Study on high-speed plasma-enhanced chemical vapor deposition of conductive carbon by microwave power

by

Hansin Bae

Department of Electronics

Nagoya University

Nagoya, Japan

Table of Contents

Chapter 1
Introduction

1.1 Background

1.1.1 Various types of carbon film

Carbon films are attractive materials because of their physical and chemical characteristics, *i.e.*, high thermal conductivity, anti-corrosion, wear resistance, low friction, eco-friendly. The carbon exists in various forms depending on the bonding structure. It is well-known that graphite and diamond are composed only of carbon atom, but their structures are not the same. In addition to the graphite and the diamond, the carbon has more allotropes such as graphene, fullerenes, carbon nanotube, amorphous carbon (a-C) and so on.[1] The interesting point is that they have different characteristics due to their different structures. For example, the diamond and the graphite, typical allotropes of carbon, are composed of 100% sp^3 and 100% sp^2, respectively, and their characteristics are completely different. In the point of the electrical conductivity, the graphite is electrically conductive, whereas the diamond is insulating.

Among the carbon's allotropes, one of carbon film widely applied to the industry is a-C. The a-C is composed of the disordered network of the carbon atoms. Additionally, on the synthesis of a-C, the hydrogen is

involved in the carbon structure by the synthesis method. So, a-C and hydrogenated amorphous carbon (a-C:H) are classified by the content of sp^2, sp^3 and hydrogen as shown in Figure 1.1.[2] a-C and a-C:H with high sp^3-bond content is called as diamond-like carbon (DLC). Since the DLC has a high sp^3 content, the DLC has the high hardness and the high wear resistance. So, the DLC is mainly applied in the fields of tools, vehicle parts, dies, medical equipment and so on.[1,3-6] a-C and a-C:H with the high sp^2-bond content is called as graphite-like carbon (GLC). Since GLC has the high sp^2 content, the GLC has the low friction and the high electrical conductivity. Using its superior characteristics, the GLC film is mainly applied in the fields of electrode, battery, lubricative parts and so on.[7-20] the GLC has been developed for the next generation battery parts in two decades. On the lithium-ion battery, to enhance the anode

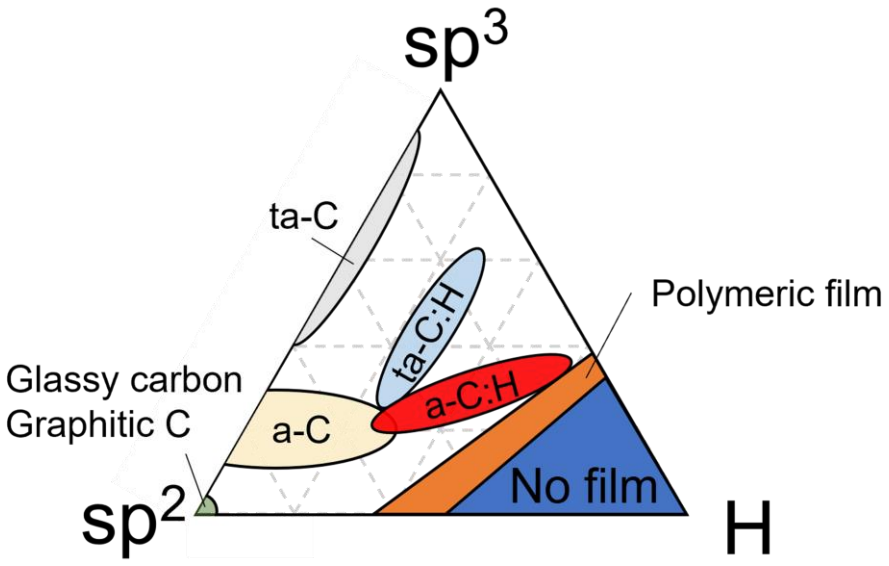

Figure 1.1 Ternary phase diagram of hydrocarbon film.[2]

capacity, the GLC coated silicon has been reported. [7,11] For the application of hydrogen fuel cell, the GLC-coated metal has been evaluated. [8-10,12-14]

1.1.2 Applications of high conductive carbon film

Recently, the high conductive carbon film, kind of GLC, has been studied as the anode of the lithium-ion battery and the bipolar plate (BPP) of proton exchange membrane fuel cell (PEMFC).

As the application for the anode of the lithium-ion battery, graphite is mainly used as a material for the anode, but its capacity is not enough to satisfy the market requirement. Among the numerous anode materials, silicon is attracting attention because it has 10 times higher charge capacity (4200 mAh/g) than that of the graphite. However, the silicon has difficulty in applying for the lithium-ion battery, because the volume of silicon expands when the silicon is lithiated and the cracks are induced in the silicon after repetitive charging and discharging as shown in Figure 1.2. Due to the induced crack, the electrical contact between the particles is degraded, and the charge capacity is drastically reduced. The above issue can be solved by introducing conductive carbon film. The cracks by the volume expansion can be suppressed by high conductive carbon coating on the silicon surface. Furthermore, the high conductive carbon

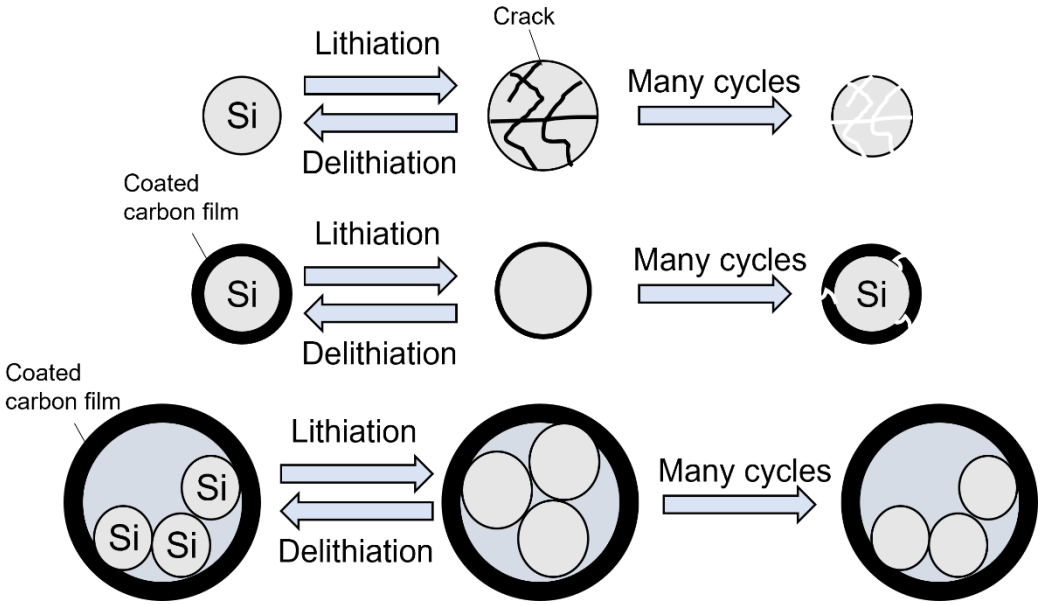

Figure 1.2 Ternary phase diagram of hydrocarbon film.

coating improves the electrical conductivity between the Si particles and the electrochemical properties of the electrolyte and the durable repetition cycles.[21] The other method is encapsulation of Si particles by the thin carbon coating (5~10 nm thickness). The carbon film can increase the chemical safety and the life cycle of the silicon particles.[21,22]

As a new technology of automobiles, PEMFC is expected as a new power generation system that will replace traditional internal combustion engine. The PEMFC has attractive features, *i.e.*, eco-friend, high energy efficiency between 40% and 60%, and chemically safe characteristic. Figure 1.3 shows the structure of PEMFC and the power generation mechanism. The parts of PEMFC are separated into BPP, membranes,

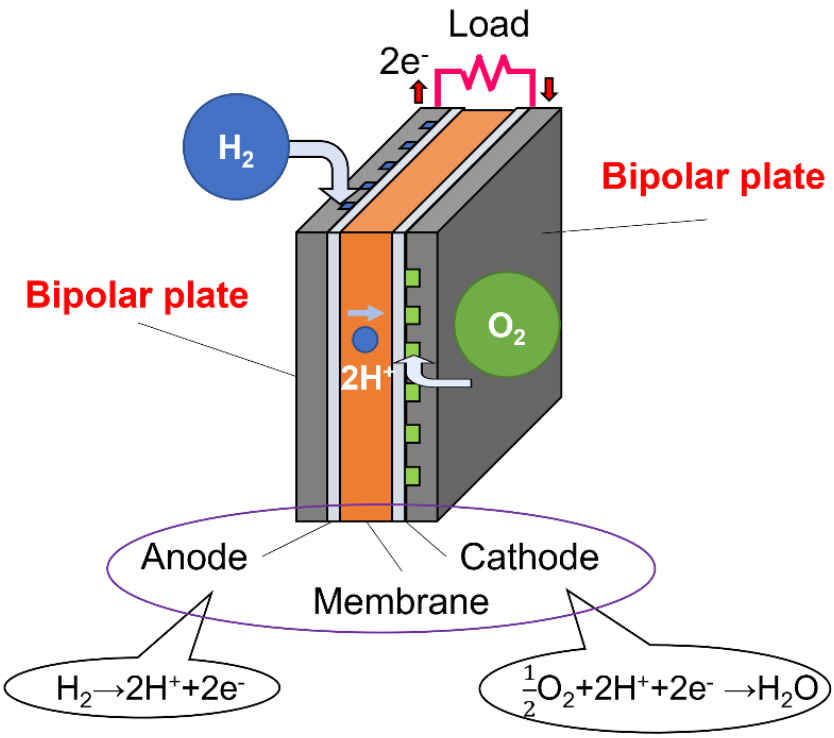

Figure 1.3 PEMFC structure and redox reaction at anode and cathode.

catalyst link & application, gas diffusion layer, membranes and electrode assemble gasket and others. The oxygen gas and the hydrogen gas are diffused from the BPP into the cathode and the anode, respectively. At the anode, the hydrogen is electrochemically oxidated, then H^+ and electron are generated as follows,

$$H_2 \rightarrow 2H^+ + 2e^- . \qquad (1.1)$$

The H^+ moves to the cathode through the membrane and electron moves to the cathode through the BPP and the electrical circuit. At the cathode, the oxygen is electrochemically reduced with H^+ and electron through equation (1.2).

$$\frac{1}{2}O_2 + 2H^+ + 2e^- \rightarrow H_2O \ . \qquad (1.2)$$

The energy is produced by the movement of electrons in the electrochemical redox reaction that occurs at the anode and the cathode, and the electric power is generated by the flow of the electron from the anode to the cathode.

So, the BPP plays various roles such as a current collector plate that conducts electrons generated in the anode toward the cathode, a skeleton that fixes and shields the membrane and the electrodes, a passage for supplying fuel gas to the electrodes and removing the water generated by reduction at the cathode. Therefore, the material of the BPP should have high electrical conductivity, low gas permeability, high mechanical strength, chemical stability, light weight and low price. US Department of Energy (DOE) proposes the specifications of the BPP as shown in table 1.1.[23] In present, most of the BPPs are made by graphite and fuel gas passages are fabricated by mechanically processing the graphite. However, the issue is the production cost in processing graphite, and C. Houchins et al.[24] has reported that the BBP production cost is higher than other part production costs. In their study, they introduced the total cost ratio of PEMFC production in the detail. The production cost ratio of the BPP is 21% of total cost, secondary higher cost of the PEMFC production. To reduce the cost of the BPP, various methods have been proposed to replace the graphite. Stainless steel, aluminum, titanium and nickel are considered as the alternative materials of the graphite because

Performance requirements for BPP of PEMFC		
Property	Value	Unit
Tensile strength	>41	MPa
Flexural strength	>59	MPa
Electrical conductivity	>100	S cm^{-1}
Corrosion rate	<1	μA cm^{-2}
Contact resistance	<20	mΩ cm^2
Hydrogen permeability	$<2.10^{-6}$	cm^3 $(cm^2s)^{-1}$
Mass	<1	kg/kW
Density	<5	g cm^{-3}
Thermal conductivity	>10	W $(m\ K)^{-1}$
Impact resistance	>40,5	J m^{-1}

Table 1.1 Performance requirements for bipolar plate of proton exchange membrane fuel cell

they are easy to be processed while satisfying a lot of conditions suggested by DOE. However, corrosion resistance is the issue to use these materials as the BPP. So, the introduction of corrosion-resistant and high-conductive coatings is required as a solution to the lack of non-corrosive metal bipolar plates. As the material which meets with these requirements, high conductive carbon is attractive, because it is chemically inert and has high electrical conductivity. The corrosion current density of high conductive carbon coated BPP is reported as 0.05 ~ 8 μA cm^{-2}.[23]

1.2 Deposition methods of high conductive carbon film

So far, some typical methods have been reported for the high conductive carbon film deposition, *i.e.*, physical vapor deposition (PVD)[25-29], chemical vapor deposition (CVD)[30-35], plasma enhanced chemical vapor deposition (PECVD)[36-45] and so on. Among various PVD methods, the sputtering method is mainly used for the carbon film deposition. To deposit the carbon film, the high-density plasma is generated near the carbon target by applying negative voltage to the target. The ions incident on the carbon target are controlled by the negative bias voltage, and the carbon atoms are sputtered. The sputtered carbon atom is deposited on the substrate. In the case of the carbon film deposition by the CVD method, the hydrocarbon gas is introduced and high temperatures from 500 ℃ to 1000 ℃ is applied to the substrate. The introduced hydrocarbon gas is dissociated on the high-temperature surface, and the carbon film is deposited on the substrate. In the PECVD method, the carbon film is deposited by introducing hydrocarbon gas into a vacuum chamber and the plasma is produced. The hydrocarbon gas is dissociated by the plasma without dissociating the hydrocarbon gas on the high temperature substrates. Therefore, the PECVD method enables us the carbon film deposition at substrate temperatures less than 400 ℃, which is much lower than that of the CVD method.

In the deposition of a-C:H, there are typically two methods for increasing sp^2 content in the structure of the carbon film. The first

method is to raise the temperature of the substrate when the carbon film is deposited. This method is mainly used in CVD and PECVD.[30-41] It has been reported that the sp^2 content increases as the substrate temperature increases. At substrate temperatures around ~400 ℃, the sp^2 content is ~20%. With increasing the substrate temperature from 400 ℃ to 750 ℃, the sp^2 content becomes up to 80%.[41] However, the application range of the CVD is limited because high substrate temperature gives a thermal damage to the substrate, *i.e.,* crack, melting down and deformation of the substrate by thermal expansion. The second method is to apply ion bombardment to the substrate during the film deposition process.[42-46] By introducing the ion bombardment effect, high conductive carbon films can be deposited at relatively low temperatures compared to those of CVD methods. J. Robertson reported that the H content and band gap of the deposited a-C:H as a function of the substrate bias voltage.[46] The deposition pressure is 3 Pa. The carbon films are deposited by different precursor gases, benzene and methane respectively. The hydrogen content in the carbon film decreases from 40% to 22% by increasing the negative bias voltage of the substrate from 50 V to 1000 V. The band gap energy also decreases from 2.3 eV to 1.0 eV by increasing the negative bias voltage of the substrate from 50 V to 1000 V. The bias voltage almost corresponds to the ion incident energy because the electrical potential across the sheath depends on the bias voltage of the substrate.

The band gap energy E_g is related with the sp^2 cluster in carbon film

as following equation.[47]

$$E_g \propto M^{-1/2} \quad \text{eV} . \tag{1.3}$$

M is the number sixfold rings per single sp^2 cluster. It is proved by experiment with Hückel approximation.[47] The above equation indicates that the change of the band gap energy is correlated with the sp^2 content and the sp^2 content increases by increasing the negative bias voltage.

J. Robertson [45,46,48] suggested the mechanism of the sp^2-bond increase by ion bombardment as the result of basic two reactions during the carbon film growth (Figure 1.4). At high bias voltages above 0.8 kV (low H content), the ion bombardment is used to dehydrogenation of the carbon film by reducing C-H bonds in the film and reforming the bonds between carbon atoms into double bonds as Figure 1.4(a). However, at the low bias voltages below 0.8 kV (intermediate hydrogen content), conversion of sp^2 into sp^3 occurs by ion subplantation as Figure 1.4(b) at the constant H content. At the low ion energies, he mentioned that 'the ion range is only a few monolayers and ions loose energy by elastic collision with target nuclei. Such collisions produce permanent vacancy interstitial pairs if the energy transferred in the collision exceeds the displacement threshold energy.'.[46] It is considered why the sp^3 state increases in the low bias voltages. As the result, he concluded that high energy ion bombardment is effective to increase sp^2 bonds in carbon film.

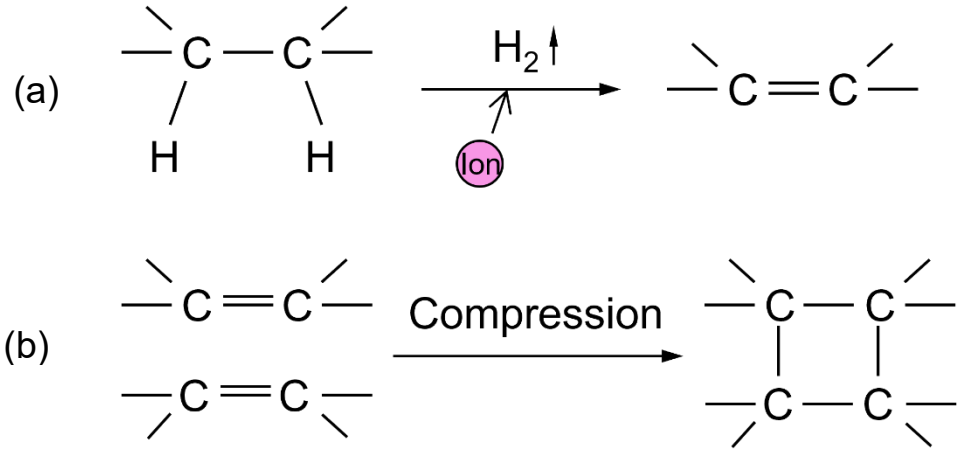

Figure 1.4 Reactions for growth of a-C:H.

1.3 Issue and purpose

As was indicated above, the carbon films with the high sp^2 content have various applications. However, a problem of the carbon film deposition with high sp^2 content is very low deposition rate. For example, the typical deposition rate reported so far is less than 0.04 nm/s in the PVD process [29] and is less than 0.001 nm/s in the CVD process [35]. The PECVD showed the relatively high deposition rate ~1.0 nm/s compared to the PVD and the CVD [39] but the deposition rate is still not enough. The issue of the low deposition rate makes commercialization of the GLC films difficult.

Purpose of this study is to explore new methods to enhance the deposition rate of high-sp^2 content carbon film without degrading the electrical conductivity and to deposit high-sp^2 content carbon film. For the application of the conductive carbon to the BPP of the PEMFC, the electrical conductivity higher than 100 Scm^{-1} is required (Table 1.1). The

deposition system for the target application, i.e., the conductive carbon deposition on the BPP, is Roll-to-Roll system or conveyor deposition system. Both deposition systems are suitable for mass production and widely used in industrial. Considering the supposed deposition system, the target deposition rate is over 10 times higher (>10 nm/s) than the surveyed deposition rates of conventional deposition methods as was indicated in the Chapter 1.2.

To achieve the above goals, this study considers following three key points.

(1) High plasma density in the deposition system

Dissociation rate of the precursor gas increases by increasing plasma density. It means that the amount of the deposition precursor increases by increasing plasma density. Additionally, from the viewpoint of the ion bombardment effect, the ion flux increases by increasing plasma density. Therefore, increasing the plasma density increases the deposition rate. Furthermore, in the point of application to the mass production system supposing Roll-to-Roll or conveyer, the plasma system should be wide. The microwave plasma system is quite suitable on the high density plasma ($>10^{17}$ m^{-3}) system with wide area (> 30 cm) than other plasma system.[49] So, in this study, the microwave surface-wave plasma and the microwave electron cyclotron resonance plasma, which are representative high density plasma systems with wide area, are introduced.

(2) Applying the highest bias voltage to the substrate

As mentioned in Chapter 1.2, the sp^2 content of the carbon film increases by increase negative bias voltage. In this study, high negative bias voltage supply is introduced.

(3) Using benzene gas as the precursor gas.

Robertson reported that benzene gas has the highest deposition rate of the carbon film among the hydrocarbon gases.[2] Among the ionization energies of hydrogen gases, the benzene has the lowest ionization energy (~9.2 eV) and high deposition rate (85 nm/min). The secondary highest deposition rate of the hydrogen gases is 40 nm/min of the acetylene. The deposition rate decreases as number of carbons constituting the molecule decreased.

1.4 Content of the dissertation

The present dissertation is composed of 5 Chapters. In Chapter 1, the background and issue of the high sp^2 carbon film and objective of the dissertation are described. In Chapter 2, the plasma equipment used for the carbon film deposition and the evaluation method used for the properties and structure of the deposited carbon film are described. In Chapter 3 and 4, the high sp^2 carbon film is deposited by two different plasma sources. In Chapter 3, the high sp^2 carbon film is deposited by microwave surface wave plasma (SWP) source with high deposition rate (~6 nm/s) with the area of 18×3 cm^2. The effects of the ion incident

energy on the carbon film properties and the carbon film structures are mainly discussed. In Chapter 4, the high-speed deposition of the high sp^2 carbon film is deposited by electron cyclotron resonance (ECR) plasma source with the high deposition rate (~5 nm/s). The effects of the ion flux on the carbon film properties and structures are discussed. Additionally, very interesting phenomenon of the bias voltage application, *i.e.*, drastic increase of the plasma density with high bias voltage application to the substrate, is described. The increase of the plasma density is evaluated by experiment and simple power balance model. In Chapter 5, the conclusion of the present dissertation is stated.

References

[1] J. Vetter: *Surf. Coat. Technol.* **257** (2014) 213.

[2] J. Robertson: *Mater. Sci. Eng. R Rep.* **37** (2002) 129.

[3] Grigoriev, S., Volosova, M., Fyodorov, S., M. Lyakhovetskiy and A. Seleznev: *J. of Materi Eng and Perform* **28** (2019).4415.

[4] M. Kalin,I. Velkavrh, J. Vižintin, L. Ožbolt: *Meccanica* **43** (2008) 623.

[5] A. Tyagi, R.S. Walia, Q. Murtaza, S. M. Pandey, P. K. Tyagi, and B. Bajaj: *Int J Refract Hard Met* **78** (2019) 107.

[6] Alanazi AS: *J Clin Med Img* **5** (2021) 1.

[7] J. Guo, X. Chen and C. Wang: *J. Mater. Chem.* **20** (2010) 5035.

[8] Y. Show: *Surf. Coat. Technol.* **202** (2007) 1252.

[9] K. Fu, L. Xue, O. Yildiz, S. Li, H. Lee, Y. Li, G. Xu, L. Zhou, P. D. Bradford and X. Zhang: *Nano Energy* **2** (2013) 976.

[10] T. Fukutsuka, T. Yamaguchi, S. Miyano, Y. Matsuo, Y. Sugie and Z. Ogumi: *J. Power Sources* **174** (2007) 199.

[11] M. Yoshio, H. Wang, K. Fukuda, T. Umeno, N. Dimov and Z. Ogumi: *J. Electrochem. Soc.* **149** (2002) A1598.

[12] C. Chung, S. Chen, P. Chiu, M. Chang, T. Hung and T. Ko: *J. Power Sources* **176** (2008) 276.

[13] Y. Fu, G. Lin, M. Hou, B. Wu, Z. Shao and B. Yi: *Int. J. Hydrog. Energy* **34** (2009) 405.

[14] K. Feng, Y. Shen, H. Sun, D. Liu, Q. An, X. Cai and P. K. Chu: *Int. J. Hydrog. Energy* **34** (2009) 6771.

[15] S. Hirono, S. Umemura, M. Tomita and R. Kaneko: *Appl. Phys. Lett.* **80**

(2002) 425.

[16] L. Li, L. Liu, X. Li, P. Guo, P. Ke and A. Wang: *ACS Appl. Mater. Interfaces* **10** (2018) 13187.

[17] L. Feng, Z. Wang, W. Shen: *Results Phys.* 12 (2019) 1495-1499.

[18] S. Zhou, G. Liu, N. Ding, L. Shang, R. Dang and J. Zhang: *Surf. Coat. Technol.* **399** (2020) 126150.

[19] Y. Wang, J. Pu, J. Wang, J. Li, J. Chen and Q. Xue: *Appl. Surf. Sci.* **311** (2014) 816.

[20] J. Qi, H. Liu, Y. Luo, D. Zhang and Y. Wang: Tribol. Int. 71 (2014) 69.

[21] A. Casimir, H. Zhang, O. Ogoke, J. C. Amine, J. Lu and G. Wu: Nano Energy 27 (2016) 359.

[22] N. Liu, H. Wu,M. T. McDowell, Y. Yao, C. Wang and Y. Cui: Nano Lett. 12 (2012) 3315.

[23] R. A. Antunes, M. Cristina, L. Oliveira, G. Ett and V. Ett: Int. J. Hydrog. **35** (2010) 3632.

[24] C. Houchins, G. J. Kleen, J. S. Spendelow, J. Kopasz, D. Peterson, N. L. Garland, D. L. Ho, J. Marcinkoski, K. E. Martin, R. Tyler and D. C. Papageorgopoulos: Membranes 2 (2012) 855.

[25] T. Schumann, M. Dubslaff, M.H. Oliveira Jr, M. Hanke, F. Fromm, T. Seyller, L. Nemec, V. Blum, M. Scheffler, J.M.J. Lopes and H. Riechert: *New J. Phys.* **15** (2013) 123034.

[26] S. K. Jerng, D. S. Yu, Y. S. Kim, J. Ryou, S. Hong, C. Kim, S. Yoon, D. K. Efetov, P. Kim and S. H. Chun: *J. Phys. Chem. C* **115** (2011) 4491.

[27] J. Kwak, S. Lee, H. Lee, G. Anoop, H. Lee, W. Kim, S. Ryu, H. Kim

and J. Jo: *Appl. Phys. Lett.* **108** (2016) 123107.

[28] X. Li, W. Dai, Q. Wang, Y. Liang and Z. Wu: *Diam. Relat. Mater.* **106** (2020) 107818.

[29] M. Huang, X. Zhang, P. Ke and A. Wang: *Appl. Surf. Sci.* **283** (2013) 321.

[30] A.N. Obraztsov, E.A. Obraztsova, A.V. Tyurnina and A.A. Zolotukhin: *Carbon* **45** (2007) 2017.

[31] M. Yudasaka, R. Kikuchi, T. Matsui, H. Kamo, Y. Ohki, S. Yoshimura and E. Ota: *Appl. Phys. Lett.* **64** (1994) 842.

[32] J. Sun , N. Lindvall, M. T. Cole, T. Wang , T. J. Booth, P. Bøggild, K. B. K. Teo, J. Liu and A. Yurgens: *J. Appl. Phys.* **111** (2012) 044103.

[33] D. Noll, P. Hönicke, Y. Kayser, S. Wagner, B. Beckhoff and U. Schwalke: *ECS J. Solid State Sci. Technol.* **7** (2018) Q3108.

[34] N. Weber, A. Binder, M. Kettner, S. Hirth, R. T. Weitz and Ž. Tomović: *Carbon* **112** (2017) 201.

[35] A.N. Obraztsov, A.V. Tyurnina, E.A. Obraztsova, A.A. Zolotukhin, B. Liu, K. Chin and A.T.S. Wee: Carbon **46** (2008) 963.

[36] R. Kato and M. Hasegawa: *Carbon* **141** (2019) 768.

[37] V.A. Krivchenko, A.A. Pilevsky, A.T. Rakhimov, B.V. Seleznev, N.V. Suetin, M. A. Timofeyev, A.V. Bespalov and O.L. Golikova: *J. Appl. Phys.* **107** (2010) 014315.

[38] V.A. Krivchenko, V.V. Dvorkin, N.N. Dzbanovsky, M.A. Timofeyev, A.S. Stepanov, A.T. Rakhimov, N.V. Suetin, O.Yu Vilkov and L.V. Yashina: *Carbon* **50** (2012) 1477.

[39] G. Kalita, M.S. Kayastha, H. Uchida, K. Wakita and M. Umeno: *RSC Adv.* **2** (2012) 3225.

[40] D. Liu, W. Yang, L. Zhang, J. Zhang, J. Meng, R. Yang, G. Zhang and D. Shi: *Carbon* **72** (2014) 387.

[41] S. Sattel, J. Robertson and H. Ehrhardt: *Journal of Applied Physics* **82** (1997) 4566.

[42] M. A. Tamor and W. C. Vassell: *J. Appl. Phys.* **76** (1994) 3823.

[43] G. Capote, G.C. Mastrapa and V.J. Trava-Airoldi: *Surf. Coat. Technol.* **284** (2015) 145.

[44] J. Che, P. Yi, L. Peng and X. Lai: *Int. J. Hydrog. Energy* **45** (2020) 16277.

[45] J. Robertson: *J. Non-Cryst. Solids* **137&138** (1991) 825.

[46] J. Robertson: *Diam. Relat. Mater.* **3** (1994) 361.

[47] J. Robertson and E. P. O'Reilly: *Phys. Rev. B* **35** (1987) 2946.

[48] A.C. Ferrari and J.Robertson: *Phys. Rev.* **61** (2000) 14095.

[49] T. Ishijima, H. Toyoda, Y. Takanishi and H. Sugai: *Jpn. J. Appl. Phys.* **50** (2011) 036002.

Chapter 2

Plasma sources, plasma diagnostics methods and carbon film evaluation methods

2.1 Introduction

In this chapter, plasma sources used for the carbon film deposition, evaluation methods of plasma properties, and carbon film evaluation method are briefly introduced. Firstly, features of two different plasma sources used in Chapter 3 and Chapter 4 are introduced. Secondly, Langmuir probe for the evaluation of the plasma parameters is introduced. Lastly, film evaluation methods, *i.e.,* four terminal sensing method, Raman spectroscopy, Fourier transform infra-red spectroscopy, X-ray photoelectron spectroscopy, scanning and transmission electron microscope and electron energy-loss spectroscopy are introduced sequentially.

2.2 Plasma sources for the carbon film deposition

2.2.1 Surface wave plasma

Surface wave is the electromagnetic wave propagating at the interface between a dielectric and a plasma. When the surface wave amplitude decays in both directions from 0 to z and -z direction as shown in Figure 2.1, the magnetic field strength H is expressed as

$$H_y^d = H_{y0} e^{\alpha_d x - jk_z z} \quad (z < 0) \quad , \tag{2.1}$$

$$H_y^p = H_{y0} e^{-\alpha_p x - jk_z z} \quad (z > 0) \quad . \tag{2.2}$$

Here, α_d and α_p are decay constants of the dielectric and plasma, respectively. k_z is wavenumber along z-direction. H_{y0} is arbitrary constant. H is continuous at the interface between the dielectric and the plasma (x = 0). From the wave equation, decay constant and k_z are

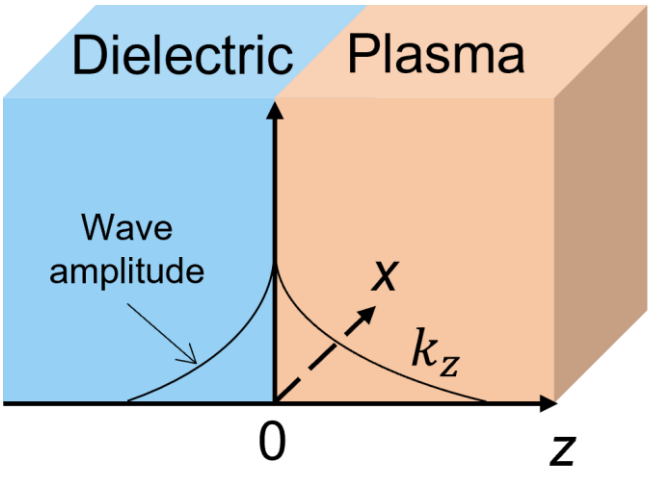

Figure 2.1 Surface-wave propagation.

expressed as

$$-\alpha_d^2 + k_z^2 = \varepsilon_d \frac{\omega^2}{c^2} \quad , \tag{2.3}$$

$$-\alpha_p^2 + k_z^2 = \varepsilon_p \frac{\omega^2}{c^2} \quad . \tag{2.4}$$

Here, ε_d and ε_p are relative permeabilities of dielectric and plasma, respectively. From the Maxwell equation (2.5), electrical components of E_z^d and E_z^p are expressed as equations (2.6) and (2.7),

$$\nabla \times H = -\varepsilon \frac{\partial E}{\partial t} \ , \tag{2.5}$$

$$E_z^d = H_{y0} \frac{\alpha_d}{j\omega\varepsilon_0\varepsilon_d} e^{\alpha_d x - jk_z z} \quad , \tag{2.6}$$

$$E_z^p = H_{y0} \frac{\alpha_p}{j\omega\varepsilon_0\varepsilon_p} e^{\alpha_d x - jk_z z} \quad . \tag{2.7}$$

ε_0 is vacuum permittivity. As E_z is continuous at $x = 0$, we can derive equation (2.8) from equations (2.6) and (2.7),

$$\frac{\alpha_p}{\varepsilon_p} = -\frac{\alpha_d}{\varepsilon_d} \quad . \tag{2.8}$$

By substituting equations (2.3) and (2.4) to (2.8),

$$\varepsilon_d^2 \left(k_z^2 - \varepsilon_d \frac{\omega^2}{c^2}\right) = \varepsilon_p^2 \left(k_z^2 - \varepsilon_p \frac{\omega^2}{c^2}\right) \quad . \tag{2.9}$$

From equation (2.9), dispersion relation of the surface wave is expressed as

$$k_z = {\varepsilon_d}^{\frac{1}{2}} \frac{\omega}{c} \left(\frac{{\omega_p}^2 - \omega^2}{{\omega_p}^2 - (1+\varepsilon_d)\omega^2}\right)^{\frac{1}{2}} \ . \tag{2.10}$$

Here, ω_p is plasma frequency and is described as $\omega_p = (e^2 n_0/\varepsilon_0 m_e)^{1/2}$, where e, n_0 and m_e are elementary charge, plasma density and electron mass, respectively. Wavenumber $k_z \rightarrow \infty$ when ${\omega_p}^2 = (1+\varepsilon_d)\omega^2$, and this means the resonance of the surface wave. For example, when the 2.45 GHz microwave is introduced to the quartz ($\varepsilon_d \approx 3.8$), the resonance of the surface wave occurs at the $n_0 \approx 3.6 \times 10^{17}$ m^{-3}. In this situation, high density plasma is generated by microwave surface wave plasma. When the plasma density is high enough, *i.e.*, ${\omega_p}^2 \geq (1+\varepsilon_d)\omega^2$, the surface wave propagates between the dielectric and plasma.

2.2.2 Electron cyclotron resonance plasma

Electron cyclotron resonance (ECR) plasma is a representative plasma generation method using microwave. When the electron moves under the existence of the magnetic field *B*, the electron feels the Lorentz force and moves in a circular orbit perpendicular to *B*. The angular frequency (ω_c) of the cyclotron motion is expressed by following equation,

$$\omega_c = \frac{eB}{m_e} . \qquad (2.11)$$

Here, m_e is the mass of the electron. When the frequency of power supply and ω_c is matched, the electron is resonantly accelerated and electromagnetic power is transferred to the electron. It is called cyclotron

damping of the wave. Sugai [1] experimentally showed cyclotron damping. When the ratio of ω_c and electromagnetic wave angular frequency ω is as close as 1, the electromagnetic wave is damped. When microwave power with typical frequency of 2.45 GHz is used, magnetic field density for the ECR is 87.5 mT. Typical feature of the ECR plasma is its high plasma density ($\geqq 1\times 10^{17} m^{-3}$) even at low pressures of 0.05~0.5 Pa.

2.2.3 Magnetic mirror effect

In addition to ECR, magnetic mirror effect sometimes plays an important role in the discharge and is explained briefly. The magnetic mirror effect occurs when a charged particle travels from low magnetic field region toward high magnetic field region, as shown in Figure 2.2.

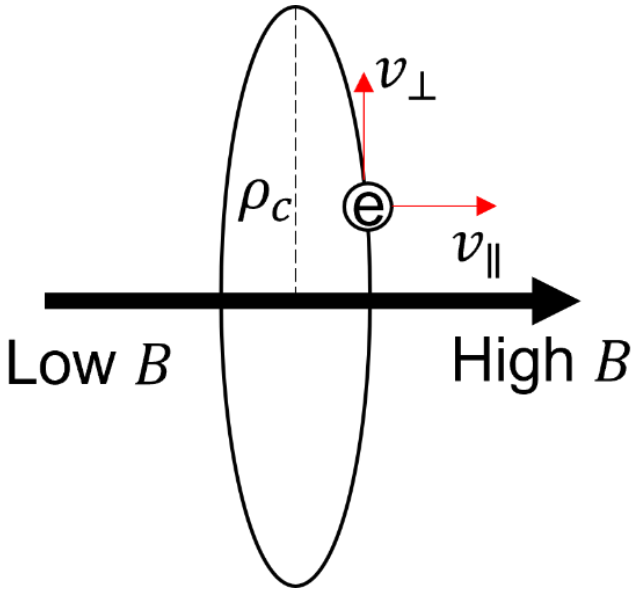

Figure 2.2 Traveling electron with cyclotron motion.

Due to gyro motion of charged particles, radius of an electron in cyclotron motion (ρ_c) is

$$\rho_c = v_\perp/\omega_c \quad . \tag{2.12}$$

Here, $v_\perp$ is the velocity perpendicular to the magnetic field. Area surrounded by electron circular trajectory (A_c) is $\pi\rho_c^2$ and the current of cyclotron electron is $I_c = e\omega_c/2\pi$. In magnetized plasma, plasma becomes slightly unti-magnetic and magnetic moment (μ) of cyclotron electron is expressed as

$$\mu = I_c A_c = m_e v_\perp^2/2B \quad . \tag{2.13}$$

From equations. (2.11) and (2.12), ρ_c decreases and B increases when the electron moves from low magnetic field to high magnetic field, conserving μ at its constant value. Due to the increase of $v_\perp$, however, velocity component parallel to the magnetic field $v_\parallel$ is decreased conserving total kinetic energy $\frac{1}{2}m_e v_e^2$, *i.e.*,

$$\frac{1}{2}m_e v_e^2 = \frac{1}{2}m_e v_\parallel^2 + \frac{1}{2}m_e v_\perp^2 . \tag{2.14}$$

Here, v_e is the electron velocity. At a strong magnetic field position where $\frac{1}{2}m_e v_e^2 = \frac{1}{2}m_e v_\perp^2$, $v_\parallel$ becomes zero and the electron is reflected toward low magnetic fields. This phenomenon is called magnetic mirror effect.

2.3 Langmuir probe method

One of the most representative indicators of the plasma state is plasma density. As mentioned in Chapter 1, the plasma density in this PECVD process is an indicator of the film deposition rate and the ion flux incident to the stage surface.

There are a lot of methods to diagnose the plasma state such as probe method, optical emission spectroscopy and so on. Among the probe methods, Langmuir probe method is representative diagnosis method of plasma parameters such as plasma density (n_0), electron temperature (T_e), plasma potential (V_p) and floating potential (V_f). Figure 2.3 shows simple diagram of Langmuir probe measurement.[2] A metal probe is inserted into a point of discharge area, and the characteristic of probe voltage (V_{PRB})-current (I_{PRB}) is evaluated by scanning V_{PRB}. Figure 2.4 shows

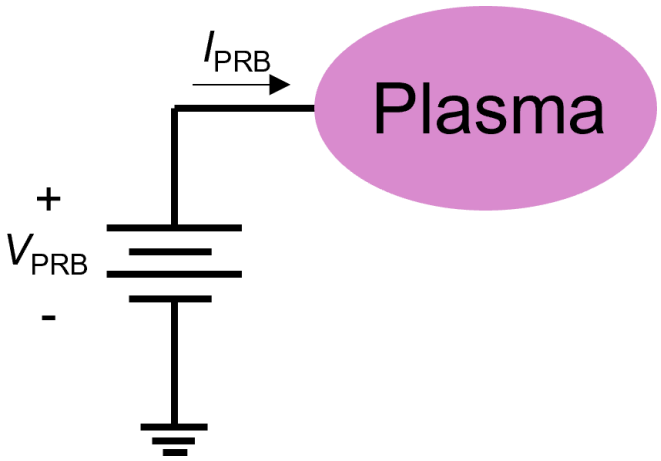

Figure 2.3 Simple diagram of Langmuir probe.

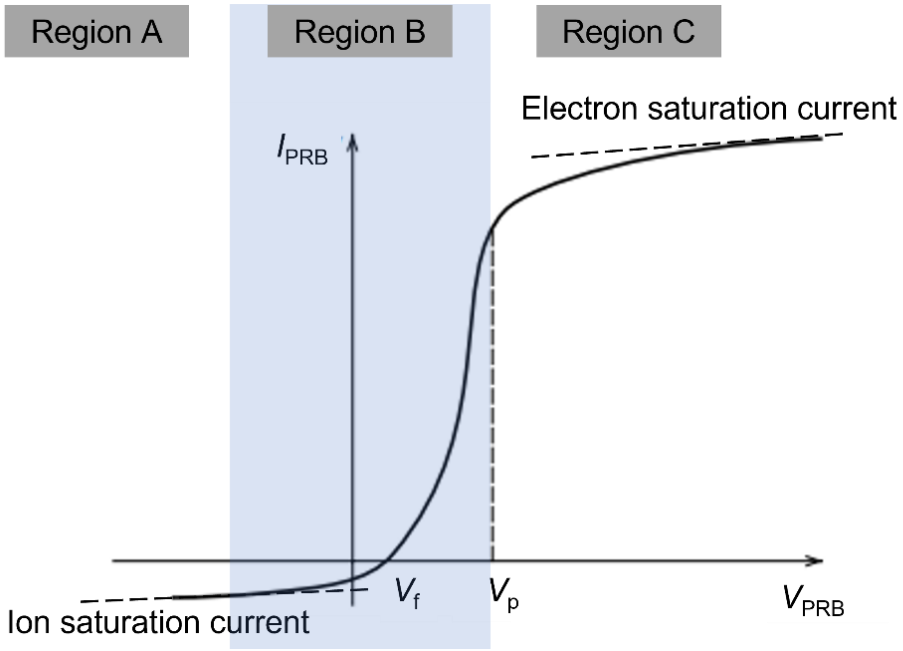

Figure 2.4 typical V_{PRB}-I_{PRB} characteristic of Langmuir probe.

typical V_{PRB}-I_{PRB} characteristic graph. The plasma parameters are evaluated from this graph. The V_{PRB} at I_{PRB} = 0 A where ion flux and electron flux are same is defined as floating potential V_f. At the region A and C in Figure 2.4, I_{PRB} is dominated by ion current for region A and by electron current for region C. So, the I_{PRB} at the region A and C are called as ion saturation current I_{is} and electron saturation current I_{es}, respectively. I_{is} and I_{es} are described by following equations

$$I_{is} = -0.605 e n_0 \left(\frac{\kappa T_e}{m_i}\right)^{\frac{1}{2}} S \quad , \tag{2.15}$$

$$I_{es} = \frac{n_0 e \langle v_e \rangle}{4} S \quad . \tag{2.16}$$

Here, κ is Boltzmann constant, m_i is mass of ion, S is the exposed

area of the metal probe in the plasma, v_e is thermal velocity of electron. At the region B ($V_{PRB} \leq V_P$), I_{PRB} is the sum of electron current I_e and ion current I_{is} ;

$$I_e = I_{PRB} - I_{is} \quad . \tag{2.17}$$

I_e in the region B is described by following equation,

$$I_e = I_{es} e^{e(V_{PRB}-V_P)/\kappa T_e}. \tag{2.18}$$

From equation (2.18), $log I_e \propto e(V_{PRB} - V_P)/\kappa T_e$. Accordingly, T_e is evaluated from slope of I_e-V_{PRB} graph in semi-logarithmic scale as $e/\kappa T_e$. Furthermore, n_0 is evaluated from equations (2.15) and (2.16).

2.4 Evaluation methods for a-C and a-C:H film

2.4.1 Four-terminal sensing method

Four-terminal sensing, or 4-point probes method, is one of typical methods for the electrical impedance evaluation of the thin film. The impedance is evaluated by 4 probes, 2 pairs of voltage and current electrodes as shown in Figure 2.5. The reason why 4 probes are used in the measurement is because contact resistance at current-flowing point can be neglected by separating current and voltage electrodes. When the current is applied to the sample by a pair of probes 1 and 4, the voltage-drop between probe 2 and 3 is measured. From the Ohm's law, the

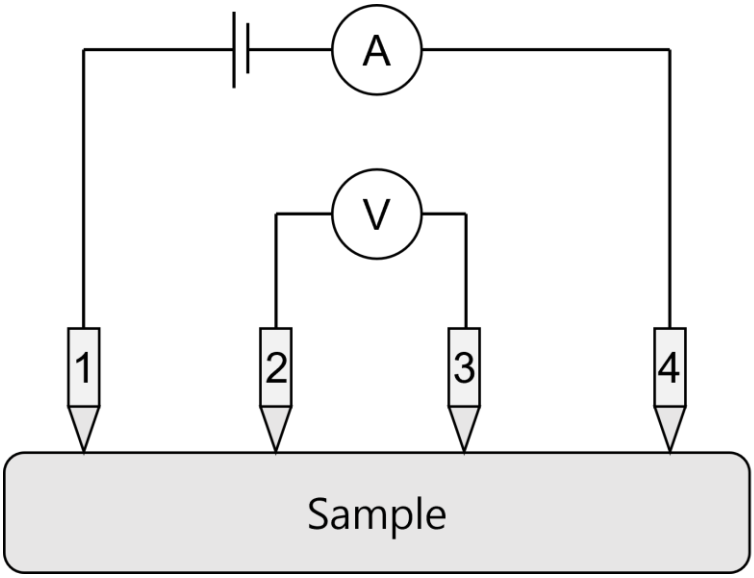

Figure 2.5 Diagram of Four-terminal sensing method.

impedance of the sample is evaluated. The unit of the impedance measured by four-terminal sensing, called sheet resistance, is Ω/sq because the thickness of the sample is not considered for evaluation of it. The sheet resistance means the impedance on infinite area of the sample. Additionally, resistivity (ρ) of the sample is evaluated by convolution of sheet resistance and thickness.

2.4.2 Raman spectroscopy

In the evaluation of carbon thin film structure, Raman spectroscopy is a typical and widely used analysis method. When a molecule is irradiated with light, the molecule goes into an excited state and then returns to the ground state. When the state returns to the ground state without changing the vibrational level, it is called Rayleigh scattering as

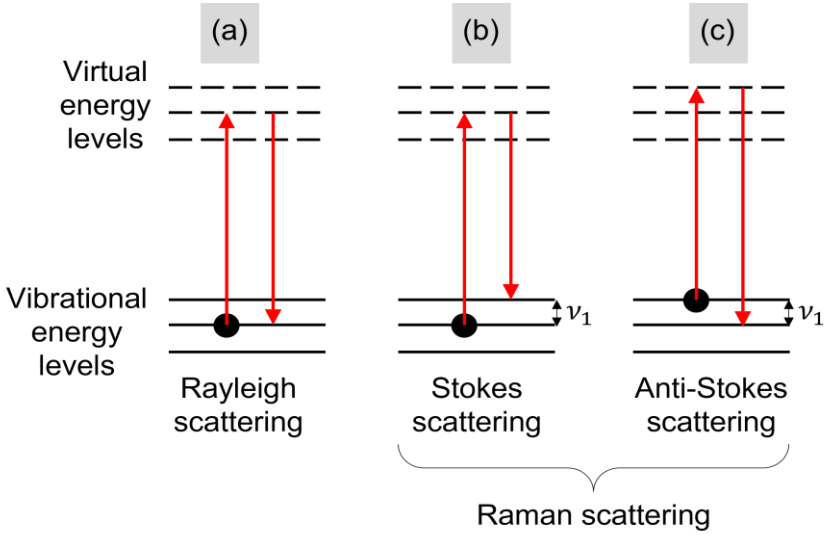

Figure 2.6 Vibrational energy shift by Raman scattering.

shown in Figure 2.6 (a). When vibrational energy level is shifted ($\Delta E = h\nu_1$) by inelastic scattering as shown in Figure 2.6 (b) and (c), it is called Raman scattering. ΔE depends on the bonding structure and the vibration mode. Therefore, it is possible to evaluate the structure of molecule by Raman spectroscopy.

In the Raman spectrum, the signal of C-H bond and sp^3 bond are very weak compared to the signal of sp^2 bond.[3] There are two types of the sp^2 bond signal, *i.e.*, breathing mode and stretching mode as shown in Figure 2.7. The signal by stretching mode is called as graphite (G) peak. The G peak is observed between 1520 and 1600 cm^{-1}. The signal from breathing mode is called as disorder (D) peak. The D peak is observed between 1330 and 1370 cm^{-1}. The feature of D peak is not observed in ordered aromatic ring. D peak occurs by the disorder of aromatic ring or the unchained aromatic ring. Therefore, D peak is strong at the polycrystalline structure. Due to the difference in the occurrence of the

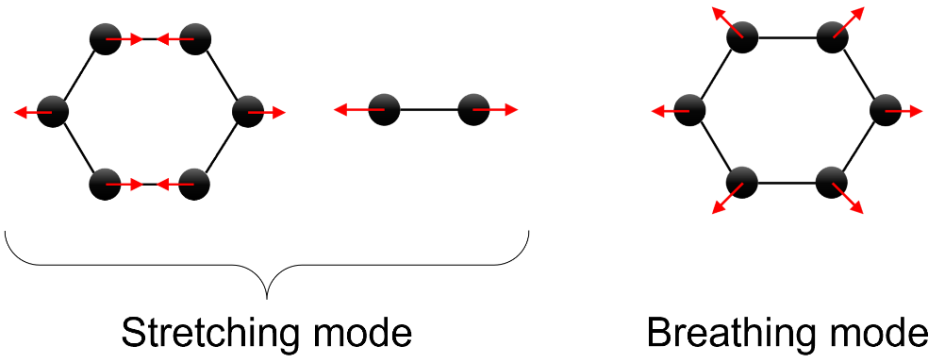

Figure 2.7 Vibration mode of sp^2 bond.

G and D peaks, the Raman spectrum of the carbon film appears differently depending on the bonding structure. D.R. Tallant [4] reported the Raman spectra of the diamond, DLC, glassy carbon (high sp^2 a-C) and graphite. The Raman spectrum of the diamond shows a sharp peak at the Raman shift 1315 cm^{-1}. The Raman spectrum of the DLC shows a broad peak at the Raman shift 1331 cm^{-1}. The Raman spectrum of the glassy carbon shows the two broad peaks at the Raman shift 1360 cm^{-1} and 1590 cm^{-1}. The Raman spectrum of the graphite shows a sharp high peak at a Raman shift wavenumber of 1580 cm^{-1} and a small peak at a wavenumber of 1350 cm^{-1}. Ferrari [3] shows that the G peak position and the intensity ratio of the G and D peaks (I(G) and I(D)) are different depending on the carbon bond structures of the hydrogen-free carbon film. The I(D)/I(G) ratio increases from 0.2 to 2.0 and G peak position increases from 1520 cm^{-1} to 1600 cm^{-1} by the graphitization of high sp^3 carbon (sp^3 content decreases from 85% to 0%). Ferrari [3] also explained the I(D)/I(G) ratio and G peak position in a-C:H. The H

content affects to the structure of carbon film. When the H content increases in a-C:H, the sp^3 content increases by H saturating C=C bonds as $\equiv CH_x$ groups rather than increasing sp^3 content by C-C bond. So, in the low H content of a-C:H, sp^2 bond dominates. In the intermediate H content of a-C:H, sp^3 content by the C-C bonds becomes its maximum and the film becomes similar to DLC. In the high H content of a-C:H, the carbon film is polymeric. The optical gap is related with the sp^2 and sp^3 fractions. So, the optical gap (Tauc gap) is different by the different H content, *i.e.*, low sp^2 content ($\leq$1 eV), intermediate H content (1 eV ~ 1.8 eV) and high H content ($\geq$1.8 eV). Raman results of a-C:H, *i.e.*, *I*(D)/*I*(G) ratio and G peak position are plotted as a function of Tauc gap energy.[3] The *I*(D)/*I*(G) ratio decreases from 3.5 to 0.1 and G peak position decreases from 1585 cm^{-1} to 1520 cm^{-1} with increasing the Tauc gap energy. To summarize the trend of Raman spectrum in the a-C and a-C:H, both the *I*(D)/*I*(G) peak ratio and G peak position increase by increasing sp^2 content.

2.4.3 Fourier transform infrared spectroscopy

Fourier transform infra-red (FTIR) spectroscopy is an evaluation method that transmits infra-red light to a matter and confirms the bonding state of the material through the absorption rate of the infra-red light. When the light of intensity I_0 pass through a sample of thickness *L*, the light intensity decreases as it passes through the sample from I_0 to I_a. Beer-Lambert law defines the relation between the transmittance and

absorbance k and is expressed as (2.19)

$$ln\frac{I_a}{I_0} = -kL \ . \tag{2.19}$$

The I_a of frequency v is expressed as

$$I_a(v) = I_0(v)\exp(-k(v)L) \ , \tag{2.20}$$

$$k(v) = k\alpha(v) \ . \tag{2.21}$$

$k(v)$ is expressed as absorbed line profile, $\alpha(v)$ is profile of the absorption coefficient as a function of frequency v. From the FTIR spectroscopy, the profile of $\alpha(v)$ is evaluated.

The FTIR spectroscopy is useful to evaluate C-H bonds in the hydrogenated carbon film. M. Veres [5] introduces that the stretching mode of C-H bond is ranged in the wavenumber 2750 ~ 3250 cm^{-1} as shown in Table 2.1. Figure 2.8 show the FTIR spectra of a-C:H deposited by different bias voltages of 250, 500, 750, and 1000 V. The peaks and areas of FTIR absorption intensity is decreased by increasing the bias voltage. It means that C-H bonds decrease in a-C:H by increasing ion bombardment. Furthermore, the H content (n_{H}) in a-C:H is evaluated by FTIR spectrum. n_{H} in the film is obtained from following equation (2.22),

$$n_{\mathrm{H}} = A_{\mathrm{s}} \int \frac{\alpha(\nu)}{\nu} d\nu \ . \tag{2.22}$$

Here, ν, α and A_s are wavenumber, absorption coefficient and coefficient of C-H absorption, respectively. A_s value is reported as 8.7×10^{20} cm^{-2}.[7]

The IR spectrum of the C-H bond should be seperated by each peaks to evaluate n_{H}.

Peak location (cm^{-1})	FWHM (cm^{-1})	Relative intensity	Assign
2852	24.7	1.05	sp^3 CH_2 symmetric
2873	29.3	2.04	sp^3 CH_3 symmetric
2904	31.9	2.89	sp^3 CH
2928	25.6	2.26	sp^3 CH_2 asymmetric
2950	25.5	1.68	sp^3 CH_3 asymmetric
2973	31.0	2.13	sp^2 CH_2 symmetric
3026	20.6	2.69	sp^2 CH olefinic
3058	24.6	2.60	sp^2 CH aromatic
3083	13.5	0.63	sp^2 CH_2 asymmetric

Table 2.1 FTIR Peak locations by the absorption of C-H bond [5].

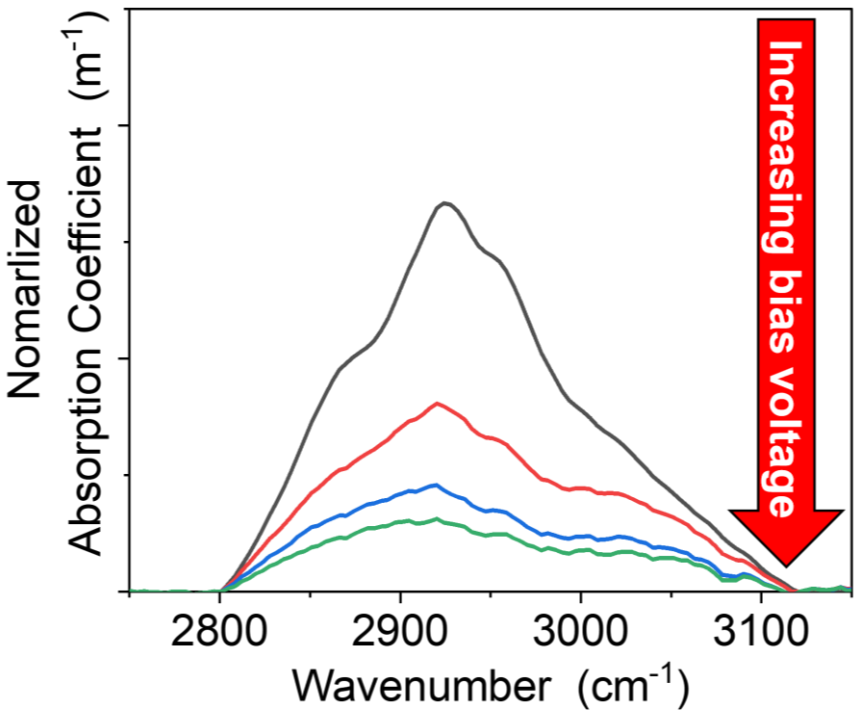

Figure 2.8 FTIR spectra of C-H bond by different bias voltage.

2.4.4 *X-ray photoelectron spectroscopy*

X-ray photoelectron spectroscopy (XPS) is a method to evaluate the bonding state of matter as well as quantitative analysis of elements on the surface of a material in a few nm. X-ray has enough energy to eject electron in the matter. So, by irradiating X-rays on a matter, the binding energy of molecules of a matter is evaluated as the difference in kinetic energy between the incident X-rays and the ejected electron.

Figure 2.9 shows simple concept to evaluate the ejected electron energy. When the X-ray with the high energy $h\nu$ is radiated from the X-ray source to the matter, the electron in the matter is ejected by X-ray. The ejected electron is called photoelectron. The kinetic energy of the photoelectron E_{kin} is detected by the energy analyzer. So, the binding energy of the electron E_b is calculated as $E_b = h\nu - E_{kin} - W_f$, where W_f is work function and is negligibly small. As elements have unique E_bs

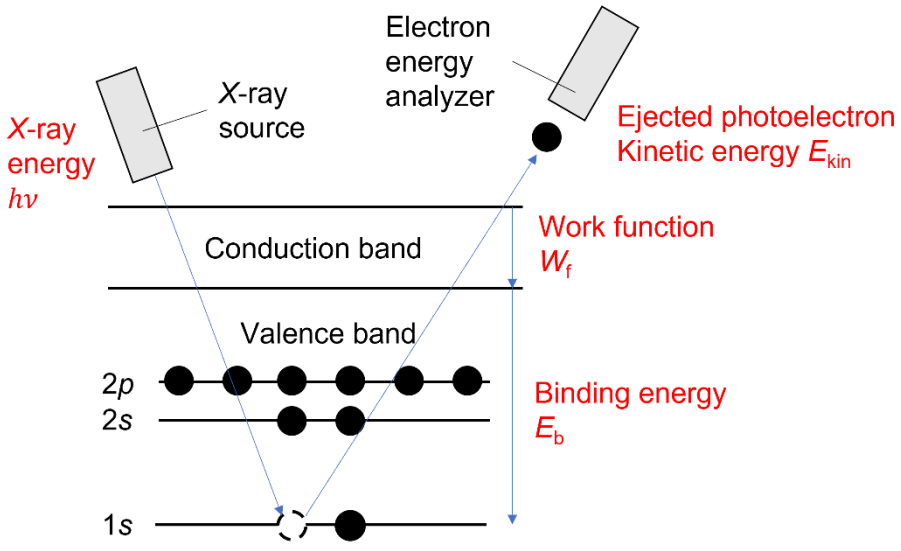

Figure 2.9 Principle of XPS.

depending on their chemical binding states, the XPS is very useful to evaluate the elements and binding states in the matter.

In the carbon film structure evaluation, XPS is useful to evaluate the sp^2 and sp^3 ratio. The XPS spectrum of C1s is located at binding energies of 284 ~ 286 eV, and the spectrum of C1s can be separated into sp^2 (284.5±0.1 eV), sp^3 (285.3±0.1 eV) and C-O (286.5±0.1 eV) peaks.[8] The C-O peak usually indicates the oxidized surface of the sample since the sample is exposed to the atmosphere. The ratio of sp^2 and sp^3 is evaluated through the area ratio of each separated spectrum.

The peak of the C1s spectrum shifts to lower binding energies by increasing the sp^2 content. Increase of the sp^2 content by the ion bombardment is also reported from the XPS measurement.[9] The carbon film is deposited by different bias voltages from -500 V to 0 V. The peak energy of the C1s spectrum decreases from the binding energy of 285 eV to 283 eV by increasing the negative bias voltage from 0 V to -500 V.

2.4.5 Scanning and transmission electron microscope and electron energy-loss spectroscopy

Scanning and transmission electron microscope (STEM) is an electron microscope that combines the high resolution of the transmission electron microscope (TEM) with the stereoscopic image of the scanning electron microscope (SEM). In the STEM measurement, the electron beam is focused to a fine spot, typical spot size 0.05 ~ 0.2 nm, to acquire high-resolution images. Therefore, the nano-size structure of matter can be illuminated by STEM. Electron energy loss spectroscopy (EELS) measures the energy loss of inelastically scattered electrons those occur when accelerated electrons are irradiated into a thin matter (sample thickness <100 nm). By detecting energy loss of electrons, the element, composition and chemical bonding state of a matter are evaluated.

STEM pictures and EELS spectra by different carbon structure in N. Jiana's study.[10] In the STEM picture of the graphitized carbon, the patterns with intervals of 0.34 nm, which is the length between the graphite layers, is confirmed. However, in the a-C, there is no pattern to confirm crystalline structure. To evaluate the carbon film structure, sp^2 and sp^3 are evaluated by EELS. The peak of the sp^2 bond is located at the 285.5 eV. The peak of the sp^3 bond is located at the 290 eV. The EELS spectra of carbon annealed at each temperature, from 25 ℃ to 1000 ℃, are introduced.[10] As the carbon film is graphitized, the peak of C1s-π

corresponding to the sp^2 bond gradually increases. Additionally, L. Ponsonnet et al.[11] introduced EELS spectra of the graphitized carbon and a-C like DLC. From this report, the carbon structure is estimated by EELS spectrum. For the diamond, the peak of 285 eV doesn't appear.

References

[1] H. Sugai: *Phys. Rev.* **A24** (1981) 157.

[2] M.A. Lieberman "Principles of plasma discharge and materials processing" 2nd ed., Wiley, New Jersey, Ch. 6.6.

[3] A.C. Ferrari and J. Robertson: *Phys. Rev.* **61** (2000) 14095.

[4] D.R. Tallant, J.E. Parmeter, M.P. Siegal and R.L. Simpson: *Diam, Relat. Mater.* **4** (1995) 191.

[5] M. Veres, M. Koós and I. Pócsik: *Diam. Relat. Mater.* **11** (2002) 1110.

[6] M. Zarrabian, N. Fourches-Coulon, G. Turban, M. Lancin and C. Marhic: *Diam. Relat. Mater.* **6** (1997) 542.

[7] H. Kojima, H. Kako, M. Terada, H. Sugai and T. Okuda: *Jpn. J. Appl. Phys.* **24** (1985) 1432.

[8] S.T. Jackson and R.G. Nuzzo: *Appl. Surf. Sci.* **90** (1995) 195.

[9] Y. Wang, L. Wang, G. Zhang, S.C. Wang, R.J.K. Wood and Q. Xue: *Surf. Coat. Technol.* **205** (2010) 793.

[10] N. Jiana, P. Xuea and D. Diaoa: *Appl. Surf. Sci.* **498** (2019) 143831.

[11] L. Ponsonnet, C. Donnet, K. Varlot, J. M Martin, A. Grill and V. Patel: *Thin Solid Films* **319** (1998) 97.

Chapter 3

Carbon deposition with surface wave plasma

3.1 Introduction

As was mentioned in Chapter 1, to increase electrical conductivity of carbon films, the high ion energy with high ion-flux density is important. Furthermore, from the viewpoint of the productivity, high deposition rate with large processing area is also important. As for the high ion-flux and the high deposition rate, high density plasma is required because the production rate of reactive species and ion flux to the substrate are determined by the plasma density. As for the uniformity of the deposition rate and the film quality, the plasma density must be spatially uniform because the plasma density distribution determines the spatial profile of the deposition precursor and the ion flux. Accordingly, to realize high-speed deposition of the conductive carbon film with large area, high density plasma source with good spatial uniformity is required, in addition to the high-voltage biasing of the substrate.

In this chapter, the high conductive carbon deposition with wide-area and high deposition speed is demonstrated by combination of surface wave plasma (SWP) and high impulse power generator. The SWP produces high density plasma ($\geq 10^{17}$ m^{-3}) with good spatial

uniformity.[1-5] The high impulse power source realizes film biasing with high negative voltages up to 2 kV. By combination of the SWP and high-impulse power source, both the high incident energy and high flux of ion is realized with good spatial uniformity of the deposition rate and the film quality. Influence of the bias voltage on various film properties such as electrical conductivity of the film or film structure are introduced.

3.2 Experimental apparatus

Schematic of experimental apparatus is shown in Figure 3.1. A vacuum vessel (length: 50 cm, width: 26 cm, height:16 cm) is equipped with a quartz plate (length: 50 cm, width: 17 cm, thickness: 1 cm). A vacuum chamber is evacuated by a dry pump down to base pressures less than 0.1 Pa. The quartz plate is attached with a waveguide and a slot plate involving two arrays of three slot antennas. The waveguide is terminated with a plunger to control node position of the standing wave in the waveguide. In this study, Cartesian coordinates (x, y, z) with its origin on the center of the quartz plate are defined as shown Figure 3.1. Argon gas is introduced into the vessel through a mass flow controller at a flow rate of 65 sccm. Apart from the Argon (Ar) gas feed, vaporized benzene (C_6H_6) is fed through a gas manifold at z = 3 cm toward a water-cooled substrate stage (26×7 cm^2). The center of the stage is located at x = -7.5 cm off center of the vessel and another coordinate (x_2) on the stage surface is introduced with its origin on the stage center. The total pressure is kept at 13 Pa by a conductance valve.

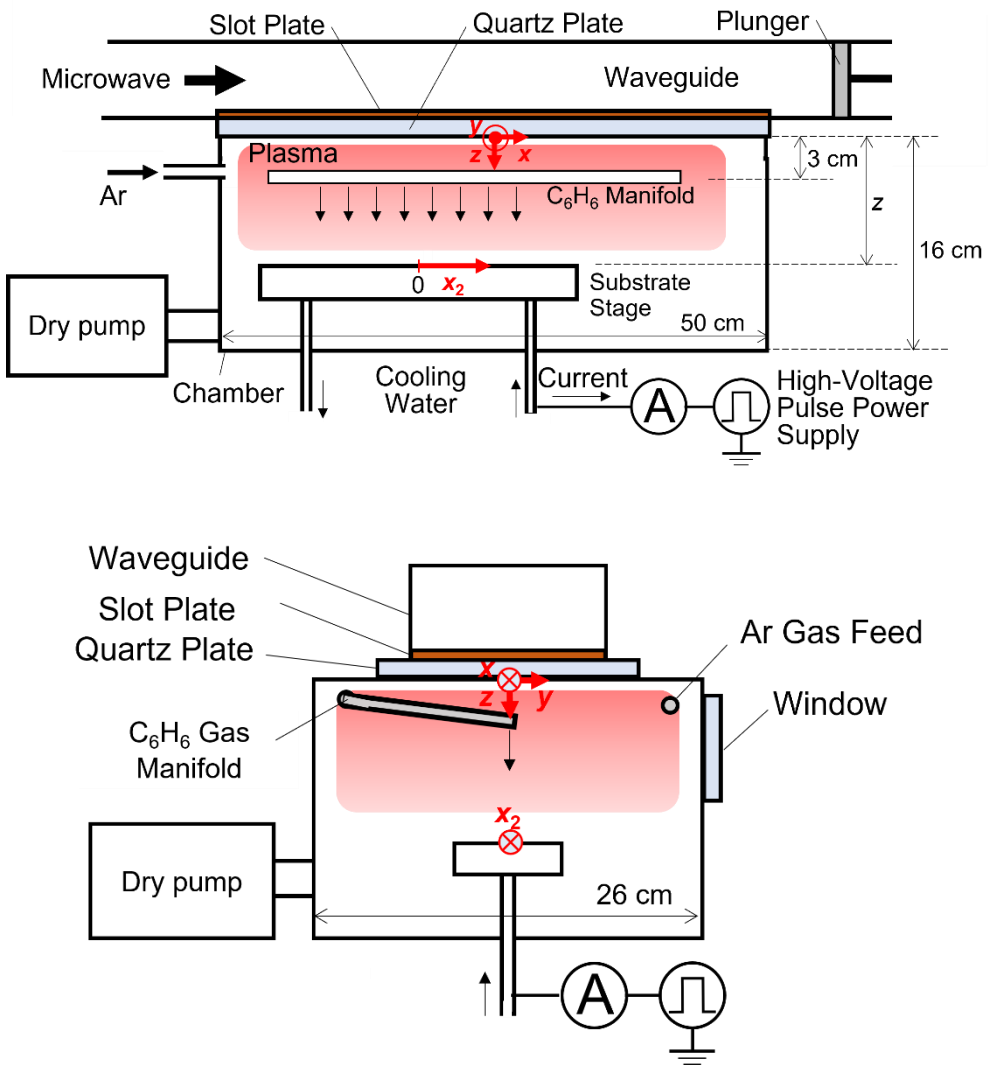

Figure 3.1 Schematic of experimental apparatus.

Microwave power (2.45 GHz, 1.3 kW) is applied to the waveguide and the SWP is produced in front of the quartz plate. The deposited film tends to produce sp^3 bonds and to be insulative if the ion bombardment is not enough. This results in charging-up of the film surface by positive charge and unipolar arcing on the film surface. Such situation can be avoided by

using pulsed DC biasing, where accumulated charge is released during the pulse-off phase. In this study, the stage is negatively biased by a high impulse voltage generator (maximum voltage: -2 kV, pulse frequency: 500 Hz, pulse-on time: 0.2 ms). Hereafter, stage bias voltage (V_B) is indicated by its absolute value. The voltage and current are measured by a high voltage probe and a current probe, respectively. At the same stage position and the microwave power, the stage current is almost the same irrespective to the bias voltage.

Electrically conductive (n-doped) silicon (100) substrate (size: 18×3 cm^2, resistivity: 10.5 Ω·m, sheet resistance: 150 Ω/sq) is placed on the stage surface. Prior to the film deposition, the silicon substrates are cleaned by an ultrasonic cleaner with acetone and are pre-sputtered by Argon plasma for 2 min at V_B = 1 kV. After the pre-sputtering of substrates, benzene gas at a flow rate of 50 sccm is introduced through the gas manifold, and the film is deposited on the substrate. Film thickness is measured by the step profiler and electrical resistivity is measured by the four-terminal sensing method. The deposited film thickness is ~ 400 nm in all experiments. A distance from the quartz plate to the stage and bias voltage are varied.

Film quality is investigated by Raman spectroscopy, FTIR, X-ray diffraction (XRD), X-ray photoelectron spectroscopy (XPS), scanning transmission electron microscopy (STEM) and electron energy loss spectroscopy (EELS).

3.3 Measurement of plasma density and stage current

3.3.1 Bias voltage and current of the stage

As mentioned above, ion bombardment during the film deposition plays important role to obtain the high conductive carbon film. To evaluate the ion flux to the substrate, bias voltage and current on the stage are measured. Figure 3.2 shows voltage and current waveforms at V_B = 2.0 kV. Ar gas pressure without benzene gas, and microwave power are 13 Pa and 1.3 kW, respectively. Just after turning on the pulse at t = 0, ringing is observed (<5μs) with a maximum bias voltage and a current of 3.5 kV and 2 A, respectively. After then, steady state voltage and current at 2.0 kV and 0.75 A, respectively, are observed. By turning off the pulse power at t = 0.2 ms, a long falling time is observed. In the present study, the high-voltage pulse power generator does not have a short-circuiting transistor to release the output capacitor charge during the pulse-off phase. Long falling time is because the charge reduction of the capacitor is conducted only by the current from the plasma.

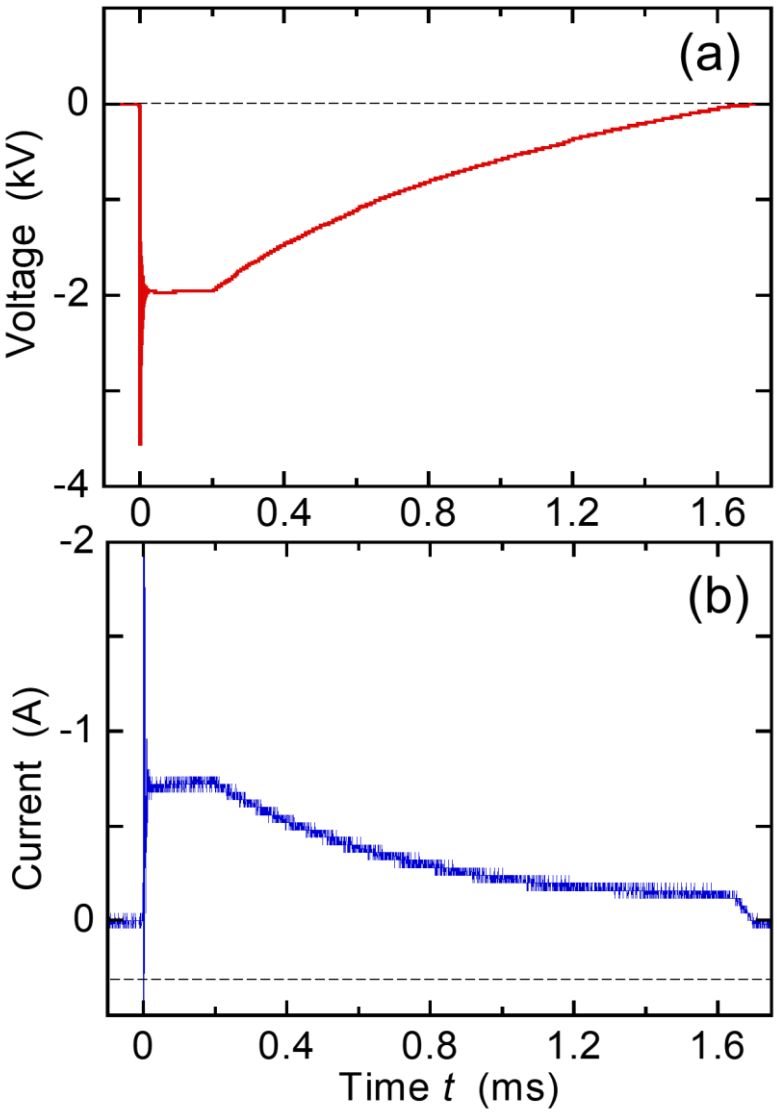

Figure 3.2 Typical (a) voltage and (b) current waveforms of the stage.

3.3.2 Spatial distribution of plasma density

Spatial profile of Ar plasma density is measured using wire Langmuir probes made of tungsten (diameter: 0.1 mm, length: 10 mm). Two identical Langmuir probes are moved along the z axis at x = 0 cm and along the x-axis at z = 8 cm. Spatial distributions of the plasma density and the electron temperature are measured by Langmuir probes. Ar gas pressure and microwave power are 13 Pa and 1.3 kW, respectively. In this measurement, C_6H_6 is not introduced to avoid film deposition on the probe surface. Figures 3.3(a) and (b) show spatial profiles of the plasma densities along z axis at x = 0 and along x axis at z = 8 cm, respectively. In Figure 3.3(a), the plasma density monotonically decreases with increasing the distance from the quartz plate. Such spatial variation of the plasma density is almost similar with those of other SWPs.[1,5] In Figure 3.3(b), uniform plasma density ($\sim 4.1\times10^{17}$ m^{-3}) along x direction is observed at $x<\pm15$ cm. Uniformity of electron temperature at $T_e\sim1.4$ eV is also confirmed, although not shown in the figure.

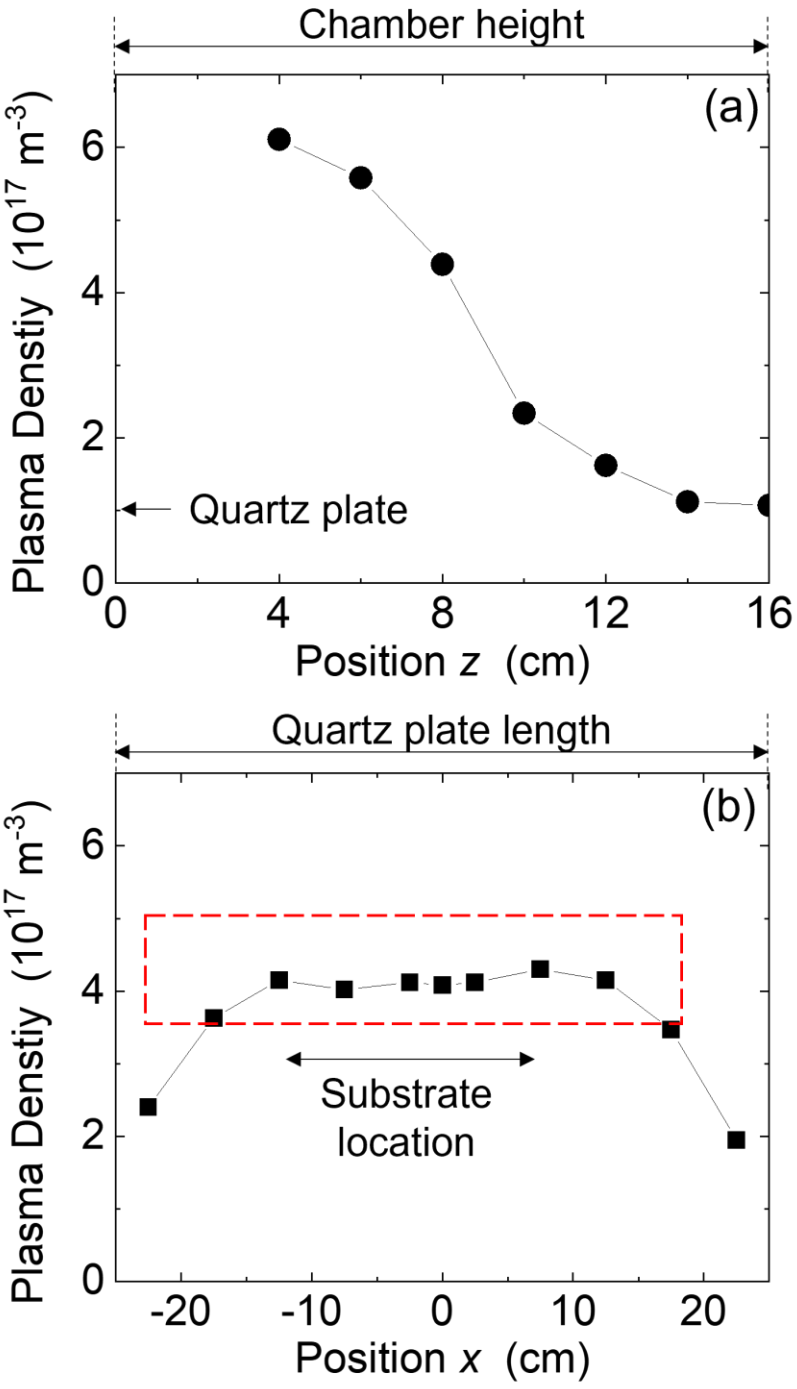

Figure 3.3 Spatial profiles of (a) plasma density along z-axis at x=0 and (b) along x-axis at z=8 cm (stage surface position).

3.4 Deposition rate and electrical conductivity

3.4.1 Spatial uniformity

Carbon film is deposited at a stage position of $z = 8$ cm by introducing the benzene gas, and spatial uniformity of the film properties, *i.e.*, deposition rate and sheet resistance, are evaluated. Figures 3.4(a) and (b) show spatial profiles of deposition rate and sheet resistance, respectively, at various bias voltages. Both the deposition rate and the sheet resistance are almost uniform along x_2 direction irrespective of the bias voltage. Deposition rate decreases from 13 to 5 nm/s with increasing the bias voltage from 0.5 to 1.75 kV. Carbon film is almost insulative at low bias voltages. However, electrical conductivity of the film drastically decreases at bias voltages above 1.35 kV.

3.4.2 Bias voltage dependence

From the viewpoint of film structure, it is known that the film conductivity is increased by the increase of the sp^2 state, and that the ion flux and the ion energy play important roles to control the film conductivity.[7-10] Firstly, the effect of the ion energy to the carbon film is investigated by changing the bias voltage (V_B). As was mentioned, the stage current is almost independent of the V_B and ion flux is constant with respect to the V_B.

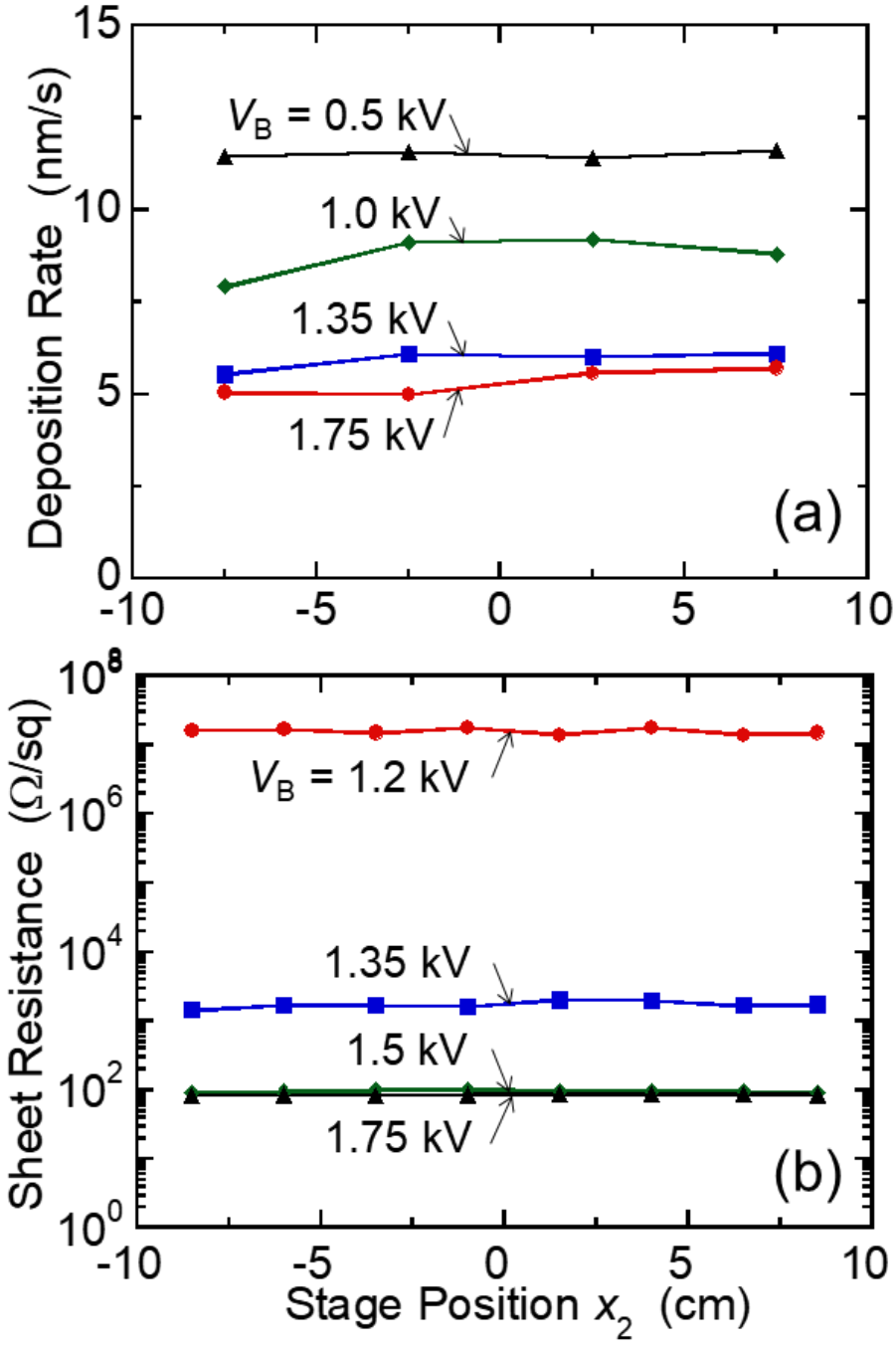

Figure 3.4 Spatial uniformities of (a) deposition rate and (b) sheet resistance on the stage.

Figures 3.5(a) and (b) show spatially-averaged deposition rate and sheet resistance, respectively, as a function of the V_B. Both the deposition rate and the sheet resistance decrease with increasing in the V_B. At high bias voltages ($V_B \geq 1.5$ kV), sheet resistance is lower than that of the silicon substrate. At V_B = 2.0 kV, the deposition rate and the sheet resistance are 6 nm/s and 80 Ω/sq, respectively. The conductivity is possible to be evaluated by the convolution of sheet resistance and film thickness. The problem is the sheet resistance is affected by the carbon film and silicon substrate. To estimate conductivity of the carbon film, the sheet resistance lower than silicon substrate is considered ($V_B \geq 1.5$ kV). In this case, the estimated conductivity of the carbon film is 200 S/cm, which is low enough to satisfy DOE requirements of the BPP, as shown in Chapter 1. These results are better than those of previous studies[11-26] and suggest that energetic ions accelerated by the negative bias voltage contribute to the deposition of conductive carbon film.

In the previous study of carbon film deposition by ion beam, sp^3 bond becomes dominant when the carbon ion energy is ~100 eV, and sp^2 bond increases when the ion energy is higher than 100 eV.[27] This result suggests that high conductive film can be deposited at higher ion energies. In the case of the PECVD of high conductive film, however, hydrogen atoms incorporated in the film also hinders the sp^2-bond formation and the ion bombardment is required also for the hydrogen removal from the film. This means that the enhancement of the ion bombardment not only by the ion flux, but also by the ion energy is required for the high

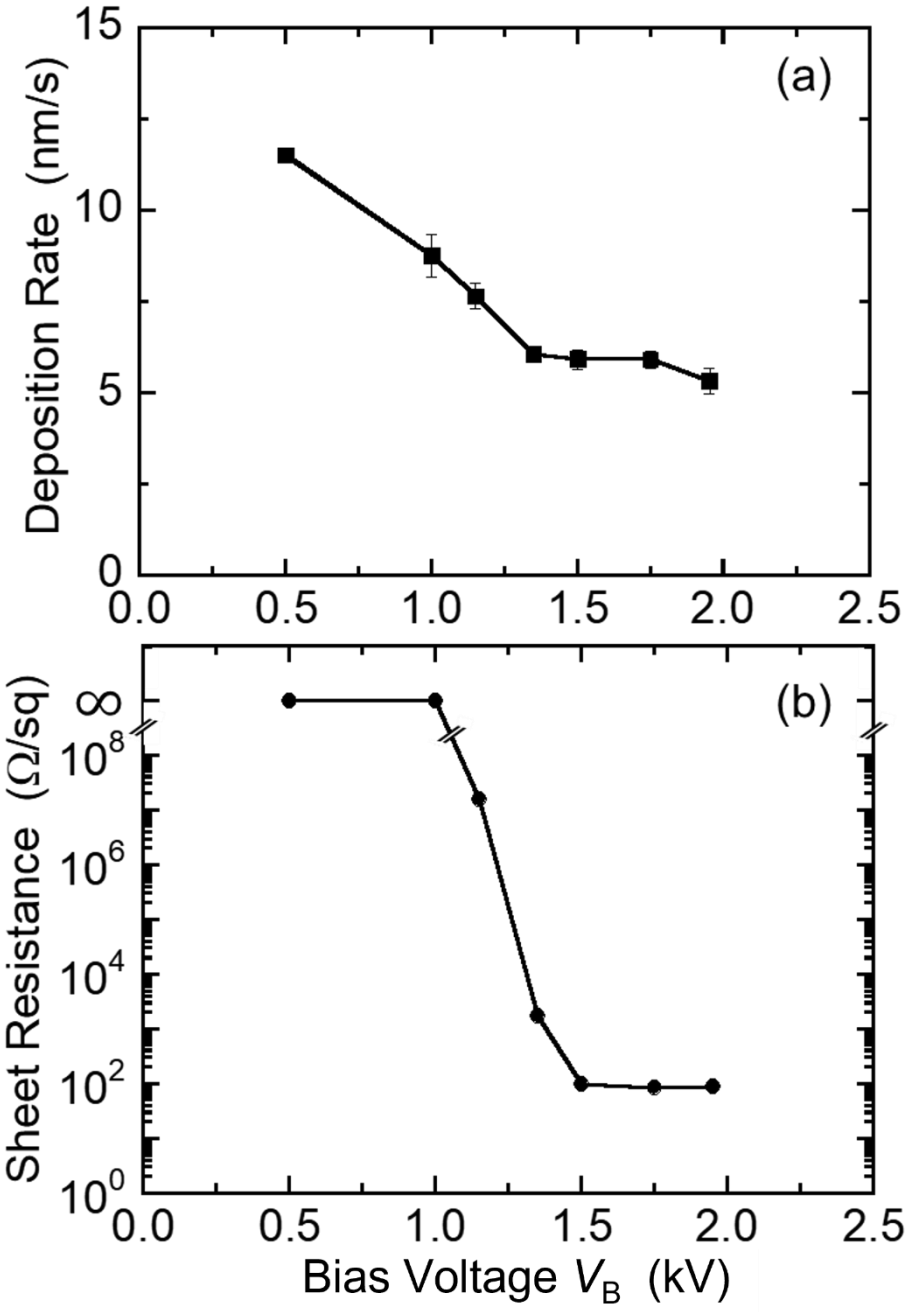

Figure 3.5 Bias voltage dependences of (a) deposition rate and (b) sheet resistance.

conductive film deposition by the PECVD. The SWP, a high-density microwave plasma, enables us to increase the ion flux to the substrate. From the plasma density n_o and Bohm velocity $u_B = (kT_e/M)^{1/2}$, ion flux Γ_i is evaluated to be

$$\Gamma_i = n_o u_B . \tag{3.1}$$

where, k, T_e and M are Boltzmann constant, electron temperature and ion mass, respectively. The ion flux estimated from the plasma density is $1.2\text{x}10^{21}$ $1/\text{m}^2\text{s}$. Supposing an ion incident energy of 1.5 keV, energy deposition flux to the film is $\sim 2\text{x}10^{23}$ $\text{eV}/\text{m}^2\text{s}$, taking into account the pulse duty ratio. Considering carbon atom deposition flux of $7\text{x}10^{20}$ $1/\text{m}^2\text{s}$ from the deposition rate (~6 nm/s), ion energy deposition per one depositing carbon atom is estimated to be ~300 eV, and this energy is much higher than the ion energy to produce sp^3 and the result is consistent with the previous work showing that higher ion energy produces sp^2 bonds rather than sp^3 bonds. In conventional RF plasma sources, plasma density is one or two orders of magnitude lower than that of the SWP and energy deposition to one depositing carbon with a few 100 eV cannot be achieved at high deposition rates (~a few nm/s) with bias voltages of a few keV. This is presumably the reason why the high conductive carbon is deposited by the combination of the SWP and the high voltage bias power source.

As possible reasons why the deposition rate is decreased at high V_B may be due to the change of carbon structure or due to the film sputtering.

The change of the carbon structure will be discussed later in Chapter 3.5. In this section, sputtering rate of carbon is approximately evaluated based on the ion flux and the sputtering yield. The deposition rate at the non-bias application is 13.5 nm/s and the specific gravity is 1.3 as the carbon film is similar with a-C:H.[28] From these values, deposited carbon atom flux without the bias ($\Gamma_{\mathrm{C}}^{\mathrm{SWP}}$) is calculated to be ~$9 \times 10^{16}$ 1/cm^{2}s. At a bias voltage of 2.0 kV, where deposition rate is ~6 nm/s, specific gravity is 2.2 as the deposited carbon film is similar with graphite.[29] In this case, deposited carbon flux at V_{B}~2kV ($\Gamma_{\mathrm{C}}^{\mathrm{SWP\_PLS}}$) is ~$7\times 10^{16}$ 1/cm^{2}s. From these values, the difference of the carbon deposition flux $\Gamma_{\mathrm{C}}^{\mathrm{DEC}}$ (= $\Gamma_{\mathrm{C}}^{\mathrm{SWP}}$ - $\Gamma_{\mathrm{C}}^{\mathrm{SWP\_PLS}}$) is ~$2\times 10^{16}$ 1/cm^{2}s. On the other hand, sputtered carbon flux $\Gamma_{\mathrm{C}}^{\mathrm{SPU}}$ is evaluated from the ion flux and carbon sputtering yield by Argon ion ($\gamma_{\mathrm{Ar-C}}$). Stage current density (~2.8 mA/cm^2) is evaluated from stage current of the Figure 3.2 and the stage surface area, and $\Gamma_{\mathrm{C}}^{\mathrm{SPU}}$ is obtained to be ~1.7×10^{16} 1/cm^{2}s, taking into account $\gamma_{\mathrm{Ar-C}}$~1.0 at an Ar incident energy of 2.0 kV.[30] Evaluated $\Gamma_{\mathrm{C}}^{\mathrm{DEC}}$ and $\Gamma_{\mathrm{C}}^{\mathrm{SPU}}$ are similar and it can be concluded that the decrease of the deposition rate is mainly caused by the sputtering effect.

3.4.3 Stage position dependence

The effect of the ion energy on the film property was evaluated in chapter 3.3.2, showing that the high energy ion contributes to the enhancement of the electrical conductivity. In this section, effect of the stage position on the electrical conductivity is investigated changing the stage position from z = 8 to 16 cm. Figures 3.6(a), (b) and (c) show stage bias current, deposition rate, and sheet resistance, of the deposited film, respectively, as a function of the stage position at V_B = 2.0 kV. Stage bias current monotonically decreases with increasing the z position, which is almost similar with the spatial variation of the plasma density (Figure 3.3(a)). Deposition rate monotonically decreases with increasing the z position. This is presumably due to the decrease of the deposition precursor diffusing to the substrate with increasing the distance. It is also notable that the sheet resistance increases with increasing stage position. As shown in Figure 3.6(a), the stage current, which is proportional to the ion flux, monotonically decreases with increasing the z position. This result suggests the importance of the ion flux as well as the ion energy to the film surface for the conductive film deposition.

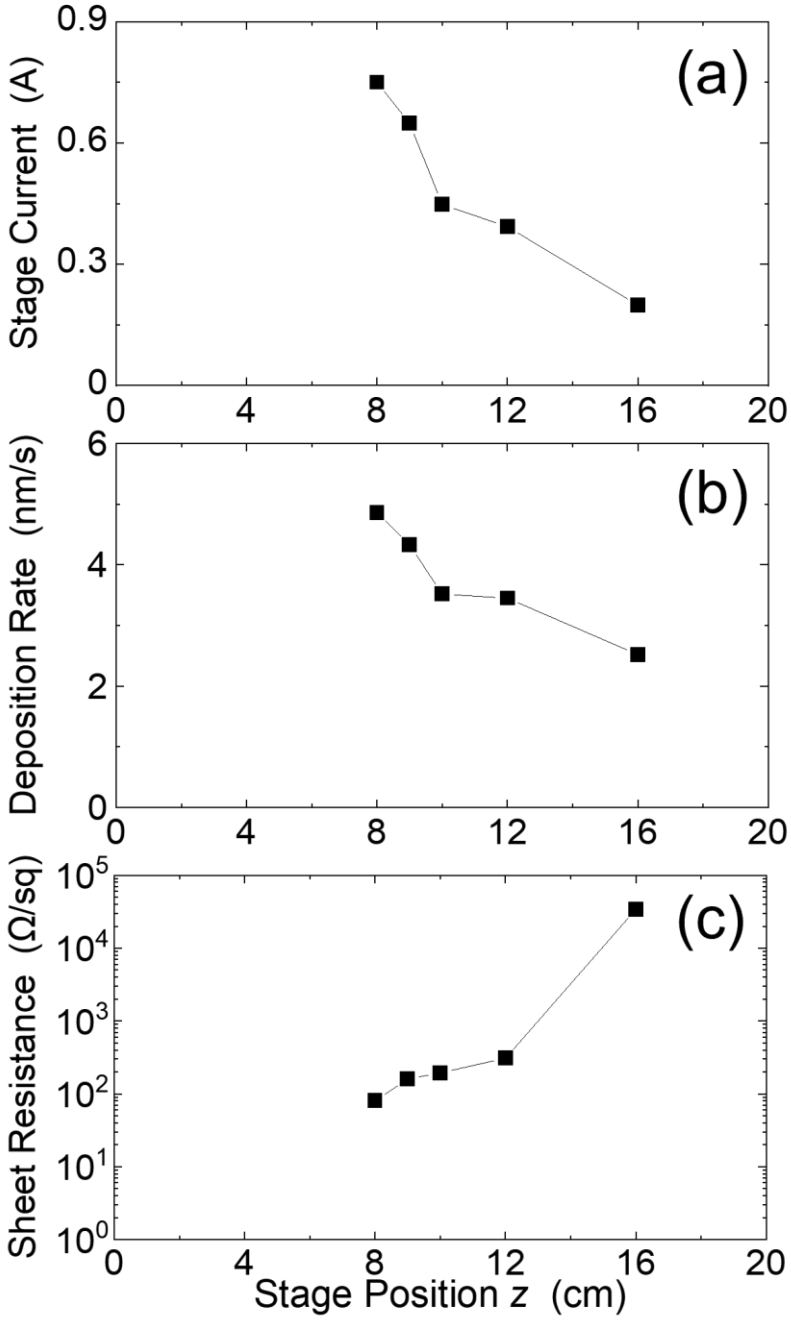

Figure 3.6 (a) Stage current, (b) deposition rate and (c) sheet resistance as a function of the stage position along *z* axis.

3.4.4 Benzene admixture-ratio dependence

C_6H_6 flow rate ratio is also varied from 25 sccm to 140 sccm at an Ar flow rate of 65 sccm. Total pressure and bias voltage are at 13 Pa and 2.0 kV, respectively. Figure 3.7 shows C_6H_6 flow-rate dependence of (a) stage bias current, (b) deposition rate and (c) sheet resistance of the deposited carbon film. It is known that addition of molecular gas into rare gas plasma decreases the plasma density due to increase of the power loss by dissociation, vibrational and rotational excitation of molecular gases. Decrease of the stage current with the C_6H_6 flow rate is presumably due to the decrease of the plasma density by adding C_6H_6. In Figure 3.7(b), deposition rate increases with increasing the C_6H_6 flow rate. The result suggests that, even though the plasma density decreases with the C_6H_6 addition, production rate of the deposition precursor from C_6H_6 is increased. In Figure 3.7(c), the sheet resistance increases at higher C_6H_6 flow rates above ~100 sccm. This result suggests that both the deposition rate increase and the ion flux decrease degrades the electrical conductivity of the carbon film.

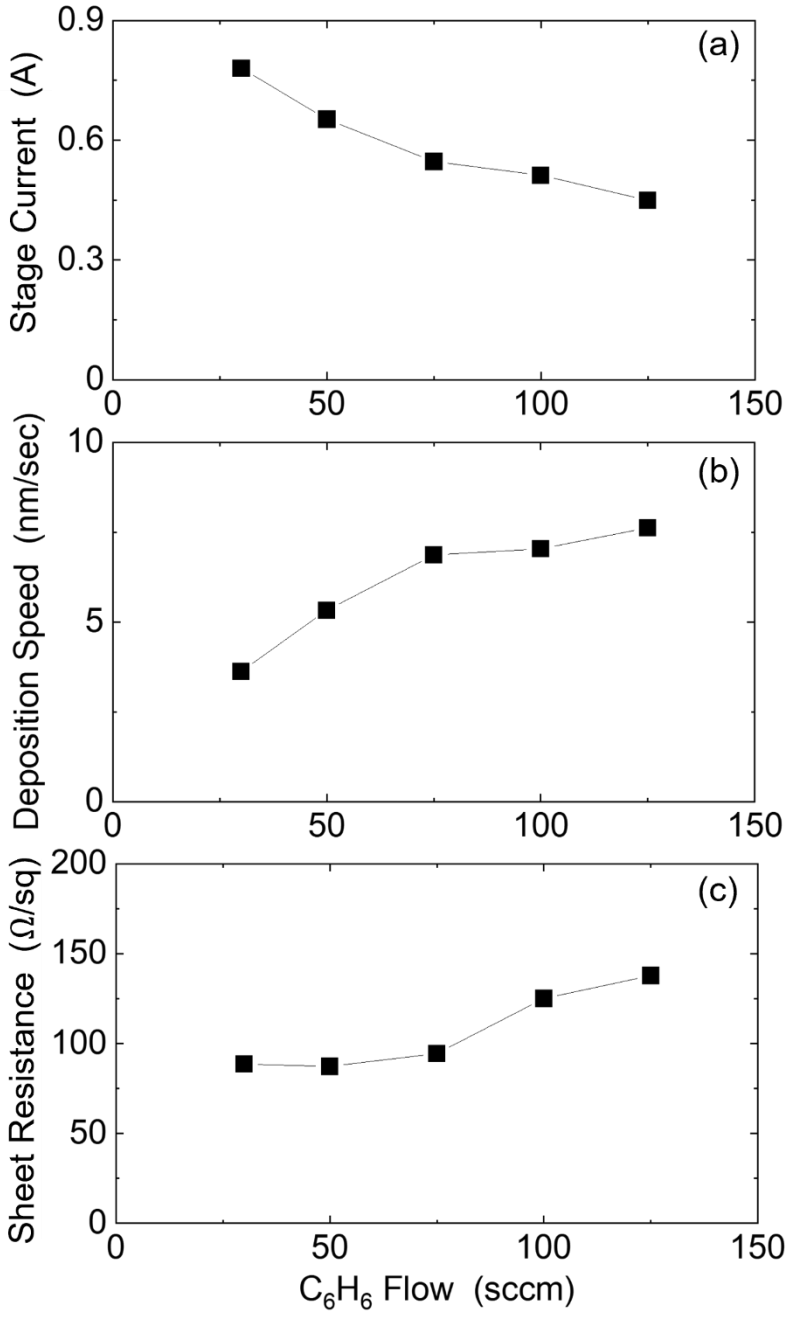

Figure 3.7 (a) Stage current, (b) deposition rate and (c) sheet resistance as a function of the stage position along *z* axis.

3.5 Change of carbon structure by ion bombardment

In chapter 3.3, influence of ion energy, flux, stage position or C_6H_6 flow rate on the electrical conductivity of the carbon film is investigated. The increase of the electrical conductivity implies the change of the film structure, *i.e.*, increase of the sp^2 structure in the film. In this section, the change of the carbon structure is evaluated by various methods, *i.e.*, Raman spectroscopy, FTIR, XRD, XPS, STEM and EELS.

3.5.1 Raman spectroscopy

Films are evaluated by Raman spectroscopy using visible light at a wavelength of 532 nm. It is known that Raman spectrum of carbon film is composed of two peaks, *i.e.*, G-peak (graphite peak: 1520 ~ 1600 cm^{-1}) and D-peak (disorder peak: 1340 ~ 1380 cm^{-1}), and that the G-peak shift and the I(D)/I(G) ratio are good indexes to evaluate the film structure.[3,6,8-26,31] To evaluate the G-peak shift and the I(D)/I(G) ratio, the Raman spectrum is separated into I(D) and I(G) peaks as shown in Figure 3.8. Figure 3.9(a) shows normalized Raman spectra of deposited films at bias voltages from 0.5 to 2.0 kV. By increasing the bias voltage, both increase of the D-peak relative intensity and G-peak shift to higher wavenumbers are observed. To evaluate the G-peak position and the I(D)/I(G) ratio more precisely, G- and D-peaks are separated

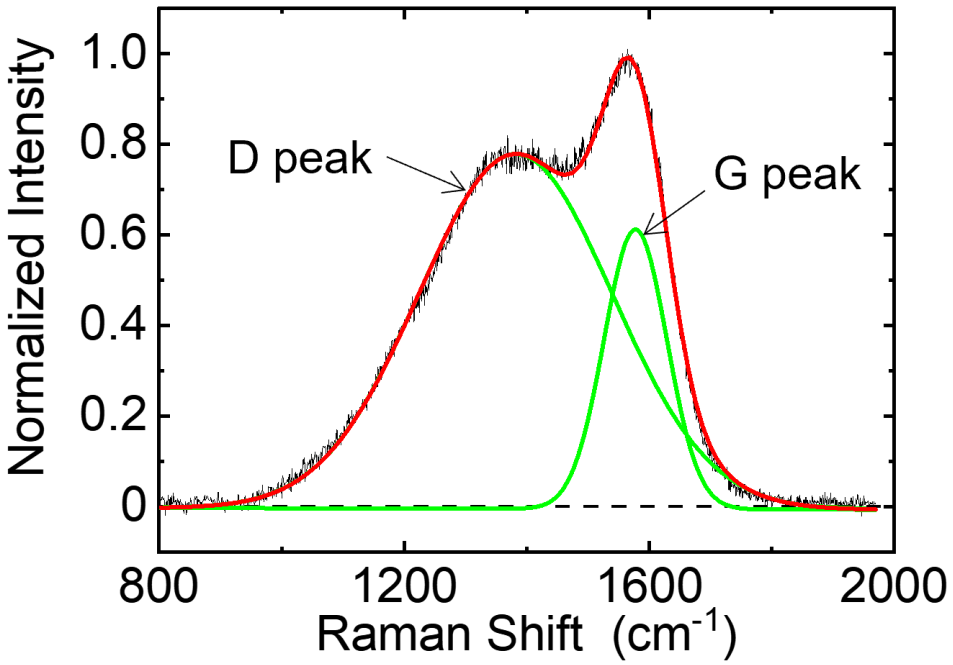

Figure 3.8 The peak separation of Raman spectrum by *I*(D) peak and *I*(G) peak.

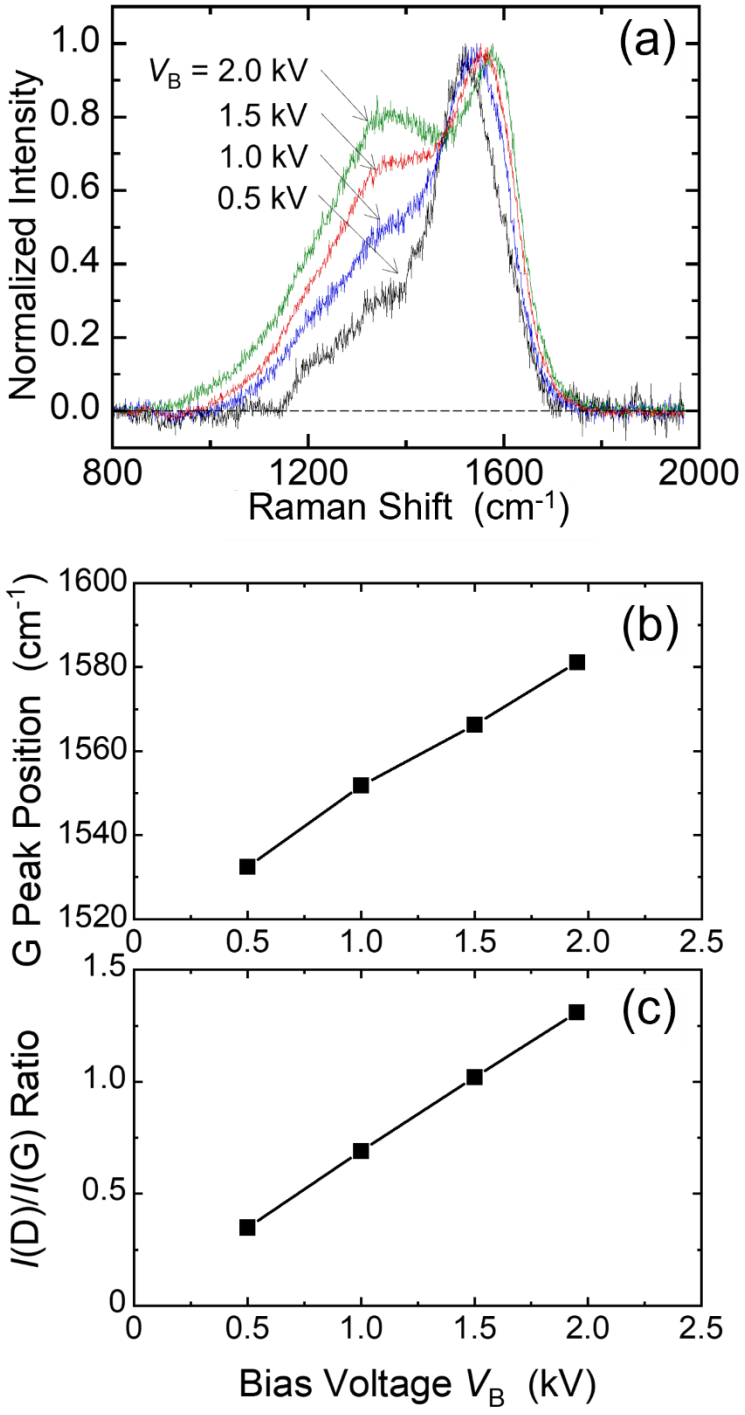

Figure 3.9 Bias voltage dependences of (a) Raman spectra, (b) G peak position and (c) I(D)/I(G) ratio.

using Gaussian curve fitting. Figures 3.9(b) and (c) show the bias voltage dependence of the G peak position and the I(D)/I(G) ratio, respectively. Both the G-peak position and the I(D)/I(G) ratio monotonically increases with increasing the bias voltage. Ferrari and Robertson[6,31] have reported the relation between Raman spectrum and carbon structures (tetrahedral amorphous carbon (ta-C), amorphous carbon (a-C), nanocrystalline graphite (NCG), and graphite) from the viewpoint of the G-peak position and the I(D)/I(G) ratio. Among carbon structures, G-peak shift to lower wavenumber is apparent in the case of a-C and the I(D)/I(G) ratio has its maximum in the case of NCG. From these facts, we can conclude that the deposited film structure changes from a-C to NCG with increasing the bias voltage. The change of the film structure from a-C to NCG suggests the increase of the sp^2 composition. This is qualitatively consistent with the result of Figure 3.5(b), *i.e.*, decrease in the sheet resistance at higher bias voltages.

Furthermore, it is possible to estimate the size of the sp^2 cluster in the carbon film. Ferrari and Robertson[31] introduced the model between the I(D)/I(G) ratio and the sp^2 cluster size L_a as follows,

$$\frac{I(D)}{I(G)} = C'(\lambda)L_a^2. \qquad (3.2)$$

Here, $C'(\lambda)$ is the Raman coupling coefficient, and is $\approx$0.0055 at a laser wavelength of 514 nm. This value of $C'(514\,nm)$ is adopted for the present L_a calculation because the wavelength of Raman spectroscopy used in this study (532 nm) is very close to 514 nm. The

evaluated L_a is ~15 Å, and the result suggests that the nano-sized sp^2 cluster exists in the carbon film.

3.5.2 *Fourier transform infrared spectroscopy*

FTIR is one of convenient techniques to evaluate hydrogen content in the film because C-H bond absorbs infra-red light at wavenumbers of 2800~3200 cm^{-1}.[6,32,33] In Figure 3.10(a), absorption coefficient spectra are shown for the carbon films deposited at V_B = 0.5, 1.0, 1.5 and 2.0 kV. The peak absorption coefficient monotonically decreases with increasing the V_B as shown in the figure. The C-H bond absorption peak is composed of various vibration modes and can be separated. M. Veres *et al.*[32] reported detailed analysis of the C-H absorption spectrum considering vibration modes such as CH_3 sp^3-asymmetric (2873 cm^{-1}), CH_2 sp^3-asymmetric (2928 cm^{-1}), CH_2 sp^2-symmetric (2973 cm^{-1}), CH sp^2-olefin (3026 cm^{-1}) and CH_2 sp^2-asymmetric (3058 cm^{-1}). Figure 3.10(b) shows separated absorption spectra from Figure 3.10(a) based on their report.

It is possible to calculate hydrogen content n_H in the carbon film by FTIR. The H content n_H in the film is obtained from following equation,

$$n_H = A_s \int \frac{\alpha(\nu)}{\nu} d\nu \ . \qquad (3.3)$$

Here, ν, α and A_s are wavenumber, absorption coefficient and coefficient of CH absorption, respectively. A_s value is reported as 8.7×10^{20} cm^{-2}.[33] To evaluate n_H, the FTIR spectrum of the carbon film is separated by

each C-H bonds peak as Figure 3.10(b). Figure 3.11(a) shows the C-H stretching absorption coefficient spectra of carbon films at V_B = 0.5-2.0 kV. Bias voltage dependence of the H content is shown in Figure 3.11(b). Similar to ref. 34, the H content monotonically decreases with increasing the V_B, suggesting the effect of the ion bombardment on the H reduction in the film. At bias voltages above 1.5 kV, the H content is less than 6×10^{21} cm^{-3} which corresponds to the H atomic composition less than ~5%. This shows that the deposited carbon film mostly consists of carbon atoms at higher V_B.

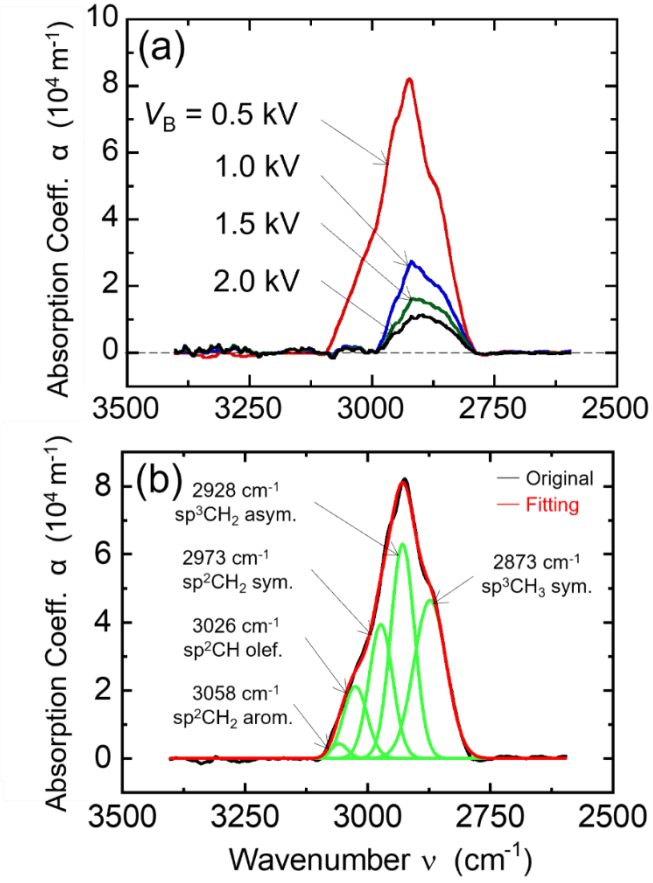

Figure 3.10 (a) C-H stretching absorption coefficient spectra of carbon films at V_B=0.5-2.0 kV. (b) Peak separation of FTIR spectrum by CH vibration modes.

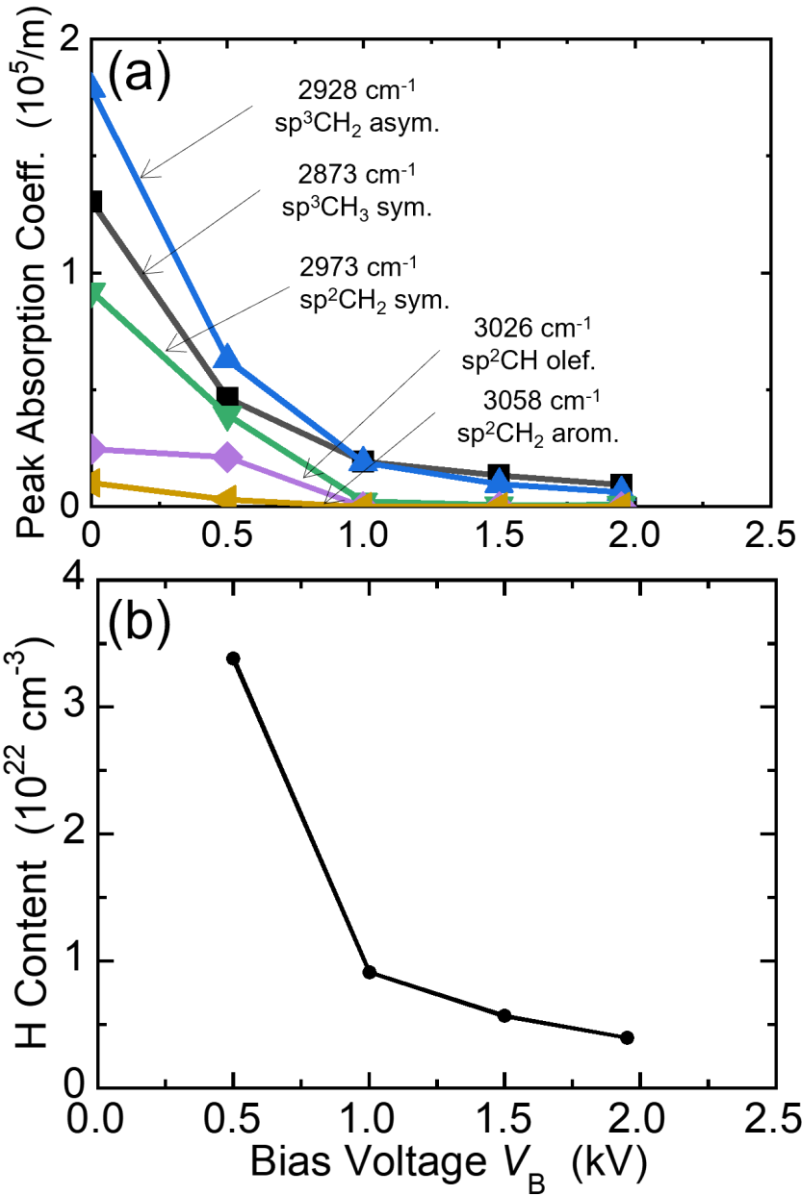

Figure 3.11 Bias voltage dependences of (a) peak absorption coefficient of each C-H bonds and (b) H content.

3.5.3 X-ray photoelectron spectroscopy and X-ray diffraction

High conductive film composition is evaluated by XPS. Monochromatized Al Kα is used for excitation source. The XPS chamber is pumped down to ~10^{-7} Pa. Before the XPS analysis, surface is cleaned by Ar ion sputtering at an energy of 0.5 keV with 50° incident angle. Electron emission angle is 0°. Figure 3.12(a) shows XPS wide-range spectrum (binding energy: 200 ~ 1350 eV) for high conductive film deposited at a bias voltage of 2.0 kV. From the spectrum, no apparent peak except for carbon is observed. Figure 3.12(b) shows XPS spectra of the films deposited at bias voltages from 0.5 to 2.0 kV. Each spectrum is composed of 3 peaks, *i.e.*, sp^2 (284.5±0.1 eV), sp^3 (285.3±0.1 eV) and C-O bond (286.5±0.1eV)[8,21,24,34]. These components are also indicated in the figure. The sp^2 bond obviously increases by increasing the bias voltage from Figure 3.12(b). Figure 3.13 shows sp^2/sp^3 content ratio as a function of the bias voltage. The sp^2/sp^3 content ratio monotonically increases from ~1.0 to ~3.1 by increasing the bias voltage. This result is consistent with the sp^2 bond variation evaluated by Raman spectroscopy. From the detailed investigation of C1s XPS peak, monotonic increase of sp^2/sp^3 ratio is observed up to ~3 at V_B = 2.0 kV, as shown in Figure 3. 13.

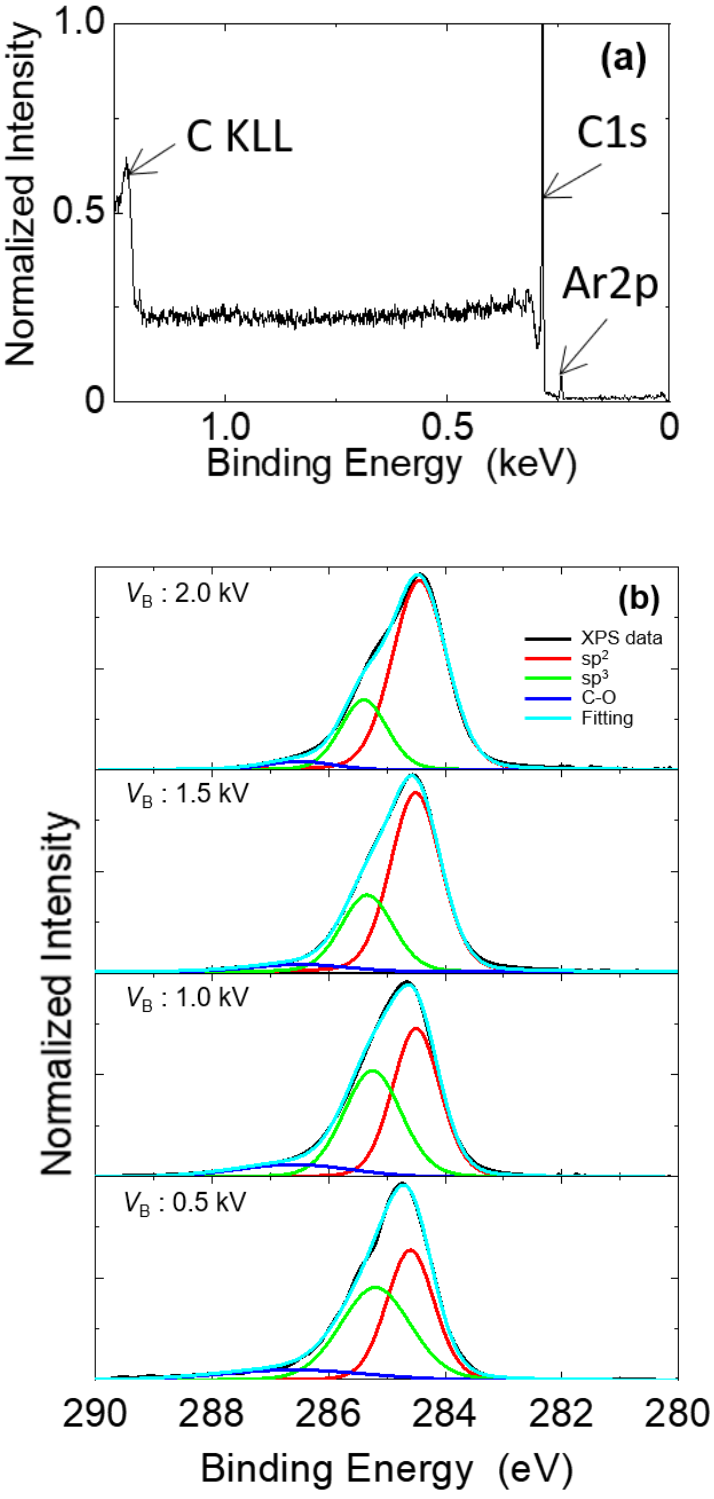

Figure 3.12 (a) XPS survey data of high conductive film (V_B=2.0 kV). (b) Bias voltage dependence of XPS spectra with C1s peak separation (sp^2, sp^3 and C-O).

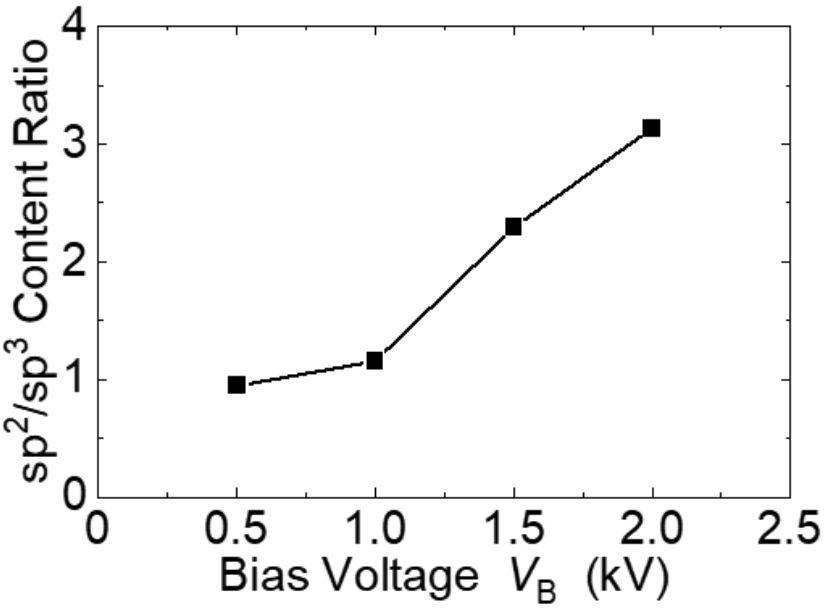

Figure 3.13 Bias voltage dependence of sp^2/sp^3 content ratio.

In addition to the above film evaluation, film structure was investigated by X-ray diffraction (XRD). Cu Kα radiation was used for XRD analysis. Anode power was 1.2 kW. Incident angle was changed from 0.1° to 5° with 0.1° interval. But no apparent peak was observed both from in-plane and from 2θ methods from 15° to 80°. From the above measurements, conductive carbon film deposited in this study was considered to be high conductive carbon film presumably with very small sp^2 clusters in the film which has been introduced by Robertson in Ref [6].

3.5.4 Scanning transmission electron microscopy and electron energy loss spectroscopy

To investigate the structure of deposited carbon film at V_B = 2.0 kV in more detail, I also performed aberration-corrected scanning transmission electron microscopy (STEM) and electron energy loss spectroscopy (EELS) at an electron beam energy of 200 kV and an EELS energy dispersion of 0.1 eV/channel. The EELS is set to dual EELS mode with zero-loss peak. Figure 3.14(a) shows typical TEM image, and no distinguished crystal structure is observed in the figure. Figure 3.14(b) shows EELS spectrum of carbon K-edge. The EELS spectrum is close to the graphitized carbon spectrum in Ref.[35]. Figure 3.14(c) shows mapping of C_K edge sp^2 bonding intensity (284.9 ± 0.7 eV). The

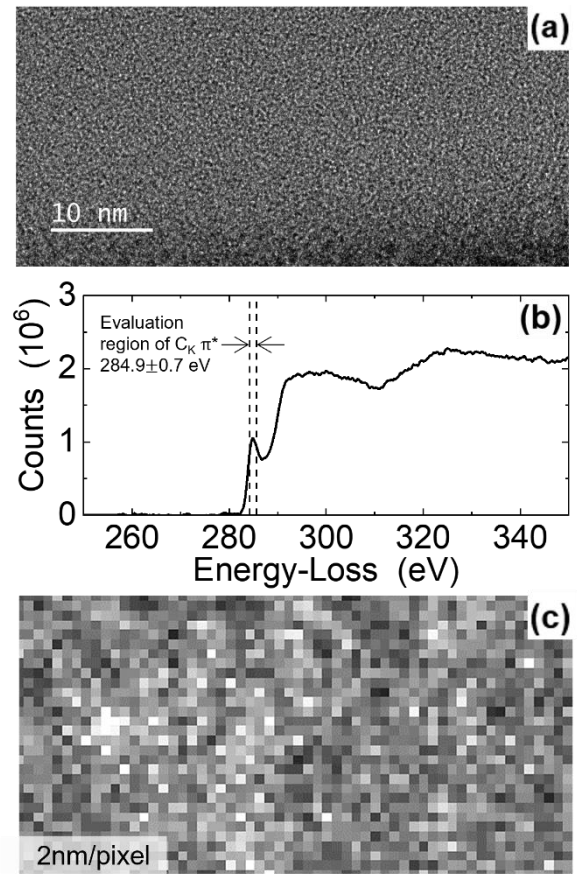

Figure 3.14 (a) TEM image of carbon film (V_B=2.0 kV), (b) EELS spectrum and (c) C_K edge sp^2 mapping.

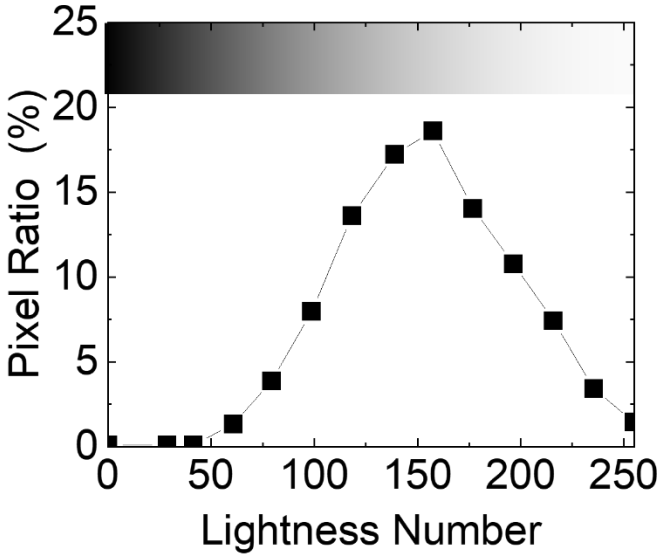

Figure 3.15 Pixel ratio by lightness.

white lightness of the pixels in Figure 3.14(c) indicates relative intensity of sp^2 bond in the carbon film. To investigate sp^2 cluster distribution by the EELS mapping, the mapping picture is separated by lightness as shown in Figure 3.15. The lightness is ranged from 0 (black: 0 of the counts) to 255 (white: the maximum of the counts). The region over the light number 127, a half of the count peak, is considered as the sp^2 cluster dominant region. And the ratio of pixels to the sum of the lightness number >127 is $\approx$ 73%. So, it is considered that a lot of nano-sized sp^2 clusters are distributed in the carbon film deposited at high bias voltage.

3.6 Conclusion

A method of high conductive carbon film deposition using the SWP source with high-voltage pulse power supply was proposed. The plasma properties, as well as deposited carbon film properties, were evaluated. The spatial distribution of the plasma density was evaluated using the Langmuir probe. High density plasma ($\sim 4 \times 10^{17}$ /m^3) with spatially uniformity along with the width of chamber (~35 cm) at the stage surface position was generated. The carbon film was deposited at various bias voltages. The sheet resistance and deposition rate decreased by increasing the bias voltage. At the high bias voltages $\geq$1.5 kV, the high conductive carbon film was deposited. From the evaluation of the carbon structure, hydrogen content decreases and sp^2 content increases was observed by increasing the bias voltage. The structure of the high conductive carbon film was amorphous with the nano-sized sp^2 clusters.

These results indicated that a higher ion incident energy was important for enhancing the carbon film conductivity.

References

[1] T. Ishijima, H. Toyoda, Y. Takanishi and H. Sugai: *Jpn. J. Appl. Phys.* **50** (2011) 036002.

[2] A. Itoh, A. Inokuchi, S. Yasuda, A. Teramoto, T. Goto, M. Hirayama and T. Ohmi: *Jpn. J. Appl. Phys.* **47** (2008) 2515.

[3] J. Kim, M. Ishihara, Y. Koga, K. Tsugawa, M. Hasegawa and S. Iijima: *Appl. Phys. Lett.* **98** (2011) 091502.

[4] Y. Hotta, H. Toyoda and H. Sugai: *Thin Solid Films* **515** (2007) 4983.

[5] S. Somiya, H. Toyoda, Y. Hotta and H. Sugai: *Jpn. J. Appl. Phys.* **43** (2004) 7696.

[6] J . Robertson: *Mater. Sci. Eng. R Rep.* **37** (2002) 129.

[7] L.K. Cheah, X. Shi, B.K. Tay and E. Liu: *Surf. Coat. Technol.* **105** (1998) 91.

[8] Y. Wang, L. Wang, G. Zhang, S.C. Wang, R.J.K. Wood and Q. Xue: *Surf. Coat. Technol.* **205** (2010) 793.

[9] A.A. Ogwu, R.W. Lamberton, P.D. Maguire and J.A. McLaughlin: *J. Phys. D: Appl. Phys.* **32** (1999) 981.

[10] M. A. Tamor and W. C. Vassell: *J. Appl. Phys.* **76** (1994) 3823.

[11] A.N. Obraztsov, E.A. Obraztsova, A.V. Tyurnina and A.A. Zolotukhin: *Carbon* **45** (2007) 2017.

[12] M. Yudasaka, R. Kikuchi, T. Matsui, H. Kamo, Y. Ohki, S. Yoshimura and E. Ota: *Appl. Phys. Lett.* **64** (1994) 842.

[13] J. Sun , N. Lindvall, M. T. Cole, T. Wang , T. J. Booth, P. Bøggild, K. B. K. Teo, J. Liu and A. Yurgens: *J. Appl. Phys.* **111** (2012) 044103.

[14] D. Noll, P. Hönicke, Y. Kayser, S. Wagner, B. Beckhoff and U. Schwalke: ECS *J. Solid State Sci. Technol.* **7** (2018) Q3108.

[15] N. Weber, A. Binder, M. Kettner, S. Hirth, R. T. Weitz and Ž. Tomović: *Carbon* **112** (2017) 201.

[16] A.N. Obraztsov, A.V. Tyurnina, E.A. Obraztsova, A.A. Zolotukhin, B. Liu, K. Chin and A.T.S. Wee: *Carbon* **46** (2008) 963.

[17] T. Schumann, M. Dubslaff, M.H. Oliveira Jr, M. Hanke, F. Fromm, T. Seyller, L. Nemec, V. Blum, M. Scheffler, J.M.J. Lopes and H. Riechert: *New J. Phys.* **15** (2013) 123034.

[18] S. K. Jerng, D. S. Yu, Y. S. Kim, J. Ryou, S. Hong, C. Kim, S. Yoon, D. K. Efetov, P. Kim and S. H. Chun: *J. Phys. Chem. C* **115** (2011) 4491.

[19] J. Kwak, S. Lee, H. Lee, G. Anoop, H. Lee, W. Kim, S. Ryu, H. Kim and J. Jo: *Appl. Phys. Lett.* **108** (2016) 123107.

[20] X. Li, W. Dai, Q. Wang, Y. Liang and Z. Wu: *Diam. Relat. Mater.* **106** (2020) 107818.

[21] M. Huang, X. Zhang and P. Ke, A. Wang: *Appl. Surf. Sci.* **283** (2013) 321.

[22] R. Kato and M. Hasegawa: *Carbon* **141** (2019) 768.

[23] V.A. Krivchenko, A.A. Pilevsky, A.T. Rakhimov, B.V. Seleznev, N.V. Suetin, M.A. Timofeyev, A.V. Bespalov and O.L. Golikova: *J. Appl. Phys.* **107** (2010) 014315.

[24] V.A. Krivchenko, V.V. Dvorkin, N.N. Dzbanovsky, M.A. Timofeyev, A.S. Stepanov, A.T. Rakhimov, N.V. Suetin, O.Yu. Vilkov and L.V. Yashina: *Carbon* **50** (2012) 1477.

[25] G. Kalita, M.S. Kayastha, H. Uchida, K. Wakita and M. Umeno: *RSC Adv.* **2** (2012) 3225.

[26] D. Liu, W. Yang, L. Zhang, J. Zhang, J. Meng, R. Yang, G. Zhang and D. Shi: *Carbon* **72** (2014) 387.

[27] P. J. Fallon, V. S. Veerasamy, C. A. Davis, J. Robertson, G. A. J. Amaratunga, W. I. Milne and J. Koskinen: *Phys. Rev. B* **48** (1993) 4777.

[28] L. Zhang, X. Wei, Y. Lin and F. Wang: *Carbon* **94** (2015) 202.

[29] Y. Lifshitz: *Diam. Relat. Mater.* **8** (1999) 1659.

[30] R. Behrisch, W. Eckstein: *Sputtering by Particle Bombardment* (Springer, Verlag Berlin/Heidelberg, 2007) Ch. 2.

[31] A.C. Ferrari and J.Robertson: *Phys. Rev.* **61** (2000) 14095.

[32] M. Veres, M. Koós and I. Pócsik: *Diam. Relat. Mater.* **11** (2002) 1110.

[33] H. Kojima, H. Kako, M. Terada, H. Sugai and T. Okuda: *Jpn. J. Appl. Phys.* **24** (1985) 1432.

[34] A. Ermolieff, A. Chabli, F. Pierre, G. Rolland, D. Rouchon, C. Vannuffel, C. Vergnaud and J. Baylet, M.N. Séméria*: Surf. Interface Anal.* **31** (2001) 185.

[35] L Ponsonnet, C Donnet, K Varlot, J.M Martin, A Grill and V Patel: *Thin Solid Films* **319** (1998) 97.

Chapter 4

Carbon deposition with electron cyclotron resonance plasma

4.1 Introduction

In Chapter 3, carbon film with a high electrical conductivity in an area of 18 × 3 cm^2 was successfully deposited by combining a high-density plasma source, *i.e.*, microwave surface-wave plasma (SWP), with a high-voltage (−2 kV) pulse power source for the substrate biasing.[22] It was also demonstrated that high flux and high-energy incident ions were the key factors for achieving high conductivity.

However, in the previous work, the bias voltage required for conductive film deposition was higher than −1.5 kV, and decrease in the bias voltage is preferable from the viewpoint of the cost of the power source. To deposit the conductive carbon film deposition at lower bias voltages, one solution is to improve the plasma source to increase the ion flux. For this purpose, an electron cyclotron resonance (ECR) plasma as an alternative high-density plasma source[1,2] is introduced in this chapter, in combination with the high-voltage pulse power source. The influences of the bias voltage application and the magnetic field configuration on the increase in the plasma density and the film electrical conductivity are investigated.

4.2 Experimental apparatus

Figure 4.1 shows a schematic of the experimental setup. A main chamber (length: 50 cm, width: 26 cm, height: 16 cm) and a small chamber (length: 50 cm, width: 8.4 cm, height: 9.1 cm) are connected and evacuated by a dry pump below 0.1 Pa. A waveguide (10.9 × 5.4 cm in cross-section) equipped with a slot plate (3 slots × 2 arrays) is attached to the small chamber through a vacuum-sealed quartz plate. An array of magnets (surface magnetic field: 0.57 T) is placed on the back of microwave-guiding quartz plates (thickness: 1 cm). Argon gas (65 sccm) is introduced into the main chamber. In the carbon film deposition, vaporized benzene (50 sccm) is added to the plasma from a gas manifold (length: 41 cm). The total pressure (p) is kept constant at 13 Pa. In the small chamber, plasma is generated by applying 2.45 GHz microwave power (P_{MW} = 2.1 kW) through the quartz plate and two microwave-guiding quartz plates. The Cartesian coordinates (x, y, z) are defined as shown in Figure 4.1, z = 0 is defined as the end position of the microwave-guiding quartz plates. A water-cooled substrate stage (surface area: 41 × 16.8 cm^2) is located at z = 4 cm, and a high-voltage negative pulse (maximum pulse voltage: −2 kV, pulse frequency: 500 Hz, pulse-on time (T_{PLS}): 0.2 ms) is applied to the stage. A high-voltage probe and a current probe are used to measure the voltage and the current of the stage. At p =13 Pa, Langmuir probe and optical emission spectroscopy (OES) are employed for time-resolved measurements of plasma density and emission intensity in pure Ar plasma. In the probe

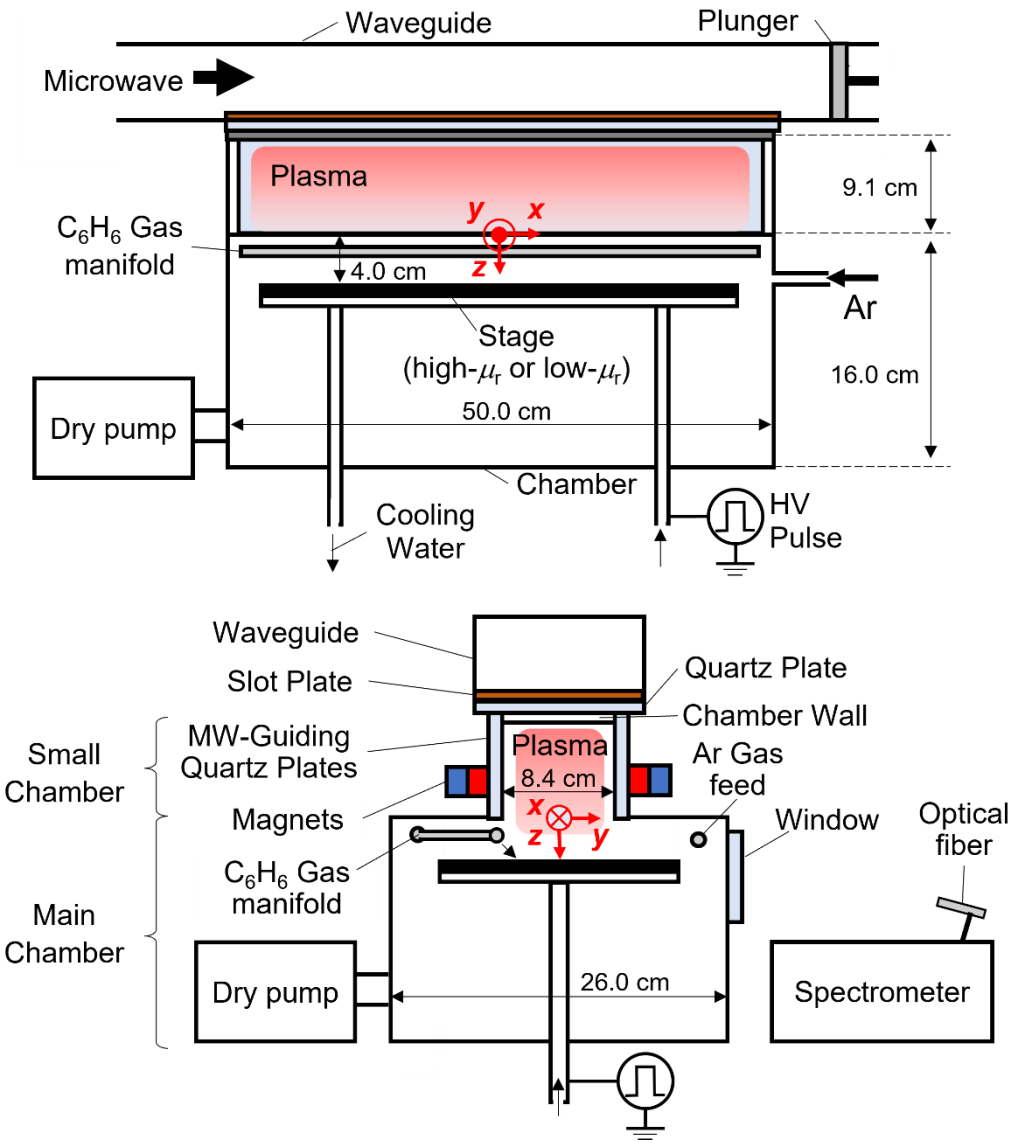

Figure 4.1 Schematic of experimental apparatus.

and OES measurements, the bias stage is covered with a graphite plate to simulate film-deposited surface conditions. In the carbon film deposition experiment, a silicon substrate (n-doped silicon (100), resistivity: 10.5 Ω·m, sheet resistance: 150 Ω/sq) is placed on the stage surface. Before the deposition, the substrate is cleaned by acetone with an ultrasonic cleaner . The substrate is then subjected to an Ar plasma at V_{PLS} = −1 kV for 1 min to pre-sputter a native oxide layer on the Si surface. After pre-sputtering, vaporized benzene is injected, and carbon films are deposited for 90 s. A step profiler is used to determine the film thickness. The sheet resistance of the carbon film is evaluated using a four-terminal sensing method. The carbon film structure is investigated *via* Fourier transform infra-red spectroscopy (FTIR) and Raman spectroscopy.

In this work, two types of magnetic field configurations in the vicinity of the stage are investigated, as well as their influence on the plasma and film properties. To achieve the field modification, two types of stage materials with different relative permeabilities (μ_r) are examined, namely, stainless steel (μ_r~1.1) and Ni-plated iron (μ_r~500). Figure 4.2 shows a simulated magnetic line of forces for two-stage materials using the COMSOL® Multiphysics software. The blue contour lines indicate the position at a magnetic field density of 87.5 mT, *i.e.*, ECR zone at a microwave frequency of 2.45 GHz. The magnetic field is shielded within the stage in the case of the Ni-plated iron stage (left side of Figure 4.2), and the magnetic lines of force outside the stage are near the direction of

the stage surface normal. However, in the case of the stainless-steel stage (right side of Figure 4.2), the stage does not affect the magnetic field, and the diverging magnetic field crosses the stage at inclined angles. The influence of the magnetic field configuration on plasma production will be discussed later.

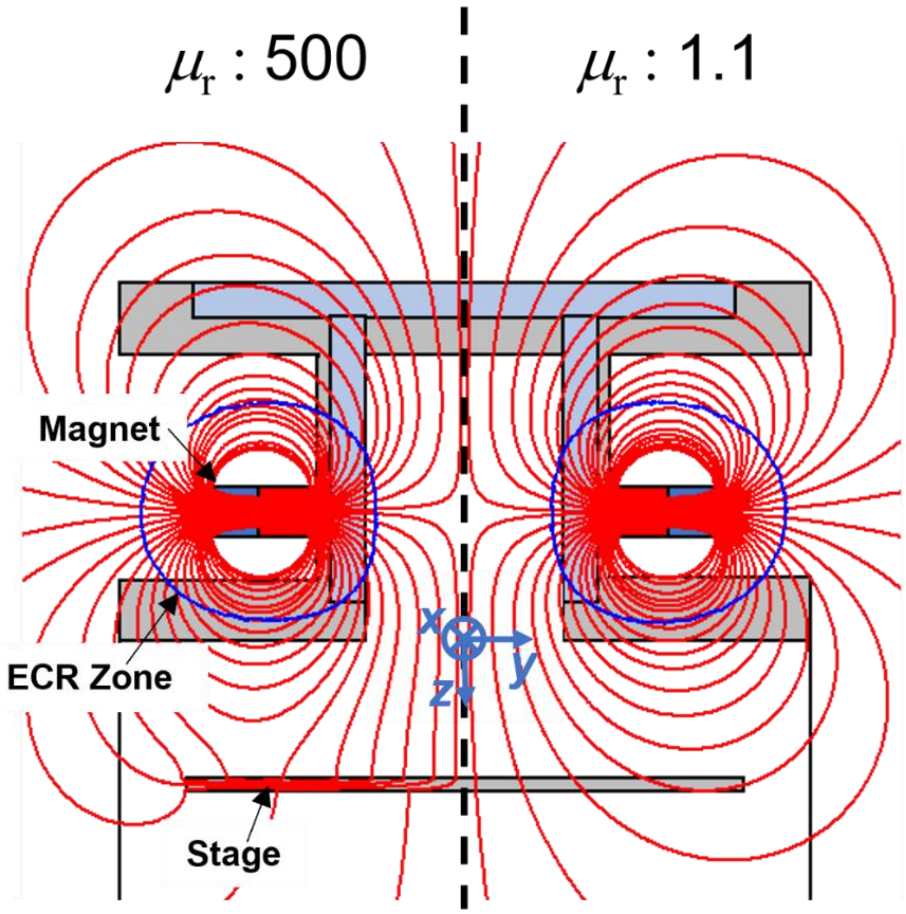

Figure 4.2 Magnetic line of force in the cases of stainless steel stage plate (μ_r: ~1.1) and Ni-plated iron stage plate (μ_r: ~500). Iso-magnetic field surface of 87.5 mT, *i,e.,* ECR zone, is also indicated in the Figure The maximum magnetic field on the quartz plate surface is 0.12 T.

4.3 Magnetic field evaluation

To confirm that the configuration of the magnetic field designed in the simulation is matched with the experiment, the *y* direction magnetic force B_y of the magnetic field in a small chamber is evaluated by Gauss meter. B_y on the surface of the microwave-guiding quartz is evaluated along the *z* direction and the *x* direction. Figure 4.3 (a) shows the spatial distribution of the B_y along *z* direction at $x = 0$ mm. Figure 4.3 (b) shows the spatial distribution of the B_y along *x* direction at $z = -38$ mm. The red and black plots in the figure shows measurement results by the Gauss meter at $y = -31$ mm and $y = 31$ mm with the stainless steel stage (μ_r~1.1), respectively. Solid curve in the figure shows simulated results. The measured results by the Gauss meter fit to the simulation result. Therefore, the simulated magnetic field in Figure 4.2 is quite reliable.

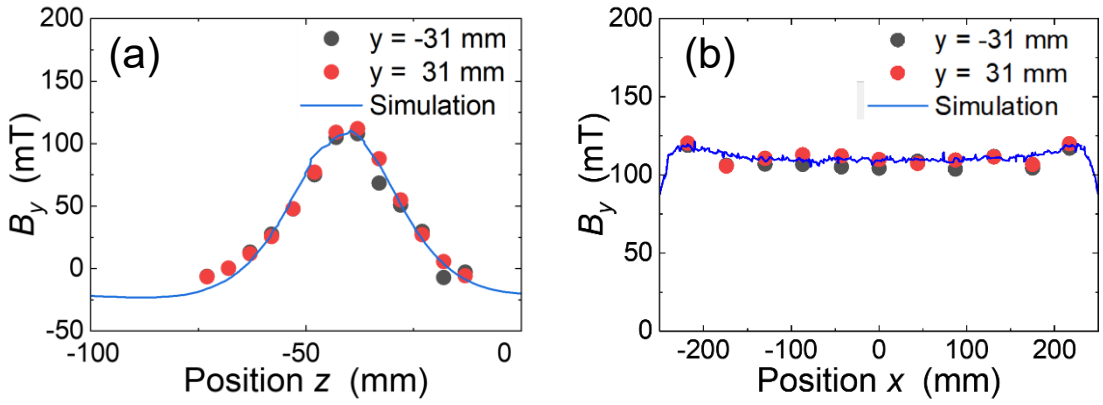

Figure 4.3 B_y spatial distribution of (a) *z* direction at x=0 mm and (b) *x* direction at z=-31 mm.

4.4 Stage current and plasma properties evaluation

4.4.1 Stage current evaluation

Figure 4.4(a) and (b) show typical stage voltage (V_{PLS}) and stage current (I_{PLS}) waveforms, respectively, for high-μ_r (red curve) and low-μ_r (black curve) stage materials. In both cases, the Ar pressure, microwave power and peak voltage are 13 Pa, 2.1 kW, and −1.0 kV, respectively, and the stage surface is covered with a graphite plate to maintain the same surface state as those of the carbon film depositions. Irrespective of the stage materials, the V_{PLS} immediately rises after turning on the pulse at $t = 0$ and maintains its voltage during the pulse-on period (0–0.2 ms). Contrarily, the I_{PLS} continues to increase during the pulse-on period. Furthermore, the stage material has a considerable influence on the current rise; the current of the low-μ_r stage is twice as great as that of the high-μ_r stage. Given that the I_{PLS} is dominated by plasma Bohm ion flux, the result indicates that the plasma density increases during the pulse-on time and that the density increase is influenced by the stage materials. This phenomenon occurs at the V_{PLS}>500 V. After turning off the pulse (t > 0.2 ms), both the V_{PLS} and I_{PLS} decay with time constants of ~0.05 ms. The reason for the $I_{PLS} = 0$ A at the t > 0.3 ms is the characteristic of the pulse generator. The different charge reduction between ECR plasma and SWP is originated from the different plasma density and the magnetic field near the stage. The pulse

generator has a switching circuit. When the pulse power is off, the switch is turned off, and the load circuit is electrically floating.

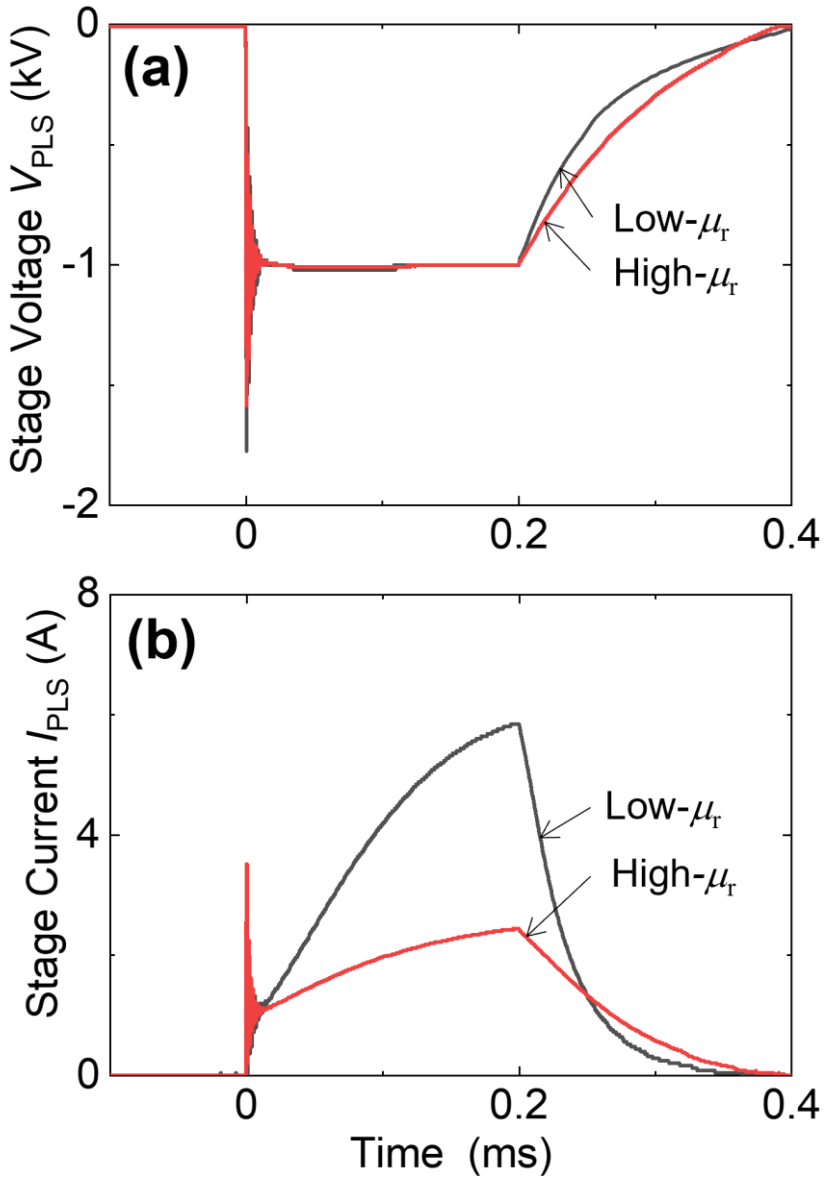

Figure 4.4 (a) stage voltage and (b) stage current waveform at V_{PLS} = 1.0 kV, f = 500 Hz, duty ratio = 10% in the cases of high-permeability Ni-plated iron plate (μ_r~500, red curve) and low permeability stainless-steel plate (μ_r~1.1, black curve).

4.4.2 Time-resolved measurement of plasma by OES and Langmuir probe

In Chapter 3, *i.e.,* carbon film deposition employing a combination of non-magnetized SWP and high-voltage pulse biasing, apparent increase in stage current was not observed during the pulse-on phase. The difference in the current behavior between non-magnetized SWP and magnetized ECR indicates that the magnetic field helps the increase in the stage current during the pulse is on. The influence of the permeability of the stage on the stage current also suggests the importance of the magnetic field. To investigate the mechanism of the stage current increase, temporal variations of plasma characteristics are investigated *via* the Langmuir probe measurement and the OES.

ArI emission intensity (763.6 nm) for Ar ECR plasma is measured by the OES to examine the temporal change of the plasma caused by the high-voltage pulse. In the experiment, an optical fiber is placed outside the glass window on the side of the chamber at (x, y, z) = (0, 45 cm, 10 cm), and is oriented toward the origin of the axes. The emission from the plasma is detected by a spectrometer (focal distance: 50 cm, 1800 groove/mm, spectral resolution: 0.05 nm, optical fiber detection angle: 5.5°) equipped with a photo-multiplier tube. The photon signal is converted into voltage pulses (pulse width: 10 ns) and is measured *via* a photon-counting method using a time-resolved multichannel scaler. Figure 4.5 shows an Ar emission waveform at $V_{PLS} = -1.0$ kV, $P_{MW} = 2.1$ kW, $p = 13$ Pa, and low-μ_r stage. The intensity increases after turning on

the pulse at $t = 0$. The intensity lowers and returns to its initial value after the pulse is turned off. The emission waveform is similar to that of I_{PLS} in Figure. 4.4(b).

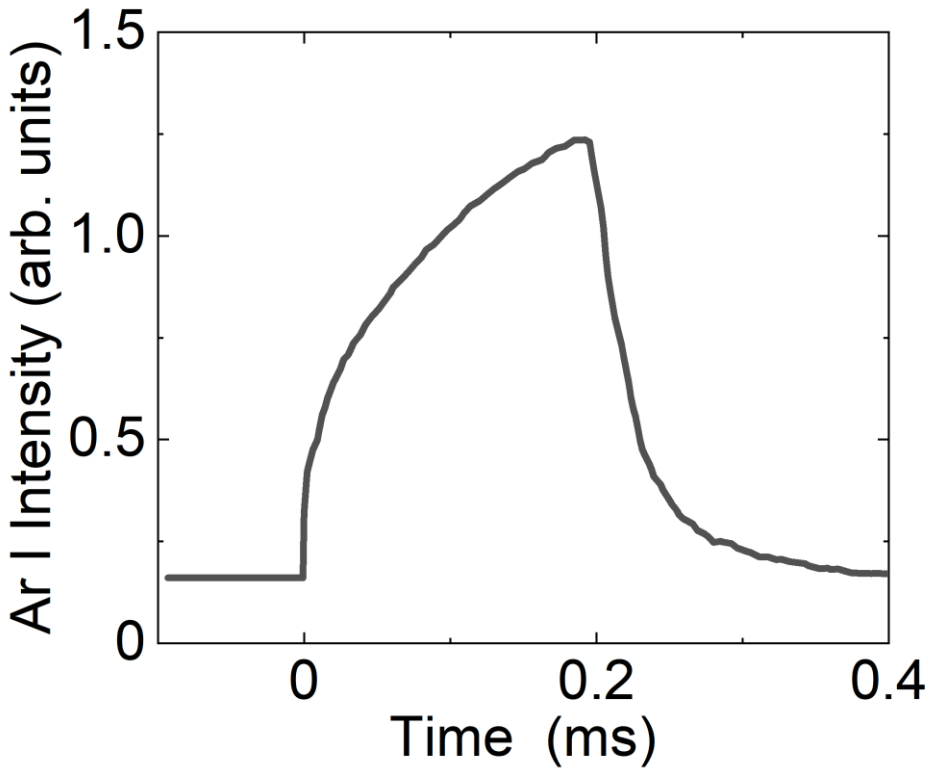

Figure 4.5 Time-resolved ArI (763.6 nm) emission intensity at V_{PLS} = 1.0 kV. The low-μ_r stage is used.

Under the same conditions, the plasma property is evaluated by

Langmuir probe (tip length: 5 mm, tip diameter: 0.2 mm), which is located at the origin of the axes. Figure 4.6(a) shows the temporal variations of the probe currents (I_{PRB}) at probe voltages (V_{PRB}) of 0, −5, −20, and −40 V. A pulse bias voltage of −1.0 kV is applied to the stage at t = 0. Negative probe current, *i.e.*, ion current, increases by turning on the pulse in the cases of V_{PRB} = −5, −20, and −40 V, except for the case of V_{PRB} = 0. The I_{PRB}'s time dependence is measured in various V_{PRB}, and then the I_{PRB} is re-plotted as a function of the V_{PRB} at timings shortly before the pulse's turn-on (t = −0.5 μs) and turn-off (t = 195 μs), as shown in Figure 4.6(b). The fall in plasma potential from 15 to 9 V, while the pulse is on, is apparently due to stage voltage biasing and its influence on the plasma. Notably, the electron saturation current for the *V-I* curve at t = 195 μs is more than two times larger than that at t = −0.5 μs. There is also an increase in the ion saturation current. The plasma density and the electron temperature are calculated using the result of Figure 4.6(b). Before the pulse bias power is introduced, the plasma density (n_0) and electron temperature (T_e) are ~8×10^{17} m^{-3} and 2.2 eV, respectively. When the pulse bias power is turned on, the values of n_0 and T_e are ~1.8×10^{18} m^{-3} and 3.5 eV, respectively. These results indicate that the plasma density is increased by applying the pulse bias voltage.

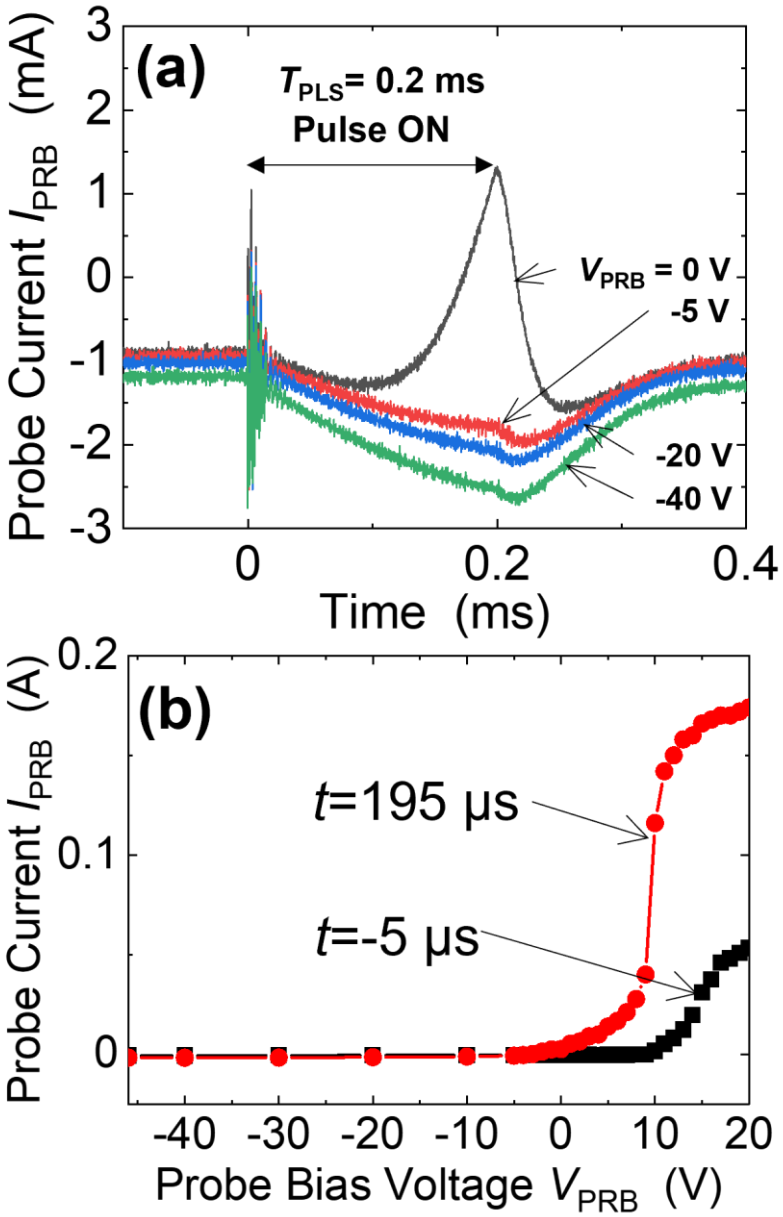

Figure 4.6 Time-resolved Langmuir probe measurement. (a) Temporal variation of the probe current at probe bias voltages of 0, −5, −30, and −40 V. (b) VI probe curves before pulse-on (t = −0.05 ms) and before pulse-off (t = 0.19 ms).

4.5 Zero-dimensional power balance model and its evaluation

4.5.1 Zero-dimensional power balance model with secondary electron ionization

The pulse power supplied to the stage is generally used for the acceleration of incident ions on the stage without affecting the plasma. In this plasma source, however, the pulse application induces the plasma density increase, and this means that the bias power is used not only for the ion acceleration but also for the plasma production. The high-energy secondary electron from the stage accelerated by the high bias voltage may be the cause of the ionization enhancement. This section discusses a power balance model that takes into account the effect of high-energy secondary electron injection into the plasma.

Figure 4.7 shows the schematic of the zero-dimensional power balance model, including the ionization by the secondary electron. The model considers the balance between absorbed power into the plasma and lost power from the plasma. With regard to the power absorption, two processes are considered, *i.e.*, power absorptions by continuous-wave microwave power ($P_{\mathrm{abs}}^{\mathrm{MW}}$) and by high-energy secondary electron ($P_{\mathrm{abs}}^{\mathrm{PLS}}$). The power loss from the plasma is expressed as $e\varepsilon_T n_0 u_B A$, where $e\varepsilon_T$, n_0, u_B, and A are the average energy carried by a pair of charged particles out of the plasma, averaged plasma density, Bohm

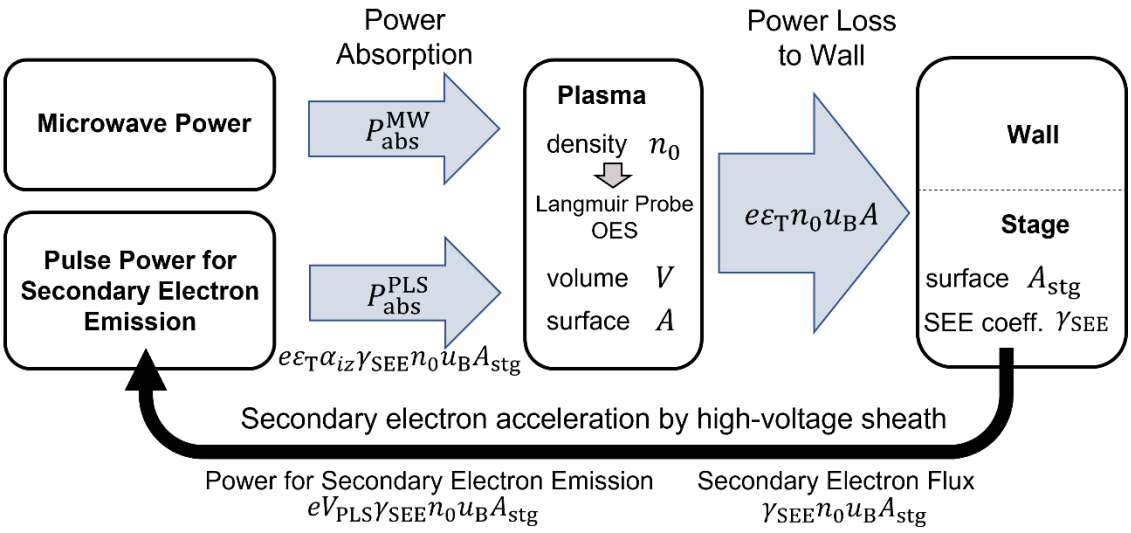

Figure 4.7 Schematic of power balance model.

velocity, and effective plasma surface area, respectively. Then, after being accelerated by the pulse bias voltage, a portion of the ions lost from the plasma impinge on the stage and form secondary electrons on the stage surface with a specific probability, *i.e.*, the secondary electron emission coefficient (γ_{SEE}). The bias voltage accelerates secondary electrons, and the flux to the plasma is expressed as $\gamma_{\mathrm{SEE}} n_0 u_{\mathrm{B}} A_{\mathrm{stg}}$, where A_{stg} denotes the effective surface area of the stage. The high-energy secondary electrons contribute to the ionization with a certain probability α_{iz}, where α_{iz} is number of ionization per one secondary electron and is a function of the bias voltage as well as ionization mean free path λ_{iz}. It should also be noted that α_{iz} is strongly influenced by the electron confinement time. The diverging magnetic field from the dielectric plate to the stage, as shown in Figure 4.2, tends to reflect energetic electrons from the quartz plate *via* the mirror effect. This implies that magnetic field configuration is an important factor in improving the α_{iz}. The specifics will be covered in Chapter 4.5.3.

Based on the above, the power balance equation in this system is described as follows:

$$e\varepsilon_{\mathrm{T}} \frac{dn_0}{dt} V = P_{\mathrm{abs}}^{MW} + e\varepsilon_{\mathrm{T}} \alpha_{iz} \gamma_{\mathrm{SEE}} n_0 u_{\mathrm{B}} A_{\mathrm{stg}} - e\varepsilon_{\mathrm{T}} n_0 u_{\mathrm{B}} A, \qquad (4.1)$$

where V denotes the plasma volume. Defining the loss frequency of charged particles ν_{loss} as the inverse of plasma confinement time

($\nu_{\mathrm{loss}} = 1/\tau_{\mathrm{loss}}$) and secondary-electron-induced ionization frequency as ν_{SEE}, these loss and ionization frequencies are expressed as follows:

$$\nu_{\mathrm{loss}} = \frac{u_{\mathrm{B}} A}{V}, \tag{4.2}$$

$$\nu_{\mathrm{SEE}} = \frac{\alpha_{iz} \gamma_{\mathrm{SEE}} u_{\mathrm{B}} A_{\mathrm{stg}}}{V} \quad . \tag{4.3}$$

Substituting equations. (4.2) and (4.3) into equation (4.1), and dividing the equation by $e\varepsilon_{\mathrm{T}} V$, the following particle balance equation per unit volume is obtained,

$$\frac{dn_0}{dt} = \frac{P_{\mathrm{abs}}^{MW}}{e\varepsilon_{\mathrm{T}} V} + n_0 \nu_{\mathrm{SEE}} - n_0 \nu_{\mathrm{loss}}. \tag{4.4}$$

The first, second, and third terms on the RHS are the applied microwave ionization rate, high-energy secondary electron ionization rate, and plasma loss rate, respectively. If the first term of the RHS is defined as the created ion-electron pair per unit volume and a second by microwave,

$$R^{MW} = \frac{P_{\mathrm{abs}}^{MW}}{e\varepsilon_{\mathrm{T}} V} \quad , \tag{4.5}$$

and $t = 0$ is defined as the pulse-turn-on time, the temporal variation of the plasma density after the pulse turn-on can be expressed from equations. (4.4) and (4.5) as follows:

$$n_0(t) = \frac{R^{\mathrm{MW}}}{\nu_{\mathrm{MP}}} + \left(\frac{R^{\mathrm{MW}}}{\nu_{\mathrm{loss}}} - \frac{R^{\mathrm{MW}}}{\nu_{\mathrm{MP}}}\right) e^{-\nu_{\mathrm{MP}} t}. \quad (4.6)$$

Here, ν_{MP} denotes the inverse of the time constant (τ_{MP}) for the plasma density increase during the pulse-on period and is described as follows:

$$\nu_{\mathrm{MP}} = \nu_{\mathrm{loss}} - \nu_{\mathrm{SEE}}. \quad (4.7)$$

After turning off the pulse, ionization due to the secondary electron does not exist ($\nu_{\mathrm{SEE}} = 0$), and the temporal variation of the plasma density can be expressed as follows:

$$n_0(t) = \frac{R^{\mathrm{MW}}}{\nu_{\mathrm{loss}}} - \left(\frac{R^{\mathrm{MW}}}{\nu_{\mathrm{loss}}} - \frac{R^{\mathrm{MW}}}{\nu_{\mathrm{MP}}}\right) e^{-\nu_{\mathrm{loss}}(t - T_{\mathrm{PLS}})}, \quad (4.8)$$

where T_{PLS} denotes the bias pulse duration time. A saturated plasma density can be found supposing a long-enough T_{PLS} as follows:

$$n_0^{\mathrm{MWPLS}} = \frac{R^{\mathrm{MW}}}{\nu_{\mathrm{MP}}}. \quad (4.9)$$

The steady-state plasma density without the pulse is

$$n_0^{MW} = \frac{R^{\mathrm{MW}}}{\nu_{\mathrm{loss}}} \quad . \quad (4.10)$$

From equations. (4.9) and (4.10), the plasma density ratio $n_0^{\mathrm{MWPLS}}/n_0^{MW}$

is

$$\frac{n_0^{\mathrm{MWPLS}}}{n_0^{MW}} = \frac{\nu_{\mathrm{loss}}}{\nu_{\mathrm{MP}}} = \frac{\tau_{\mathrm{MP}}}{\tau_{\mathrm{loss}}} \ . \tag{4.11}$$

Equation (4.11) demonstrates that the density ratio $n_0^{\mathrm{MWPLS}}/n_0^{MW}$ can be evaluated from the time constants measured from the temporal variation of the plasma during the pulse-on (τ_{MP}) and pulse-off (τ_{loss}).

4.5.2 Validation of the model

The above model discusses the time dependency of the plasma density. The Langmuir probe can be employed to assess the plasma density. In the case of constant electron temperature, the OES is also an excellent index for evaluating the relative variation of the plasma density. The validity of the power balance model is evaluated using Langmuir probe and OES measurements in this section. From the measured time constants τ_{MP} and τ_{loss}, the plasma density ratio $n_0^{\mathrm{MWPLS}}/n_0^{MW}$ is calculated using equation (4.11), and is compared with the measured $n_0^{\mathrm{MWPLS}}/n_0^{MW}$ from the Langmuir probe.

The black curves in Figures 4.8(a) and (b) show temporal variations of the Ar emission intensity and the ion saturation current in the Ar plasma during the pulse-on period, respectively, at $V_{\mathrm{PLS}} = -1.0$ kV and p = 13 Pa. The probe voltage is set at $V_{\mathrm{PRB}} = -40$ V to minimize the influence of the plasma potential shift during the pulse-on period.

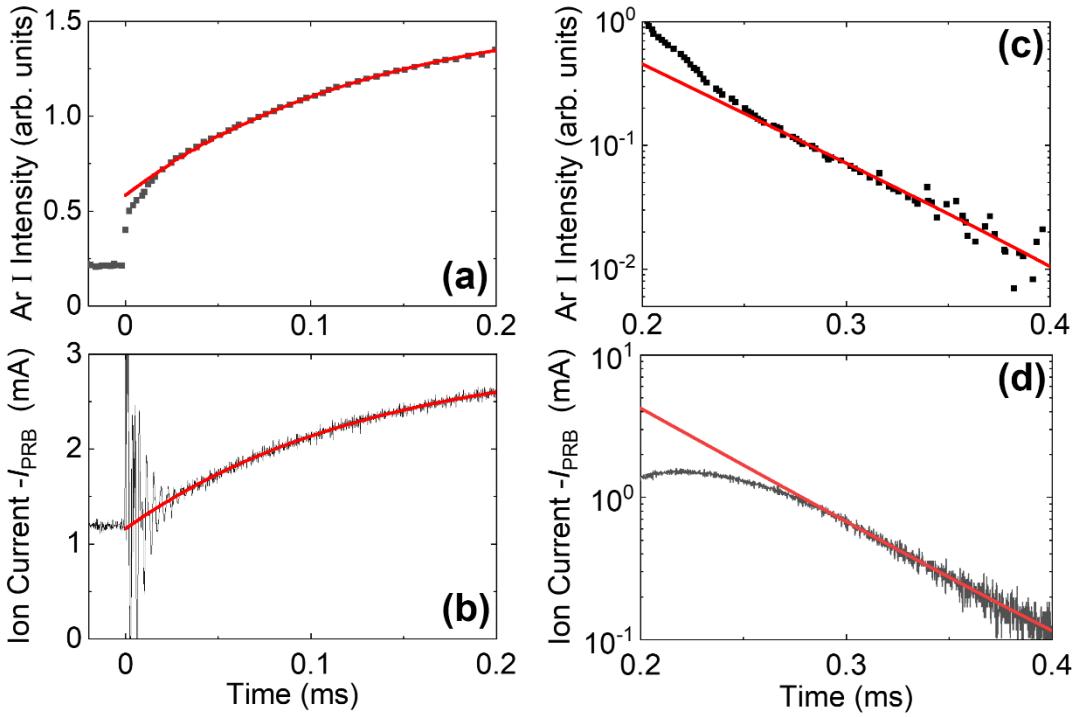

Figure 4.8 (a) Ar emission intensity and (b) probe ion current during the pulse-on period. (c) Ar emission intensity and (d) probe ion current during the pulse-off period. Black and red curves indicate the experimental results and best-fitted curves based on the power balance model, respectively. V_{PLS} = 1.0 kV.

Immediately after the pulse is turned on, the ArI signal slightly increases in a very short time. The abrupt increase in the emission intensity is presumably due to the increased excitation rate constant induced by high-energy secondary electrons. During the pulse-on period, the electron energy distribution is nearly identical because the secondary electron

flux is proportional to the ion flux to the stage, *i.e.*, to the bulk plasma density. After the first increase in the signal, both the ion saturation current and the emission intensity increase with a time constant equal to ν_{MP}. The best-fitted curves based on equation (4.6) are likewise indicated with red curves in Figures 4.8(a) and (b), and they suit the results extremely well, and the τ_{MP} obtained from the probe and the OES are virtually the same at τ_{MP} ~130 μs. From the best-fitted curve of the probe measurement, saturated ion current supposing long pulse-on time is obtained, and then the $n_0^{\mathrm{MWPLS}}/n_0^{MW}$ is obtained from the ratio of pulse-on I_{PRB} to pulse-off I_{PRB}.

The Ar emission and the ion saturation current during the pulse-off phase are shown with black curves on semi-logarithmic scales (Figures 4.8(c) and (d)). Except for the initial variation at t = 0.2–0.3 ms, the signals decline exponentially with nearly the same time constants of 55–58 μs in both cases. The variation in the ion saturation current is caused by an increase in plasma potential after the pulse is turned off. The variance in the intensity of the Ar emission is most likely caused by the remaining secondary electron contributing to the Ar excitation decaying its energy with the V_{PLS}. The same approach is used to derive τ_{MP}, τ_{loss}, and $n_0^{\mathrm{MWPLS}}/n_0^{MW}$ at V_{PLS} = −0.5 and −1.5 kV, as shown in Figure 4.9, where $\tau^{OES}$and τ^{PRB} indicate time constants evaluated from the OES and the Langmuir probe, respectively. As can be seen from Figure 4.9(a), τ_{MP} (squares) increases when $|V_{\mathrm{PLS}}|$ exceeds 0.5 kV owing to an increase in the contribution of secondary electron ionization at higher electron

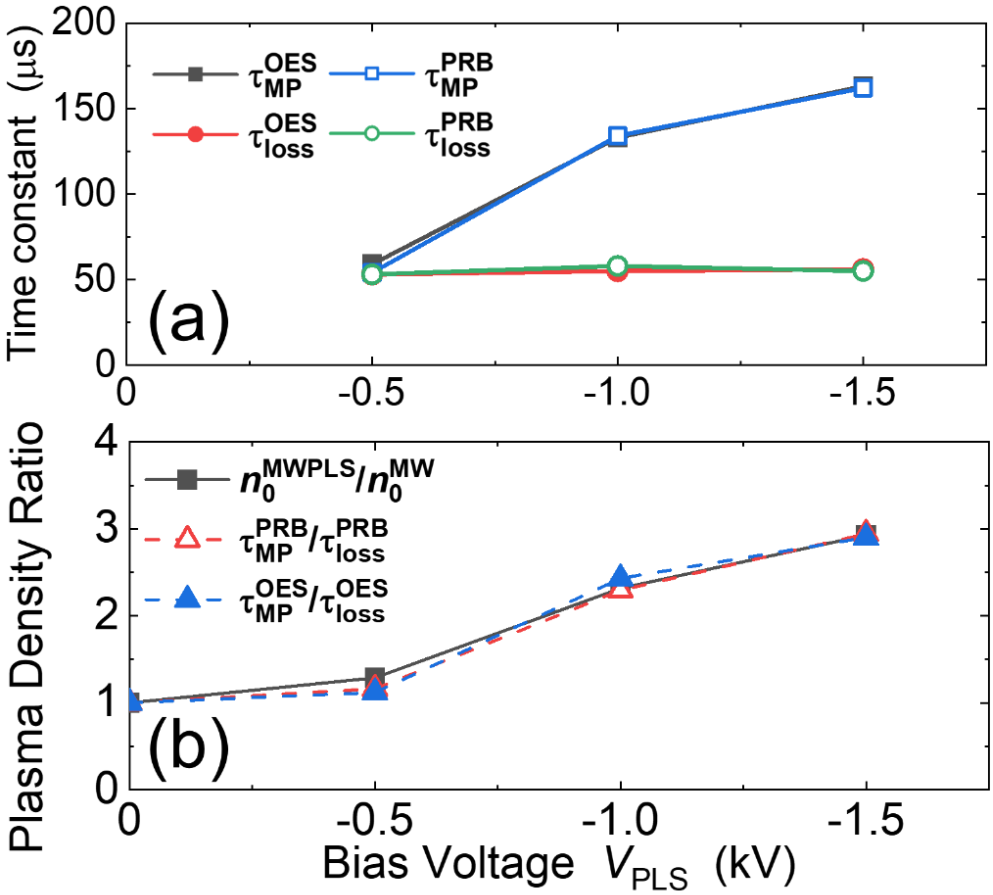

Figure 4.9 (a) τ_{MP} and τ_{loss} for OES and Langmuir probe. The square and circle indicate τ_{MP} and τ_{loss}, respectively. The filled and open colors indicate the measured data from OES and Langmuir probe, respectively. (b) Measured $n_0^{\mathrm{MWPLS}}/n_0^{MW}$ (squares with solid line) from the ratio of the ion saturation current, and the estimated $n_0^{\mathrm{MWPLS}}/n_0^{MW}$ from $\tau_{\mathrm{MP}}/\tau_{\mathrm{loss}}$. Open and filled triangles with broken lines indicate the estimated results from Langmuir probe and OES, respectively.

energies. Contrarily, τ_{loss} (circles) is almost the same irrespective of V_{PLS}, because τ_{loss} is influenced by the Bohm velocity and geometrical structure of the plasma.

To evaluate the τ_{loss}, parameters of equation (4.2) are roughly estimated as shown in Table 4.1. Although the plasma structure is influenced by the magnetic field, simple rectangular volume shown by red-shaded region in Figure 4.10 (5.2×10^{-3} m^3) is supposed in the present estimation. In the present magnetic configuration, plasma is mainly lost along the magnetic field from high- to low-field region, *i.e.*, toward the stage. Based on this, effective surface area of 3.4×10^{-2} m^2 is supposed, as shown in Figure 4.10. The Bohm velocity is ~2.2×10^3 m/s at an electron temperature of 2.2 eV. From these values, estimated τ_{loss} is ~67 μs, which fairly agrees with the experimental result (~57 μs). The difference of the τ_{loss} between the experiment and the estimation is presumably due to the simplification of the effective plasma volume and the effective surface area.

Figure 4.9(b) shows the comparison of the measured $n_0^{\mathrm{MWPLS}}/n_0^{MW}$ (squares with solid line) from the ratio of the ion saturation current and the estimated $n_0^{\mathrm{MWPLS}}/n_0^{MW}$ from $\tau_{\mathrm{MP}}/\tau_{\mathrm{loss}}$. Open and full triangles with broken lines represent estimated Langmuir probe and OES results, respectively. The estimated $n_0^{\mathrm{MWPLS}}/n_0^{MW}$ from both the Langmuir probe and the OES correspond well with the measured $n_0^{\mathrm{MWPLS}}/n_0^{MW}$, indicating the correctness of the suggested power balancing model. The ionization by the secondary electron is not enhanced at low bias voltages

Parameters	Value
A	3.4×10^{-2} m^2
V	5.2×10^{-3} m^3
γ_{SEE}	0.5

Table 4.1 Estimated parameters for effective plasma surface A, , secondary electron coefficient γ_{SEE} and volume of plasma V.

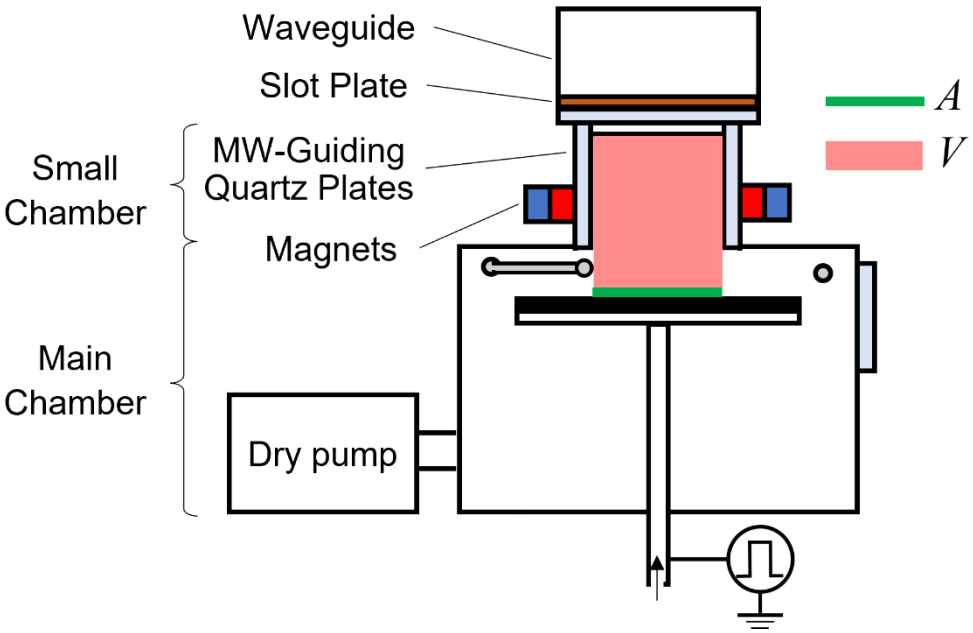

Figure 4.10 Region of effective area A and effective plasma volume V for the τ_{loss} estimation.

($|V_{\mathrm{PLS}}| \leq 0.5$ kV). However, at a bias voltage of $V_{\mathrm{PLS}} = -1.5$ kV, plasma density increases almost by a factor of three by applying the bias pulse power. It should be emphasized that the density ratio is the ratio of total absorbed power during the pulse-on to absorbed power just from the microwave power source. For example, $V_{\mathrm{PLS}} = -1.0$ kV; $n_0^{\mathrm{MWPLS}}/n_0^{MW} \sim 2$ is obtained. This means that power absorptions from the pulse power source are almost the same as those from the microwave power source. Although not all incident power is absorbed by the plasma, power absorptions from the microwave and DC pulse sources are approximated by the net microwave power and DC pulse power. The power for the secondary electron emission is calculated using the DC pulse power P_{PLS} and γ_{SEE} as $P_{\mathrm{PLS}} \times \gamma_{\mathrm{SEE}}/(1 + \gamma_{\mathrm{SEE}})$. The γ_{SEE} from the carbon surface at an Ar^+ incident energy of 1 keV is ~0.5.[3] P_{PLS} at $t = 195$ μs and $V_{\mathrm{PLS}} = -1.0$ kV is ~6 kW from Figure 4.4. Accordingly, the pulse power to the secondary electron acceleration is ~2 kW, which is almost comparable with the microwave power. This is consistent with the $n_0^{\mathrm{MWPLS}}/n_0^{MW} \sim 2$ finding, implying that secondary electrons contribute to the enhancement of the plasma density. As a result, the pulse power is effectively utilized for both the ion acceleration and the plasma generation.

4.5.3 *Influence of magnetic field structure*

As aforementioned, the stage current strongly depends on the relative permeability of the stage material as shown in Figure 4.4(b), and confinement of high-energy secondary electrons by the mirror effect is considered. The magnetic field is relatively strong near the small chamber, *i.e.*, near the permanent magnets, but is relatively weak near the stage. The magnetic moment of the secondary electrons released from the stage is affected by the relative permeability of the stage material due to the change in magnetic field direction to the sheath electric field. Electron trajectories are numerically estimated in non-collisional situations to discuss the mechanism. The magnetic field in the chamber is computed in the simulation for both non-magnetic and magnetic stages. The calculated magnetic field agreed well with the measured magnetic field of the plasma source using a Gauss meter. Next, as a model of the sheath, a uniform electric field perpendicular to the stage surface (z-direction) is defined in front of the stage surface with a 2 mm thickness and a −1.5 kV sheath voltage. The electrons are then ejected from the stage in the z-direction with a kinetic energy of 2 eV (initial kinetic energy). Both the electron momentum and the electron position are calculated by Lorentz force and the integration of the velocity based on eqs. (4.12) and (4.13),

$$\frac{d}{dt}(m_e\vec{v}) = e\left(\vec{E} + \vec{v} \times \vec{B}\right), \tag{4.12}$$

$$\frac{d\vec{r}}{dt} = \vec{v}. \tag{4.13}$$

Figure 4.11(a) shows a cross-sectional view of the simulation model in the *y*-*z* plane, along with examples of electron trajectories for low-μ_r (red curves) and high-μ_r (blue curves) stages. Electrons emitted from the stage center (y = 0) go straight to the facing wall along the z-axis in both materials. This is because the electron is emitted parallel to the magnetic field (see Figure 4.2) and is not affected by it. However, electron trajectories emitted at y = 30 mm significantly vary depending on the relative permeability (μ_r) of the stage. In the case of high-μ_r materials, the magnetic field on the stage is virtually perpendicular to the stage surface, resulting in a low magnetic moment of the electron and a very weak mirror effect near the magnets. In the case of the low-μ_r material, however, the electron is reflected at the strong magnetic field region in front of the magnets. This is because the electron has a large magnetic moment due to the large angle between the direction of the electron acceleration and the magnetic field. The reflected electrons by the magnetic mirror are then reflected by the sheath electric field, which results in longer electron confinement time and effective utilization of high-energy electrons for ionization of neutral species.

To evaluate the electron confinement efficiency, 100 electrons are emitted at the same spatial interval from y = 0 to 84 mm, and the ratio of confined electrons is evaluated at different stage materials. Figure 4.11(b) shows the confined electron ratio at μ_r = 1.1 and 500. Almost 60% of the secondary electrons are confined by using low-μ_r stage, but the confinement ratio is decreased to ~20% by using the low-μ_r stage.

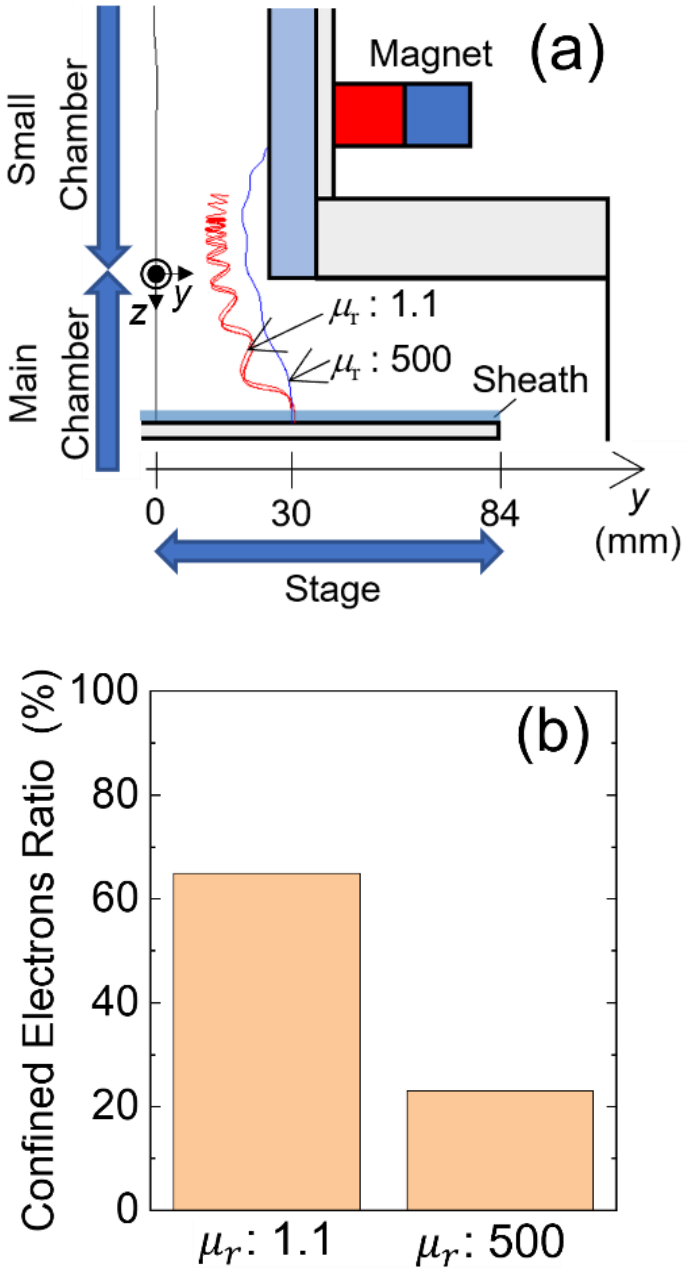

Figure 4.11 Electron trajectory simulation with different stage materials. (a) examples of electron trajectories for electrons emitted from $y = 0$ and 30 mm. Blue- and red-curves indicate trajectories with high- and low-μ_r stages, respectively. (b) Confined electrons ratio.

4.6 Application to conductive carbon film deposition

The effect of the stage permeability μ_r on carbon film deposition is evaluated. The bias voltage dependence of carbon film properties is investigated for the cases of high- and low-μ_r stage materials. The discharge conditions are the same as in Chapter 4.5, except that C_6H_6 (50 sccm) is added at a total pressure of 13 Pa. Thermal crayons are used to measure the stage temperature, and the temperature during deposition is below 300 °C, which is substantially lower than that of graphite formation through a thermal effect.[4] Figure 4.12(a) and (b) show the surface resistance and deposition rate of carbon films as a function of the bias voltage V_{PLS}, respectively. Regardless of the V_{PLS}, the sheet resistance for the case of the low-μ_r material is lower than that of the high-μ_r case, and it is lower than the Si sheet resistance at a $|V_{PLS}| \geqq$ ~1.2 kV, which is ~700 V lower than that of the high-μ_r case. In the carbon film deposition by SWP (Chapter 3), the sheet resistance of the film deposited at V_{PLS} = 1.0 kV is more than 10^9 Ω/sq, which is much higher than the result of the present study at the same V_{PLS} with the low-μ_r stage. The ratio of the energy flux from ions to a depositing carbon atom flux is considered to be an important parameter for increasing the electrical conductivity of the carbon film. Figure 4.12(b) shows the deposition rates of films deposited using the low- and high-μ_r stages. The film deposition rate of the low-μ_r stage is lower than that of the high-μ_r

stage. This is due to the removal of the C–H bonds as well as the sputtering of the film caused by greater ion flux in the case of the low-μ_r stage.

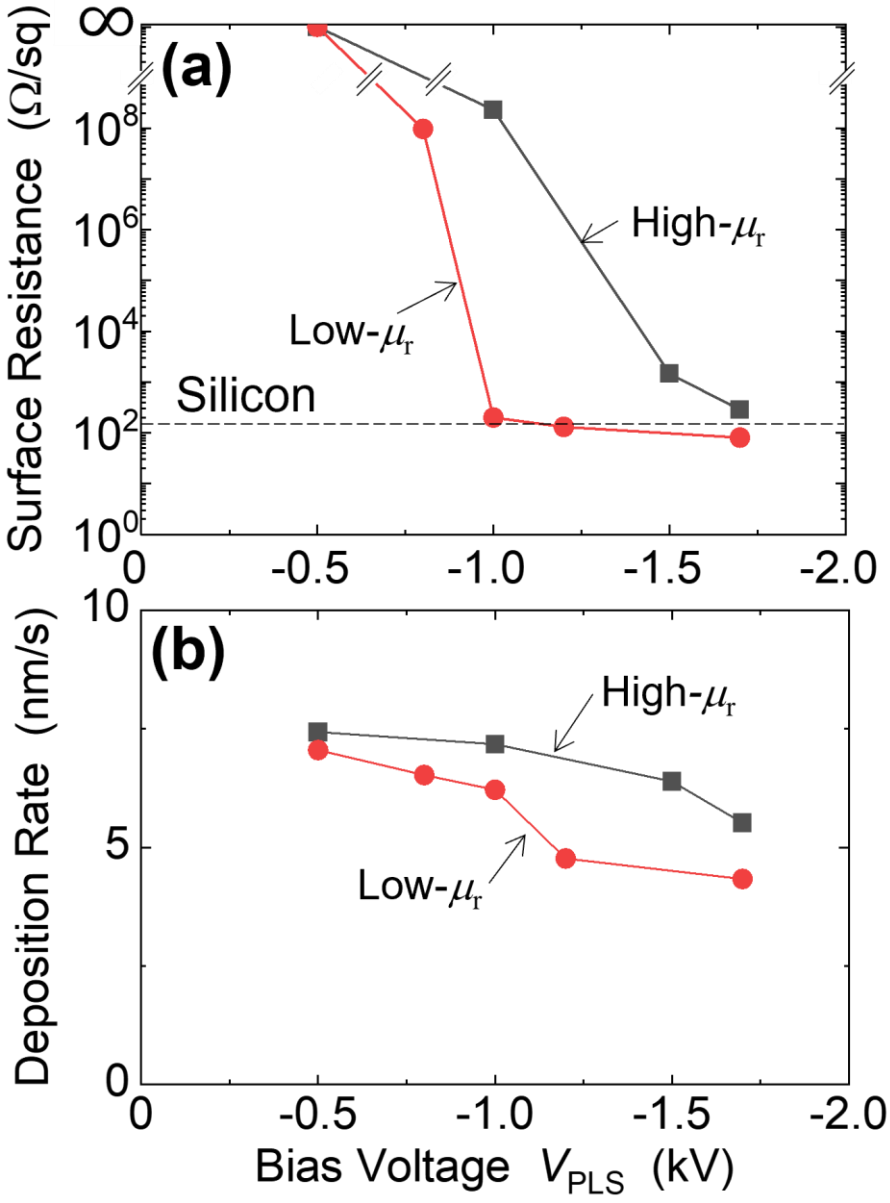

Figure 4.12 (a) Sheet resistance and (b) deposition rate of deposited carbon films as a function of pulse bias voltage V_{PLS}.

To evaluate the deposition efficiency of the precursor gas, number of deposited carbon atoms per second in the whole chamber (N_c) is evaluated from the deposition rate.

$$\Gamma_{\mathrm{C}}^{\mathrm{ECR\_PLS}} = \frac{\rho_c}{M_c} \times (\text{Avogadro's number}) \times (\text{deposition rate}), \quad (4.14)$$

$$N_c = \Gamma_{\mathrm{C}}^{\mathrm{ECR\_PLS}} \times A_{dep}. \quad (4.15)$$

Here, $\Gamma_{\mathrm{C}}^{\mathrm{ECR\_PLS}}$ is the deposited carbon flux per unit area. ρ_c is the specific gravity of the high conductive carbon deposited with low-μ_r stage at a V_{PLS} = 1.0 kV is 2.2. M_c is molar mass of the carbon. A_{dep} is the deposited area. The deposition rate at a V_{PLS} = 1.0 kV is ~5 nm/s. So, $\Gamma_{\mathrm{C}}^{\mathrm{ECR\_PLS}}$ is 5.5×10^{16} /cm^{2}s smaller than $\Gamma_{\mathrm{C}}^{\mathrm{SWP\_PLS}}$ ~ 7.0×10^{16} /cm^{2}s at a V_{PLS} = 2.0 kV as calculation in Chapter 3. Some reasons for the decrease of the deposited carbon flux are considered as the dissociation rate of the benzene and the sputtering effect. The dissociation rate of the benzene will be discussed in Chapter 4.8. The dissociation rate of the benzene is ~98% without the bias application and it is ~100% with the bias application. It means that the benzene is fully utilized for the deposition without the bias application. However, the sputtering effect increases by applying the bias voltage, because the increase of the plasma density leads to increase of the ion flux. Therefore, $\Gamma_{\mathrm{C}}^{\mathrm{ECR\_PLS}}$ is not considered as smaller than $\Gamma_{\mathrm{C}}^{\mathrm{SWP\_PLS}}$.

If almost of the carbon atoms are used for the deposition, the

deposited carbon atoms from the benzene dissociation can be evaluated to be ~1.3×10^{20} s^{-1} from the benzene gas flow (50 sccm). N_c is ~3.9×10^{19} s^{-1} with the stage area ~697 cm^2. However, the non-uniform deposition along the height direction of the stage (y axis in Figure 4.1) should be considered. So, the deposition efficiency of the precursor gas is estimated as smaller than 30% for the benzene gas flow 50 sccm.

To investigate the deposited carbon film structure, Raman spectroscopy and FTIR measurement are performed. Raman spectroscopy is a method for evaluating sp^2 and sp^3 bonds in the carbon film.[5-27] There are two peaks with different vibrational modes in the Raman spectrum of the carbon film, *i.e.*, G-peak (graphite peak: 1520–1600 cm^{-1}) and D-peak (disorder peak: 1340–1380 cm^{-1}). G-peak originates from the stretch mode of sp^2 bond, and D-peak is from the breath mode of sp^2 sixfold ring. Ferrari and Robertson introduced a trend of I(D)/I(G) ratio and G-peak shift changing the carbon film structure from sp^3-rich to sp^2-rich films, *i.e.*, tetrahedral amorphous carbon (ta-C), amorphous carbon (a-C), nanocrystalline graphite (NCG), and graphite.[26,27] They showed that as the I(D)/I(G) ratio and G-peak wavenumber increase, the film structure shifts from a-C to NCG. Figure 4.13(a) shows the Raman spectra of carbon films deposited using the high-μ_r and low-μ_r stages at a bias voltage of −1.0 kV and a Raman light source wavelength of 532 nm. Their greatest G-peak intensities are used to normalize the intensities. When compared with the high-μ_r result, the low-μ_r spectrum has a higher I(D)/I(G) ratio and a larger

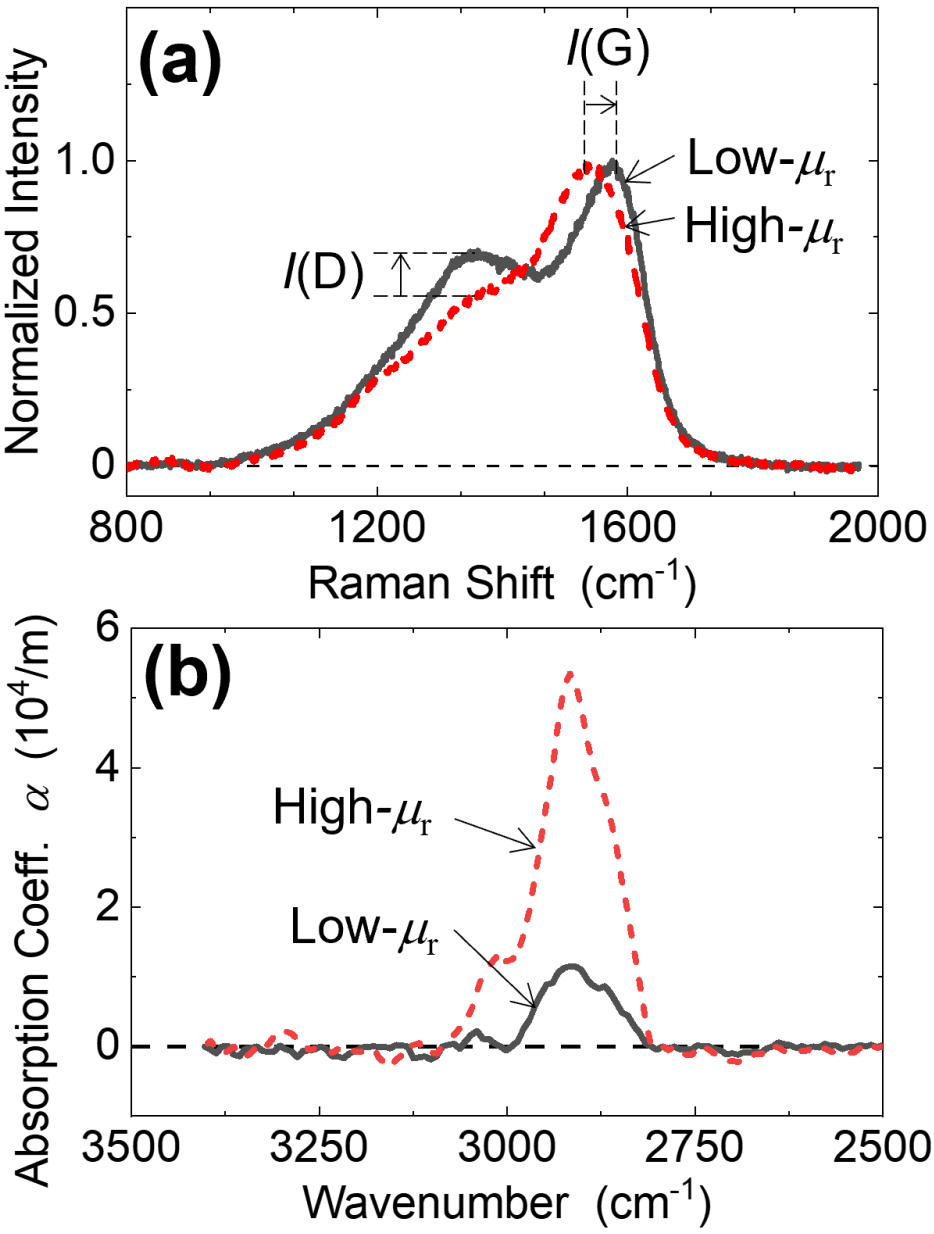

Figure 4.13 (a) Raman spectra and (b) FTIR spectra at V_{PLS} = 1.0 kV.

G-peak wavenumber. This implies that the carbon film deposited with the low-μ_r stage has a higher sp^2 composition and is more similar to the NCG film. In the carbon film deposition using the SWP (Chapter 3), two-dimensional distribution of the high sp^2 content in the carbon film was investigated *via* transmission electron microscopy and electron energy loss spectroscopy, and amorphous structure carbon film with a large amount of nanosized sp^2 clusters has been confirmed.

As mentioned in Chapter 4.1, the dehydrogenation of the C–H bond in the film by ion bombardment produces sp^2 bonds in carbon film. In other words, the C–H bonds degrade the film conductivity. FTIR spectroscopy is used to analyze the hydrogen concentration of the carbon film.[26,28-29] IR light absorptions are seen at wavenumbers of approximately 3000 cm^{-1}, *i.e.*, wavenumbers of C–H vibration modes, and C–H bond density (n_{CH}) is evaluated using the following equation:

$$n_{CH} = A_s \int \frac{\alpha(k)}{k} dk. \quad (4.16)$$

Here, k and α are the wavenumber and absorption coefficient of the deposited film, respectively. A_s is proportional constant and is 8.7×10^{20} cm^{-2}.[29] The dash and solid curves in Figure 4.13(b) shows the absorption spectra of carbon films deposited with low- and high-μ_r stages, respectively. The calculated C–H bond density (3.9×10^{21} cm^{-3}) of low-μ_r film is much lower than that of high-μ_r film (1.9×10^{22} cm^{-3}), showing the reduction of C-H bonds by using the low-μ_r stage with higher ion flux.

4.7 Comparison between ECR plasma and SWP for carbon film deposition

As mentioned in Chapter 4.1, the reason of introducing the ECR plasma was to deposit the conductive carbon films at lower bias voltages. As a solution, improvement of the plasma density was considered. The ECR plasma with the high negative bias power realized the high plasma density (n_{ECR}~1.8×10^{18} m^{-3}) over 4 times higher than SWP (n_{SWP}~4×10^{17} m^{-3}) under the Ar plasma. To confirm the ion flux enhancement by introducing the ECR plasma source, the properties of the carbon film deposited by the ECR plasma with the low-μ_r stage and the SWP are compared as shown in Figure 4.14. Figure 4.14 shows the properties (a) sheet resistance, (b) Raman spectra at a stage voltage 1.0 kV and (c) C-H absorption coefficient at a stage voltage 1.0 kV. Results of the ECR films show obviously higher sp^2 content and lower C-H bond than those of the SWP films. The deposition rate (~5 nm/s at V_{PLS}> 1.5 kV) of the ECR film is lower than that of the SWP, but it is still relatively higher than surveyed high conductive carbon film deposition rate in Chapter 1. Therefore, the idea of the high conductive carbon film deposition at the low bias voltage is realized by introducing the ECR plasma source.

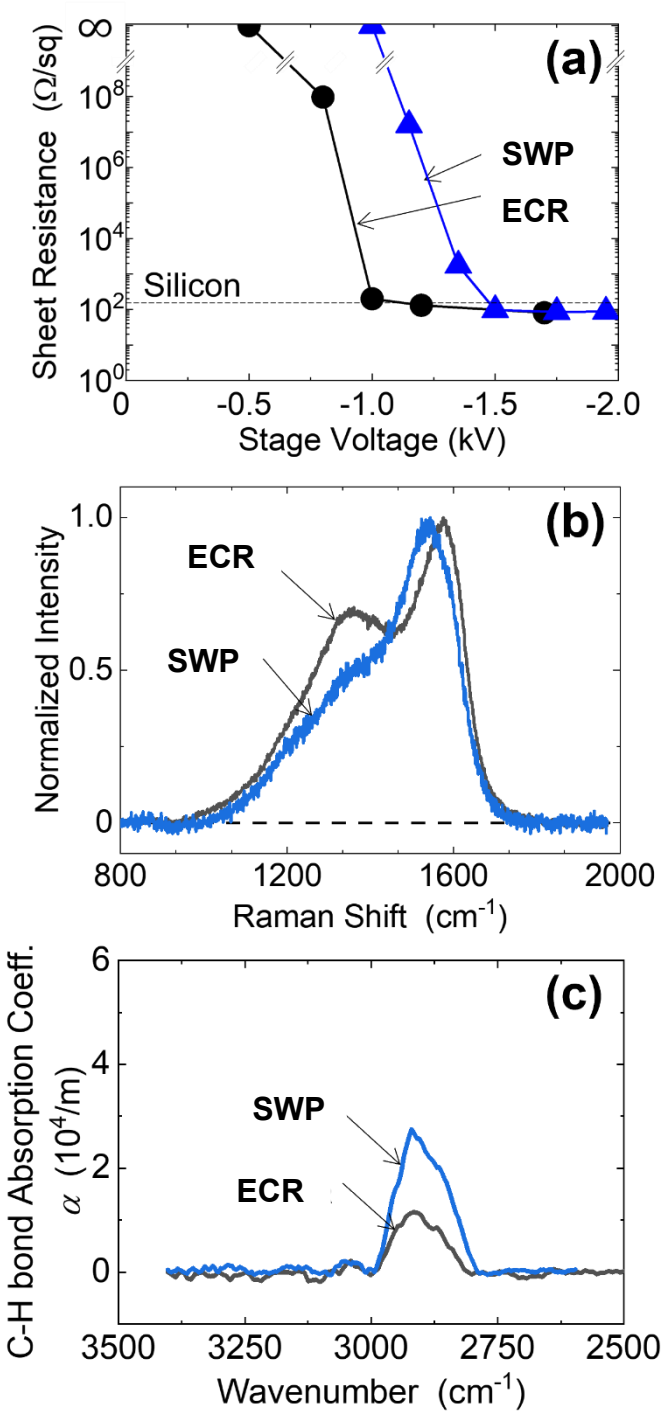

Figure 4.14 Properties of carbon films deposited by the ECR plasma and the SWP. (a) sheet resistance, (b) Raman spectra at a stage voltage 1.0 kV and (c) C-H absorption coefficient at a stage voltage 1.0 kV.

4.8 Quadrupole mass spectrometer measurement

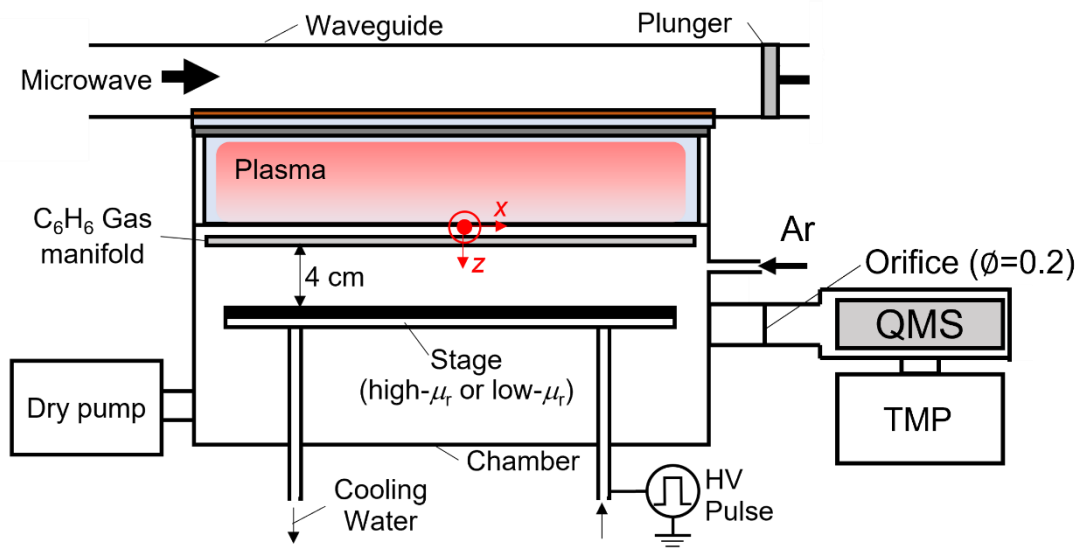

Figure 4.15 Experimental setup for QMA

The change of the precursor gas by the dissociation in the plasma is evaluated by a quadrupole mass spectrometer (QMS). The QMS experimental setup is shown in Figure 4.15. The working pressure of the QMS chamber is 4×10^{-3} Pa. The electron energy for the ionization in the QMS is -70 V. The mass spectra of benzene are evaluated at conditions of the plasma-off, plasma-on without bias application, and plasma-on with bias application V_{PLS} = 1.0 kV, as shown in Figure 4.16(a). When the plasma is on without the bias application, the benzene peaks decrease to 2% of their initial intensities, *i.e.*, intensities at plasma-off. It means that the benzene gas is almost dissociated by the plasma. Furthermore,

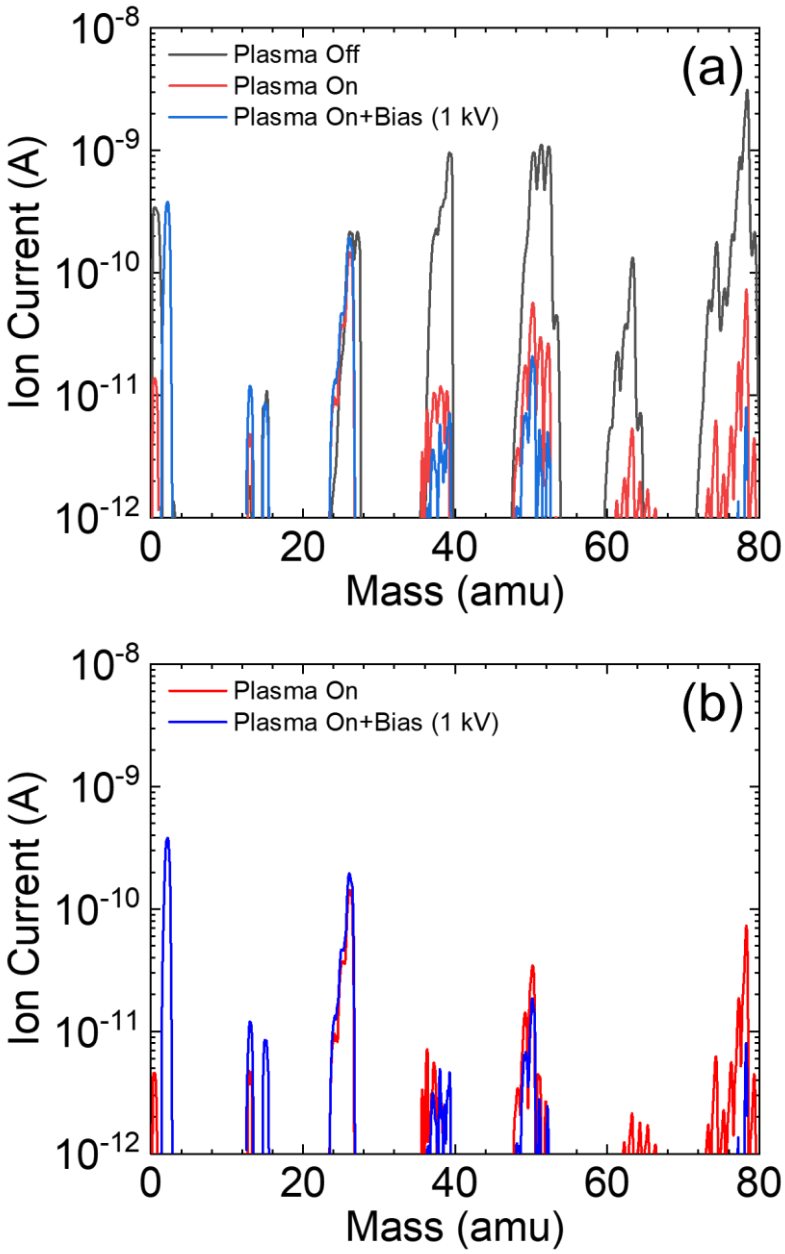

Figure 4.16 Generated molecules by plasma. (a) mass spectra for plasma-off, plasma-on without bias application, and plasma-on with bias application. (b) benzene fragment deleted mass spectra for plasma on without bias application and with bias application.

when the plasma is on with the bias application, the benzene peaks further decrease down to 0.2% of their plasma-off intensities. It is considered increased plasma density affect the benzene dissociation. To give an insight into molecules produced by the plasma, peak intensities originated from benzene molecules are subtracted from the measured plasma-on spectra, taking account for decrease in the benzene peak intensities by the benzene dissociation (Figure 4.16 (b)). The hydrogen peak (amu=2) drastically increases by applying the bias power. It shows the dehydrogenation of the carbon film by the ion bombardment. In the mechanism of the sp^2 bond increase by the ion bombardment (Chapter 1), the ion bombardment breaks the C-H bond and the hydrogen is extracted from the carbon film. The increase in the hydrogen density in the gas phase agrees well with this mechanism. The increase of CH_x peaks is presumably due to hydrocarbon release from the carbon film through carbon etching by hydrogen ions or atoms produced by the dissociation of hydrogen molecule or benzene. Surface fragmentation of benzene on the film depositing surface might be also considered.

4.9 Conclusion

A new method of conductive carbon film deposition using an ECR plasma source with high-voltage pulse power supply was proposed. The plasma properties, as well as deposited carbon film properties, were evaluated. The introduction of the bias pulse power enhanced the ion flux

to the bias stage. The temporal variation of plasma density was explored using the Langmuir probe and the OES for two types of stage materials, namely, high and low permeabilities (μ_r). During the high-voltage pulse application, an increase in plasma density was observed, particularly in the low-μ_r stage. A power balance model taking account for the ionization by the high-energy secondary electrons was proposed. The plasma density ratio of pulse-on and pulse-off conditions was measured and was compared with the density ratio estimated from the measured time constants based on the model. The estimated density ratio agreed well with the measured density ratio, from which the model was validated. Furthermore, the significance of magnetic field arrangement for the plasma density increase using high-voltage pulse power was emphasized. Electron trajectory simulation revealed that a magnetic field spanning the bias stage at an inclined angle was required for secondary electron confinement and power absorption from high-energy secondary electrons. Carbon films were deposited using an ECR plasma source and a high-voltage pulse power source, and the low-μ_r stage demonstrated high electrical conductivity at a lower bias voltage than the high-μ_r stage. The carbon film deposited by the low-μ_r stage had more sp^2 bonds than the high-μ_r stage and SWP. These results indicate that a higher ion flux is important for enhancing the carbon film conductivity and that the new plasma source is effective in depositing conductive carbon films using the high-voltage pulse power source for the plasma density enhancement.

References

[1] S. Fu, J. Chen, S. Hu, X. Wu, Y. Lee and S. Fan: *Plasma Sources Sci. Technol.* **15** (2006) 187.

[2] O. A. Popov: *J. Vac. Sci. Technol.* **A 7** (1989) 894.

[3] B. Szapiro and J. J. Rocca: *J. Appl. Phys.* **65** (1989) 3713.

[4] S. Bhargava, H. D. Bist, A. V. Narlikar, S. B. Samanta, J. Narayan and H. B. Tripathi: *J. Appl. Phys.* **79** (1996) 1917.

[5] J. Guo, X. Chen and C. Wang: *J. Mater. Chem.* **20** (2010) 5035.

[6] Y. Show: *Surf. Coat. Technol.* **202** (2007) 1252.

[7] T. Fukutsuka, T. Yamaguchi, S. Miyano, Y. Matsuo, Y. Sugie and Z. Ogumi: *J. Power Sources* **174** (2007) 199.

[8] C. Chung, S. Chen, P. Chiu, M. Chang, T. Hung and T. Ko: *J. Power Sources* **176** (2008) 276.

[9] K. Feng, Y. Shen, H. Sun, D. Liu, Q. An, X. Cai and P. K. Chu: *Int. J. Hydrog. Energy* **34** (2009) 6771.

[10] L. Li, L. Liu, X. Li, P. Guo, P. Ke, and A. Wang: *ACS Appl. Mater. Interfaces* **10** (2018) 13187.

[11] S. Zhou, G. Liu, N. Ding, L. Shang, R. Dang and J. Zhang: *Surf. Coat. Technol.* **399** (2020) 126150.

[12] Y. Wang, J. Pu, J. Wang, J. Li, J. Chen and Q. Xue: *Appl. Surf. Sci.* **311** (2014) 816.

[13] RUR. Sagar, X. Zhang, C. Xiong and Y. Yu: *Carbon* **76** (2014) 64.

[14] A.N. Obraztsov, E.A. Obraztsova, A.V. Tyurnina and A.A. Zolotukhin: *Carbon* **45** (2007) 2017.

[15] M. Yudasaka, R. Kikuchi, T. Matsui, H. Kamo, Y. Ohki, S. Yoshimura and E. Ota: *Appl. Phys. Lett.* **64** (1994) 842.

[16] J. Sun , N. Lindvall, M. T. Cole, T. Wang , T. J. Booth, P. Bøggild, K. B. K. Teo, J. Liu and A. Yurgens: *J. Appl. Phys.* **111** (2012) 044103.

[17] D. Noll, P. Hönicke, Y. Kayser, S. Wagner, B. Beckhoff and U. Schwalke: *ECS J. Solid State Sci. Technol.* **7** (2018) Q3108.

[18] N. Weber, A. Binder, M. Kettner, S. Hirth, R. T. Weitz and Ž. Tomović: *Carbon* **112** (2017) 201.

[19] A.N. Obraztsov, A.V. Tyurnina, E.A. Obraztsova, A.A. Zolotukhin, B. Liu, K. Chin and A.T.S. Wee, *Carbon* **46** (2008) 963.

[20] J. Robertson, *J. Non-Cryst. Solids* **137**&**138** (1991) 825.

[21] M. A. Tamor and W. C. Vassell, *J. Appl. Phys.* **76** (1994) 3823.

[22] G. Capote, G.C. Mastrapa and V.J. Trava-Airoldi: *Surf. Coat. Technol.* **284** (2015) 145.

[23] Ju Che, Peiyun Yi, Linfa Peng and Xinmin Lai: *Int. J. Hydrog. Energy* **45** (2020) 16277.

[24] Y. Wang, L. Wang, G. Zhang, S.C. Wang, R.J.K. Wood and Q. Xue: *Surf. Coat. Technol.* **205** (2010) 793.

[25] A.A. Ogwu and R.W. Lamberton: *J. Phys. D: Appl. Phys.* **32** (1999) 981.

[26] J. Robertson: *Mater. Sci. Eng. R Rep.* **37** (2002) 129.

[27] A.C. Ferrari and J.Robertson: *Phys. Rev.* **61** (2000) 14095.

[28] M. Veres, M. Koós and I. Pócsik: *Diam. Relat. Mater.* **11** (2002) 1110.

[29] H. Kojima, H. Kako, M. Terada, H. Sugai and T. Okuda: *Jpn. J. Appl.*

Phys. **24** (1985) 1432.

Chapter 5

Conclusion and future scope

5.1 Conclusion of dissertation

In the past 20 years, interests in the carbon coatings have increased significantly and studies for applying carbon coating to a lot of industrial fields have been carried out due to attractive features of carbon films, *i.e.*, the chemical stability and the high thermal conductivity. Furthermore, electrical conductivity, strength, and friction coefficient have been controlled by the sp^2 and sp^3 content ratio of the carbon film. Due to many studies of carbon film coating, the recent carbon films have been deposited in well-defined conditions and can be selectively applied to various fields with required features. High sp^2 content carbon film, which is amorphous carbon (a-C) or hydrogenated amorphous carbon (a-C:H), is applied in electrodes, batteries, fuel cell, bearing and so on because of its electrical conductivity, anti-corrosion and low frictional force. There are two typical methods for increasing the sp^2 content in the carbon film: heating the substrate over 500 ^oC or increasing incident ion to the carbon film. However, heating the substrate has a problem in that the substrate may receive thermal damage. On the other hand, the ion bombardment effect can increase sp^2 even at lower temperatures less than 400 ^oC. In the deposition methods of high conductive carbon film, there are 3

typical methods, *i.e.*, physical vapor deposition (PVD), chemical vapor deposition (CVD), and plasma enhanced chemical vapor deposition (PECVD). However, in the production of the high conductive carbon film, the low deposition rate less than 1 nm/s is a big problem because the thickness of the carbon film is usually required over 500 nm.

To solve the above issues, three approaches were adopted in this study. Firstly, a microwave plasma, a high-density plasma ($\geq 10^{17}$ m^{-3}) source which can realize uniform plasma process in 35 cm width, was used. This plasma source contributes to enhance productivity both from the viewpoint of the high throughput with large-surface area and from the viewpoint of high process speed. Secondly, the high negative bias voltage was applied in this study. To increase the ion incident energy, high negative bias voltage up to -2kV were introduced for the ion energy enhancement. Finally, the benzene gas was adopted as the precursor gas because it has a high deposition rate by its low ionization potential. As a result, the carbon film was deposited with a high electrical conductivity and high deposition rate of ~5, 6 times higher than those of previous studies.

In Chapter 2, the principles of high-density plasma sources used in Chapters 3 and 4, *i.e.*, surface-wave plasma (SWP) and electron cyclotron resonance (ECR) plasma, were explained. In addition, film evaluation methods, i.e., a four-terminal sensing for the electrical conductivity measurement, Raman spectroscopy, X-ray photoelectron spectroscopy (XPS), scanning and transmittance electron microscopy

(STEM) and electron energy-loss spectroscopy (EELS) for the film structure measurement, were explained. Fourier transform infra-red spectroscopy (FTIR) was also introduced for the evaluation of C-H bonds.

In Chapter 3, a high conductive carbon film was deposited by introducing the SWP plasma. The SWP realized the high-density plasma with plasma densities up to 4×10^{17} m^{-3} with high spatial uniformity along a chamber width of ~35 cm. At high bias voltages, high conductive (80 Ω/sq, estimated electrical conductivity >200 S/cm) carbon films were successfully deposited. In parallel with the conductivity measurement, influence of the ion incident energy on the carbon film structure and characteristics were studied in detail. By increasing ion incident energy, the electrical conductivity of the carbon film increased and the deposition rate decreased. The reason for the decrease in the deposition rate was explained by the change in the film structure and the sputtering effect. With increasing the ion incident energy, the hydrogen content in the film decreased and the sp^2 content ratio increased. When a bias voltage of -2.0 kV was applied to the stage, the hydrogen content evaluated by FTIR was less than 5%, and the sp^2 content evaluated by XPS was more than 70%. The carbon film was confirmed to be the amorphous structure with nano-sized sp^2 clusters (≥~15 Å) by Raman spectrum, STEM and EELS.

In Chapter 4, the high conductive carbon film was deposited by the ECR plasma source. Higher plasma densities ($\geq1\times10^{18}$ m^{-3}) more than that of SWP was realized, especially when the bias voltage was applied

to the stage. The phenomenon of the plasma-density increase in the bias application was confirmed by OES and Langmuir probe measurements. The increase in the plasma density was prominent when the low permeability material was used as the stage material, but not in the case of the high permeability stage. This suggested that the increase of the plasma density was caused by the change in the magnetic field structure near the stage. The reason for the plasma density increase was attributed to the secondary electrons which were generated by ion collision on the stage surface. They were accelerated by the sheath and were confined between the stage and the antenna due to the magnetic mirror effect and the sheath electric field, contributing to the effective ionization of the plasma. A theoretical zero-dimensional model of the increase of the plasma density well explained the experimental results. The increase of the plasma density and resultant increase of the ion flux to the stage realized to deposit the high conductive (100 Ω/sq) carbon film at lower bias voltages (V_{PLS}~1.0 kV). By increasing the ion flux, the hydrogen content in the film decreased from 1.0×10^{22} cm^{-3} to 3.9×10^{21} cm^{-3} and the sheet resistance decreased from 8.0×10^{8} Ω/sq to 1.0×10^{2} Ω/sq. The Raman spectrum showed that the increase of the sp^2 content in the carbon film. The dissociation of the benzene gas was evaluated by QMS. The plasma density affected the benzene dissociation. When the plasma was on without the bias application, the QMS peaks of the benzene decreased down to 2%. When the plasma was on with the bias application (higher plasma density than that without the bias application), the QMS peaks of

the benzene further decreased down to 0.2%. Additionally, the dehydrogenation of the carbon film by the ion bombardment was investigated by the QMS. The hydrogen drastically increased by applying the bias power. This result supported the mechanism of the sp^2 bond increase due to the dehydrogenation by the ion bombardment.

In conclusion, this study realized one-dimensionally uniform (~30 cm) conductive carbon film deposition at high deposition rates (~6 nm/s) and low substrate temperatures (<300 ºC). This study introduced a new method to realize low-cost deposition of anti-corrosion electrically-conductive film for the bipolar plates of the proton exchange membrane fuel cells.

5.2 Future scope

The achievements of this study are the realization of the high conductive carbon film (80 Ω/sq, estimated electrical conductivity >200 S/cm) deposition with high deposition rate (5,6 nm/s) ~5, 6 times faster than previous works. Additionally, the effects of ion flux and ion incident energy on carbon film formation were evaluated on the features and structure of the carbon film. However, several challenges remain in introducing surface wave plasma and ECR plasma into commercial applications.

(1) Carbon deposition on the dielectric (quartz) surface

In the deposition process, the chamber is contaminated with

the carbon deposition. To generate the plasma, the microwaves is absorbed by the plasma through the quartz window. The problem is that the deposited carbon on the quartz surface interferes the microwave transmission from the quartz to the plasma. Accordingly, for a long-time discharge, the plasma becomes unstable or the plasma density decreases. To solve this problem, plasma sources with advanced structure must be considered. One of solutions might be an ECR plasma source with new microwave launcher. In the ECR plasma, plasma production region is localized near the ECR zone and, if the microwave launcher is placed away from the ECR zone with a deposition-suppressed structure, a high-density one-dimensionally uniform plasma with suppressed deposition interference on the microwave launcher might be realized. Another solution is usage of very high frequency (VHF) capacitively coupled plasma (CCP). It has high plasma density with spatial uniformity of ~30 cm, although the uniform plasma production sometimes becomes difficult at plasma sizes of ~1 m.

(2) Productivity

In industrial applications, the speed of the process is the most important factor to reduce the production cost. This study suggested a method to increase productivity by using high-density plasma. However, there are other method to increase productivity,

i.e., change in the precursor gas, change in the supply ratio of the precursor gas, change in the plasma generation method and so on.

(3) Substrate temperature control

For the application to the PEMFC, the carbon film is coated on the metal substrates. To suppress the total weight of the PEMFC, the substrate thickness is required to be less than 0.2 mm. However, such thin substrate is difficult to place on the flat stage with good thermal contact with the stage. In this study, the samples were placed on the stage simply by the clamping structure and, especially when thin substrates were used, temperature control was difficult because substrates were deformed by less thermal contact and resultant thermal expansion. For this reason, this study used mainly Si substrates because they are thick (0.5 mm) and have small thermal expansion property. In the commercial level, however, not simple flat stage but roll-to-roll system will be adopted for the thin metal substrates, because the thin metal substrates receive uniform tension and they will make good thermal contact with the cooling drum stage.

(4) Low adhesion of carbon film

The carbon sometimes peels off because the carbon film has high stress in it. To solve this issue, adhesion strength of the carbon films with substrates must be increased. In the case of the carbon

film, native oxide layer on the surface which drastically degrades the carbon adhesion must be removed. One of ways to remove the oxide layer is Ar ion bombardment, and this method has been adopted in this study for the oxide layer removal from the Si surface. In the case of the stainless-steel substrate, however, the oxide-layer removal becomes much more difficult than the case of Si substrates. One of solutions for this issue is introduction of an intermediate layer between the stainless-steel and the carbon film. If an appropriate material for the intermediate layer is applied, the adhesion of the carbon film on the stainless-steel will be much more enhanced.

Acknowledgment

From my master course, I have studied ‘plasma’ under the guidance of Professor Hirotaka Toyoda. For a long time, he has made a lot of effort on my training related to my research. I deeply appreciate his attentive guidance, a lot of help and support.

I would like to show my gratitude to Professor Masaru Hori, Professor Makoto Sekine and Professor Hiroyuki Kousaka. They have given me great advice and have guided my research in the better direction.

I also thank Assistant Professor Haruka Suzuki for her assistance. She is my nice supervisor and is best friend who has worked hard with me. She has given me advices if I have any problem, and she has suggested me good solution. Without the help of Professor Hirotaka Toyoda and Professor Haruka Suzuki, I would not have been able to adjust to Japan and finish my studies.

I would like to show my gratitude to Kensuke Sasai. He has given me a lot of ideas and support in my Ph. D research, and as a result, I have been able to get good results.

I would like to thank Taku Suyama, Kota Tamura, Makoto Moriyama, Naoya Nakahara, Hung Chu, Kazuki Tsutsumi, Kazuya Hikita, Yukinori Chiba, Tomohiro Ogasawara, Kazuya Yamaguchi, Ikumi Hamaguchi, Keita Ichikawa, Yuto Seki, Yuki Iwata, who are my previous coworker and present coworker. They are always kind and humble to me. When I was faced on difficulties, I was possible to overcome them with their help.

I appreciate help of technical supporters of Raman spectroscopy, XRD and XPS. I also appreciate help of officers in Electronics Department and International Students Section, Nagoya University. Furthermore, I appreciate financial supports from NGK Foundation for International Student, and Toyoda Tsusho International Student Scholarship. They are greatly helpful to me for my study and my living.

I appreciate my friends in Korea, especially, Wooyoung Lee, Bin Ha, Meang Kim, Nancho Kim, Myunghoon Lee, Sorri Kim, Do Kim, Chansoo Han, Likehyun An, Byeung Su, Younghun Lee, Yeonjung Kim, Cheoljung Woo, Sungu Kim, Seokhyun Kim, Gyudoek Kim, Jaeho Kim, Sanghun Kim, Hyunwoo Gyeung

Finally, thank and love my family, Jongoh Bae, Eunhee Kim, Jinseol Bae.

List of papers and presentations

	Title	Information	Authors	Ch
	I. Paper			
1	High-speed deposition of graphite-like carbon film by Ar/C_6H_6 surface-wave plasma with high-voltage pulse biasing	*Vacuum* **192**, 110429, (2021).	H. Bae, K. Sasai, H. Suzuki, H. Toyoda	2,3
2	Enhancement of the ion flux to the substrate by high voltage biasing in an electron cyclotron resonance plasma and its application to high-speed deposition of conductive carbon film	*Japanese Journal of Applied Physics*, **60**, 126002, (2021).	H. Bae, I. Hanaguchi K. Sasai, H. Suzuki, H. Toyoda	2,4
	II. International conference			
1	Wide-area and High-speed Deposition of Graphitic Film by Microwave Surface Wave Plasma with High Power Pulse	13th International Symposium on Advanced Plasma Science and its Applications for Nitrides and Nanomaterials 14th International Conference on Plasma-Nano Technology & Science, Nagoya, Japan. (March 7-11, 2021)	H. Bae, H. Suzuki, K. Sasai, H. Toyoda	2,3

	論文題目	発表の方法及び時期	著者	章
2	High conductive carbon film deposition by DC and microwave power superposition	The 74th Annual Gaseous Electronics Conference, USA, Virtual. (October 4-8, 2021）	H. Bae, I. Hanaguchi H. Suzuki, K. Sasai, H. Toyoda	2,3 ,4
3	High Speed sp^2-rich Carbon Film Deposition with Surface-wave Microwave Plasma	42nd International Symposium on Dry Process, Japan, Virtual. (November 18-19, 2021)	H. Bae, I. Hanaguchi H. Suzuki, K. Sasai, H. Toyoda	2,3
	III. Domestic conference			
1	High speed and wide area conductive carbon film deposition by surface-wave plasma	第 37 回 プラズマ・核融合学会, Aichi, Japan. (December 1-4, 2020)	H. Bae, K. Hikita, H. Suzuki, K. Sasai, H. Toyoda	2,3
2	Wide Area and High Rate Deposition of Graphitic Carbon by Surface Wave Plasma	The 38th Symposium on Plasma Processing/ The 33rd Symposium on Plasma Scidence for Materials, Japan, Virtual. (January 27-29, 2021)	H. Bae, H. Suzuki, K. Sasai, H. Toyoda	2,3
3	High-speed Deposition of Graphite-like Carbon Film by Microwave Surface-wave Plasma	The 68th JSAP Spring Meeting 2021, Japan, Virtual. (March 16-19, 2021)	H. Bae, K. Hikita, H. Suzuki, K. Sasai, H. Toyoda	2,3
4	High speed and wide area conductive carbon film deposition by surface-wave plasma	The 82 th JSAP Autumn Meeting 2021, Japan, Virtual. (September 10-13, 2021)	H. Bae, I. Hanaguchi H. Suzuki, K. Sasai, H. Toyoda	2,4